博士論文（要約）

# Novel magnetic excitations in spin systems investigated by neutron scattering

（中性子散乱によるスピン系の新奇な磁気励起の研究）

林田　翔平

# Contents

# Preface

An importance of a spin system is an easy access to the verification of theories of non-trivial phenomena. The effective experimental tool is neutron scattering which probes static and dynamical states of matter. In this study, the two spin systems are focused; the singlet ground state magnet $CsFeCl_3$ and the Kagome lattice antiferromagnet $NaBa_2Mn_3F_{11}$. $CsFeCl_3$ exhibits a pressure-induced quantum phase transition, and an observation of Higgs amplitude mode is expected in the spin spectrum. $NaBa_2Mn_3F_{11}$ is a classical Kagome antiferromagnet and a zero-energy mode is expected.

The quantum phase transition is a transition between different ground states induced by the quantum fluctuation, which is controlled by a parameter such as magnetic field, pressure, and chemical doping. In the vicinity of the quantum critical point, the quantum fluctuation is enhanced so that non-trivial phenomena are expected. In the quantum field theory, collective excitations near the quantum critical point in the ordered phase is described by the phase and amplitude fluctuations of an order parameter. While the phase fluctuation is known as Nambu-Goldstone mode, amplitude one is called Higgs mode which is analogue to Higgs boson in particle physics.

$CsFeCl_3$ is a singlet ground state magnet having a strong easy-plane single-ion anisotropy. The magnetic $Fe^{2+}$ ions form a triangular lattice, and its low-energy excitation is described by a pseudo-spin $s = 1$ due to the cubic crystal field and spin-orbit coupling. The pseudo-spin $s = 1$ is split into $s^z = 0$ singlet and $s^z = \pm 1$ doublet states due to the easy-plane type single-ion anisotropy. In the system, the singlet ground state is realized. $CsFeCl_3$ is thus a good model compound to investigate the quantum critical phenomena on the geometrically frustrated lattice. Magnetic susceptibility measurement under pressure revealed the pressure-induced magnetic long-range order at low temperatures in $CsFeCl_3$. To investigate non-trivial phenomena in the vicinity of the quantum critical point, I study the static and dynamic states of magnetism of $CsFeCl_3$ under pressure by using neutron diffraction and inelastic neutron scattering techniques.

The neutron diffraction experiments under pressures evidences that a 120° structure with $\boldsymbol{k}_{\rm mag} = (1/3, 1/3, 0)$ is realized in the ordered phase. The estimate of the critical exponent from the temperature dependence of the order parameter indicates that the system belongs to the universality class of $U(1) \times Z_2$, in which the unusual chiral liquid state is predicted.

In the inelastic neutron scattering spectrum under pressures, the magnetic excitation are softened toward the critical pressure $P_{\rm c} \sim 0.9$ GPa, and a well-defined excitation with an energy minimum of 0.6 meV and a gapless continuum-like excitation are observed at 1.4 GPa in the ordered phase. The theoretical calculation of the spin spectrum elucidates that the observed well-defined excitation exhibits the mixed mode of transverse and longitudinal fluctuations (T+L-mode), and the gapless continuum-like excitation is the Nambu-Goldstone mode. The non-trivial T+L-mode is caused by the geometrical frustration because the non-collinearity of the 120° structure mixes the transverse and longitudinal fluctuations.

A geometrical frustration in the spin system is generated by the competition of the magnetic interaction due to the lattice geometry, and it remains the macroscopic degeneracy of the magnetic states at low temperatures. Since the macroscopic degeneracy induces the novel magnetic states such as the spin liquid state and unusual spin configuration, the geometrically frustrated

magnets have attracted great interest for a few decades. In case of the classical Kagome Heisenberg antiferromagnet, the highly-frustrated geometry causes macroscopic degeneracy, and a 120° structure is realized by order-by-disorder mechanism. In addition, the large degeneracy of the 120° structure at the ground state generates continuous arrangements of spins, and it forms excitation modes of zero energy, which is called zero-energy mode. In real compounds, additional terms including magnetic anisotropy and/or Dzyaloshinskii-Moriya interaction selects the unique ground state, and the zero-energy mode is lifted to the excited state.

$NaBa_2Mn_3F_{11}$ is a new model compound for a classical Kagome antiferromagnet. $Mn^{2+}$ ion having spin $S = 5/2$ form the Kagome lattice. The heat capacity and magnetic susceptibility exhibited an antiferromagnetic transition. The small Curie-Weiss temperature implies the importance of the magnetic dipole-dipole (MDD) interaction in $NaBa_2Mn_3F_{11}$. Recent theoretical study in the classical Kagome antiferromagnet having the MDD interaction demonstrated the unusual 120° structure with a tail-chase geometry and the existence of the zero-energy mode. In order to discuss the role of the MDD interaction in $NaBa_2Mn_3F_{11}$, the magnetic structure and magnetic excitation are studied by powder neutron diffraction and inelastic neutron scattering techniques.

In powder neutron diffraction experiment, the magnetic Bragg peaks indexed by the commensurate vector $\boldsymbol{k}_0 = (0, 0, 0)$, and incommensurate (IC) vectors $\boldsymbol{k}_1 = (0.3209, 0.3209, 0)$ and $\boldsymbol{k}_2 = (0.3338, 0.3338, 0)$ are observed. The magnetic structure analysis using the representation analysis identified the 120° structure of the tail-chase geometry, which is modulated by the IC vectors, is realized. The calculation of the ground state exhibits that the obtained 120° structure in $NaBa_2Mn_3F_{11}$ is selected by the MDD interaction.

In powder inelastic neutron scattering experiment, a spin wave excitation with a dispersionless spectrum around 0.2 meV are observed. The calculated magnetic excitation based on the linear spin wave theory reveals that the observed dispersionless spectrum is quantitatively explained by the zero-energy mode lifted by the MDD interaction. Consequently, the realization of the tail-chase 120° structure and zero-energy mode leads that $NaBa_2Mn_3F_{11}$ is a rare compound realizing the classical Kagome antiferromagnet having the MDD interaction.

This thesis consists of following chapters;

In Chapter 1, backgrounds for this study are introduced, and relevant previous studies are explained.

In Chapter 2, neutron scattering technique which is main experimental method in this study is denoted.

In Chapter 3, the study on the pressure-induced quantum phase transition in the singlet ground state magnet $CsFeCl_3$ is shown.

In Chapter 4, the study on the magnetic structure and magnetic excitation in the Kagome antiferromagnet $NaBa_2Mn_3F_{11}$ is shown.

In Chapter 5, this study is concluded and the outlook for the future is described.

# Chapter 1

# Backgrounds for study

## 1.1 Basic theory of spin system

Isolated magnetic ion

Magnetic properties in materials originate from orbital angular momentum $\hbar\boldsymbol{l}$ and spin angular momentum $\hbar\boldsymbol{s}$ of an electron. Their magnetic moments $\boldsymbol{\mu}_{\mathrm{o}}$ and $\boldsymbol{\mu}_{\mathrm{s}}$ are expressed as

$$\boldsymbol{\mu}_{\mathrm{o}} = -\mu_{\mathrm{B}}\boldsymbol{l} \tag{1.1}$$

$$\boldsymbol{\mu}_{\mathrm{s}} = -g\mu_{\mathrm{B}}\boldsymbol{s}, \tag{1.2}$$

where $\mu_{\mathrm{B}} = e\hbar/2m_{\mathrm{e}}$ is the Bohr magneton. $g$ is a constant known as the $g$-factor, which is usually given by $g \simeq 2$. Since the magnetic moments are vanished one another for closed shell in an atom, a magnetic moment of an unpaired electron in an incomplete shell is responsible for the magnetic properties.

Electronic state including orbital and spin moment in an isolated atom is determined by Coulomb repulsion in a single atom, spin-obit interaction, and crystal electric field. The Coulomb repulsion in the single atom leads to Hund's rule which determines $LS$-multiplet at ground state. The spin-orbit interaction comes from a relativistic interaction between a spin moment and an internal magnetic field, and is given by

$$\mathcal{H}_{LS} = \lambda\left(\boldsymbol{L}\cdot\boldsymbol{S}\right), \tag{1.3}$$

where $\boldsymbol{L}$ and $\boldsymbol{S}$ are total orbital and spin angular momentums, respectively. The spin-obit interaction plays a key role to connect a spin space to a real space, and originates the magnetic anisotropy determining the spin direction. In addition, the total orbital and spin angular momentums $\boldsymbol{L}$, $\boldsymbol{S}$ are not preserved because of the spin-orbit interaction. Consequently, the electronic state is labeled by a total angular momentum $\boldsymbol{J}$.

The crystal electric field derives from electric fields generated by ligands surrounding the magnetic ion, which is expressed by

$$V_{\mathrm{crystal}}(\boldsymbol{r}) = \sum_i \frac{Ze^2}{|\boldsymbol{R}_i - \boldsymbol{r}|}, \tag{1.4}$$

where $\boldsymbol{r}$ and $\boldsymbol{R}_i$ are position vectors of the magnetic ion and ligands, respectively. The $Z$ is the number of the ligands. As the crystal electric field couples with orbital angular momentum, it affects the orbital state. The eigenstate of the orbital depends on the symmetry of the environment. In many transition compounds, a transition metal of the magnetic ion locates at the center of an octahedron with anions such as oxygen. In this case, the $d$ orbitals in octahedral environment are divided into two classes: threefold $T_{2g}$ orbitals and twofold $E_g$ orbitals.

### Exchange interaction

In general, two magnetic moments $\boldsymbol{\mu}_1$ and $\boldsymbol{\mu}_2$ separated by a vector $\boldsymbol{r}_{12}$ have an energy due to the magnetic dipole-dipole (MDD) interaction, which is represented by

$$\mathcal{H}_{\mathrm{MDD}} = \frac{\mu_0}{4\pi}\left[\frac{\boldsymbol{\mu}_1\cdot\boldsymbol{\mu}_2}{r_{12}^3} - 3\frac{(\boldsymbol{\mu}_1\cdot\boldsymbol{r}_{12})\,(\boldsymbol{\mu}_2\cdot\boldsymbol{r}_{12})}{r_{12}^5}\right]. \tag{1.5}$$

The MDD interaction $\mathcal{H}_{\mathrm{MDD}}$ is estimated to be $\sim 3\times10^{-2}$ K when the spin $S = 1/2$ and the distance between the magnetic ions is 3 Å which is a usual distance in a crystal. As the MDD interaction is small compared with other interactions, it is usually ignored in the spin system.

The main interaction in the spin system is an exchange interaction. The exchange interaction is generated by antisymmetry of fermion and Coulomb repulsion, which means that it comes from quantum effect. The exchange interaction between electrons in a crystal is derived from the Hubbard model , which is expressed by

$$\mathcal{H} = \sum_{ij}\sum_{s} b_{ij}a_{js}^{\dagger}a_{is} + U\sum_{i} a_{i\uparrow}^{\dagger}a_{i\uparrow}a_{i\downarrow}^{\dagger}a_{i\downarrow}. \tag{1.6}$$

$b_{ij}$ is a hopping energy from $i$-th site to $j$-th site, and $U$ is a Coulomb energy. The hopping and Coulomb energies are defined by the Wannier function $w_i(\boldsymbol{r})$ as follow:

$$b_{ij} = \int d\boldsymbol{r} w_j^*(\boldsymbol{r})\mathcal{H}_{\mathrm{crystal}}w_i(\boldsymbol{r}), \tag{1.7}$$

$$U = \int d\boldsymbol{r}_1 d\boldsymbol{r}_2 |w_j(\boldsymbol{r}_1)|^2 \frac{e^2}{r_{12}}|w_i(\boldsymbol{r}_1)|^2, \tag{1.8}$$

where $\mathcal{H}_{\mathrm{crystal}}$ is the crystal potential between $w_i(\boldsymbol{r})$ and $w_j(\boldsymbol{r})$. In case of an insulator, the hopping energy $b_{ij}$ is much smaller than the Coulomb energy $U$. From calculations of the first and second perturbation in $U \gg |b_{ij}|$, the exchange interactions are given by

$$\mathcal{H}_{\mathrm{ex}(i,j)}^{(1)} = -J_{ij}^{(1)}\left(\frac{1}{2} + 2\boldsymbol{s}_j\cdot\boldsymbol{s}_i\right), \tag{1.9}$$

$$\mathcal{H}_{\mathrm{ex},(i,j)}^{(2)} = -2J_{ij}^{(2)}\left(\frac{1}{2} - 2\boldsymbol{s}_i\cdot\boldsymbol{s}_j\right), \tag{1.10}$$

where

$$J_{ij}^{(1)} = \int d\boldsymbol{r}_1 d\boldsymbol{r}_2 w_j^*(\boldsymbol{r}_1)w_i^*(\boldsymbol{r}_2)\frac{e^2}{r_{12}}w_i(\boldsymbol{r}_1)w_j(\boldsymbol{r}_2), \tag{1.11}$$

$$J_{ij}^{(2)} = \frac{|b_{ij}|^2}{U}. \tag{1.12}$$

The first interaction is a direct exchange interaction, and second one is an indirect exchange interaction which is called the superexchange interaction. The general expression of the exchange interaction is represented by

$$\mathcal{H}_{\mathrm{ex}} = -J_{ij}\boldsymbol{S}_i\cdot\boldsymbol{S}_j. \tag{1.13}$$

### Magnetic anisotropy

The magnetic anisotropy originates from the spin-orbit interaction which connects a spin state to an orbital state. From the second-order perturbation of the spin-obit interaction, the single-ion anisotropy is generally given by

$$\mathcal{H}_{\mathrm{single}} = D\left(S^z\right)^2 + E\left\{\left(S^x\right)^2 - \left(S^y\right)^2\right\}. \tag{1.14}$$

The $E$ term is vanished when the spin system has threefold, fourfold, and sixfold rotational symmetry along the $z$-axis. When we consider the case of $E = 0$, the spin favors to align parallel to the $z$-axis in case of the $D < 0$. This anisotropy is called an easy-axis anisotropy In contrast, the spin favors to align perpendicular to the $z$-axis for $D > 0$ and $E = 0$, which is called an easy-plane anisotropy.

In addition to the single-ion anisotropy, perturbation of the spin-orbit interaction gives an anisotropic interaction, which is generally expressed by

$$\mathcal{H}_{\mathrm{AE}} = -\sum_{\mu,\nu} S_i^{\mu} J_{ij}^{\mu\nu} S_i^{\nu}. \tag{1.15}$$

In particular, when it has no space inversion symmetry, it gives

$$\mathcal{H}_{\mathrm{DM}} = \boldsymbol{D}_{ij} \cdot (\boldsymbol{S}_i \times \boldsymbol{S}_j), \tag{1.16}$$

which is known as Dzyaloshinskii-Moriya interaction.

The Hamiltonian including the interactions and anisotropies, which are denoted above, is called Spin Hamiltonian and plays a role to determine the spin state and originates a diverse magnetic properties.

## 1.2 Magnetic ordering

The ground state is determined by minimizing the spin Hamiltonian. In most of the magnetic materials, the ground state at a low temperature shows a magnetic long-range order, in which the spins are arranged to minimize the energy of the system.

When we assume that the spin $\boldsymbol{S_m}$ is a classical vector, the magnetic structure at zero temperature can be found using following method. Let us consider a Hamiltonian in which the spins are on a Bravais lattice with one spin per unit cell. The Hamiltonian is

$$\mathcal{H} = \sum_{\boldsymbol{m},\boldsymbol{n}} J(\boldsymbol{m} - \boldsymbol{n}) \boldsymbol{S_m} \cdot \boldsymbol{S_n}, \tag{1.17}$$

where $\boldsymbol{m}$ and $\boldsymbol{n}$ are the lattice vectors. The Fourier transformation of the spin $\boldsymbol{S_m}$ is defined by

$$\boldsymbol{S_m} = S \sum_{\boldsymbol{q}} \boldsymbol{S_q} e^{i\boldsymbol{q}\cdot\boldsymbol{m}}, \tag{1.18}$$

$$\boldsymbol{S_q} = \frac{1}{NS} \sum_{\boldsymbol{m}} \boldsymbol{S_m} e^{-i\boldsymbol{q}\cdot\boldsymbol{m}}, \tag{1.19}$$

where $N$ is the number of the unit cell.

From the Fourier transformation, the Hamiltonian is represented as follow:

$$\mathcal{H} = NS^2 \sum_{\boldsymbol{q}} \mathcal{J}(\boldsymbol{q}) \boldsymbol{S_q} \cdot \boldsymbol{S_{-q}}, \tag{1.20}$$

where

$$\mathcal{J}(\boldsymbol{q}) = \sum_{\boldsymbol{m}} J(\boldsymbol{m}) e^{i\boldsymbol{q}\cdot\boldsymbol{m}}. \tag{1.21}$$

The magnetic structure can be obtained by searching $\boldsymbol{q}$ to minimize $\mathcal{J}(\boldsymbol{q})$.

For example, a stacked square lattice model is considered as

$$\mathcal{H} = \sum_{xy-\mathrm{plane}} J_1 \boldsymbol{S_m} \cdot \boldsymbol{S_n} + \sum_{z-\mathrm{axis}} J_2 \boldsymbol{S_m} \cdot \boldsymbol{S_n}, \tag{1.22}$$

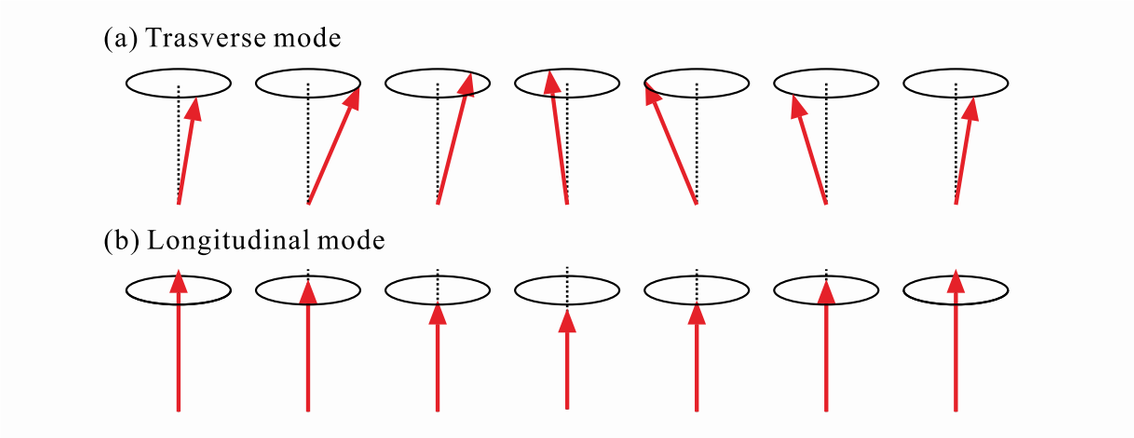


Figure 1.1 Schematic of spin wave for (a) transverse mode and (b) longitudinal mode.

where $J_1$ is antiferromagnetic interaction in the square lattice and $J_2$ is ferromagnetic interaction along the layer. The $\mathcal{J}(\boldsymbol{q})$ is represented by

$$\mathcal{J} = 2J_1(\cos q_x + \cos q_y) + 2J_2 \cos q_z, \tag{1.23}$$

where the lattice constant is defined by 1 for simplicity. Since signs of $J_1$ and $J_2$ are positive and negative, it is found that a wave vector $\boldsymbol{q} = (\pi, \pi, 0)$ gives the minimum energy. The spins are antiferromagnetically aligned along the $x$ and $y$-axis and ferromagnetically aligned along the $z$-axis.

The general expression of Eq. (1.20) in a non-Bravais lattice is written by

$$\mathcal{H} = NS^2 \sum_{\boldsymbol{q}} \sum_{i,j} \sum_{\alpha,\beta} S^{\alpha}_{i,\boldsymbol{q}} \mathcal{J}^{\alpha\beta}_{ij}(\boldsymbol{q}) S^{\beta}_{j,-\boldsymbol{q}}, \tag{1.24}$$

where $i, j$ are labels of the magnetic ions in the unit cell, and $\alpha, \beta$ are Cartesian coordinations $x, y, z$. In this case, the ground state is obtained by diagonalizing $\mathcal{J}^{\alpha\beta}_{ij}(\boldsymbol{q})$ and searching $\boldsymbol{q}$ to minimize the eigenvalues.

## 1.3 Spin wave excitation

An elementary excitation from the ordered state in the spin system is represented by the wave of the spin fluctuation. This excitation is called *spin wave* and its quantized quasi-particle is a magnon. The spin fluctuations are classified by phase and amplitude of the spin moment. The phase fluctuation corresponds to the transverse mode, and amplitude fluctuation corresponds to the longitudinal mode in the spin wave as illustrated in Figs. 1.1(a).

The most conventional way to calculate the spin wave excitation is the linear spin wave theory. In the linear spin wave theory, the spin operator $\boldsymbol{S}_i$ is expressed by using Holstein-Primakoff transformation as

$$\begin{cases} S^z_i = S - a^{\dagger}_i a_i \\ S^-_i = \sqrt{2S} a^{\dagger}_i \left(1 - \dfrac{a^{\dagger}_i a_i}{2S}\right)^{\frac{1}{2}} \\ S^+_i = \sqrt{2S} \left(1 - \dfrac{a^{\dagger}_i a_i}{2S}\right)^{\frac{1}{2}} a \end{cases}, \tag{1.25}$$

where $a^\dagger, a$ are bosonic creation-annihilation operators satisfying the commutation relation as

$$[a_i, a_j^\dagger] = \delta_{ij}. \tag{1.26}$$

Spin wave in ferromagnet

Let us denote spin wave excitation of a ferromagnet in a Heisenberg model

$$\mathcal{H} = -\sum_{i,j} J_{ij} \boldsymbol{S}_i \cdot \boldsymbol{S}_j. \tag{1.27}$$

From Holstein-Primakoff transformation, the Hamiltonian is represented as follow:

$$\mathcal{H} = E_0 + \sum_{\boldsymbol{q}} \hbar\omega_{\boldsymbol{q}} a_{\boldsymbol{q}}^\dagger a_{\boldsymbol{q}}, \tag{1.28}$$

$$E_0 = -N\mathcal{J}(0)S^2, \tag{1.29}$$

where

$$\begin{cases} a_{\boldsymbol{q}} = \dfrac{1}{\sqrt{N}} \displaystyle\sum_i e^{-i\boldsymbol{q}\cdot\boldsymbol{R}_i} a_i \\ a_{\boldsymbol{q}}^\dagger = \dfrac{1}{\sqrt{N}} \displaystyle\sum_i e^{i\boldsymbol{q}\cdot\boldsymbol{R}_i} a_i^\dagger \end{cases}. \tag{1.30}$$

The dispersion relation is given by

$$\hbar\omega_{\boldsymbol{q}} = S\left[\mathcal{J}(0) - \mathcal{J}(\boldsymbol{q})\right], \tag{1.31}$$

$$\mathcal{J}(\boldsymbol{q}) = \sum_{i,j} J_{ij} e^{-i\boldsymbol{q}\cdot\boldsymbol{\rho}_{ij}} \quad (\boldsymbol{\rho}_{ij} = \boldsymbol{R}_i - \boldsymbol{R}_j). \tag{1.32}$$

For small $\boldsymbol{q}$ meaning long wavelength excitation, we have

$$\begin{aligned} \hbar\omega(\boldsymbol{q})/S &= \mathcal{J}(0) - \mathcal{J}(\boldsymbol{q}) \\ &= \sum_{\boldsymbol{\rho}_{ij}} J_{ij} - \sum_{\boldsymbol{\rho}_{ij}} J_{ij} e^{-i\boldsymbol{q}\cdot\boldsymbol{\rho}_{ij}} \\ &\simeq \sum_{\boldsymbol{\rho}_{ij}} J_{ij} - \sum_{\boldsymbol{\rho}_{ij}} J_{ij} \left\{ 1 - \frac{1}{2} \left( \boldsymbol{q} \cdot \boldsymbol{\rho}_{ij} \right)^2 \right\}. \end{aligned} \tag{1.33}$$

The spin wave energy for small $\boldsymbol{q}$ is

$$\mathcal{H} = E_0 + \frac{S}{2} \sum_{\boldsymbol{\rho}_{ij}} J_{ij} \left( \boldsymbol{q} \cdot \boldsymbol{\rho}_{ij} \right)^2 \quad (q \ll 1). \tag{1.34}$$

Thus, in the ferromagnet the spin wave dispersion for small $\boldsymbol{q}$ is proportional to $q^2$.

Spin wave in antiferromagnet

Next let us denote the spin wave excitation in a Heisenberg antiferromagnet. Assuming that the ground state is Néel state in which the spins are antiferromagnetically aligned, the Heisenberg Hamiltonian for two sublattices $A$ and $B$ is expressed as

$$\mathcal{H} = -\sum_{i\in\mathrm{A}} \sum_{j\in\mathrm{A}} J_{ij} \boldsymbol{S}_i \cdot \boldsymbol{S}_j - \sum_{i\in\mathrm{B}} \sum_{j\in\mathrm{B}} J_{ij} \boldsymbol{S}_i \cdot \boldsymbol{S}_j - 2 \sum_{i\in\mathrm{A}} \sum_{j\in\mathrm{B}} J_{ij} \boldsymbol{S}_i \cdot \boldsymbol{S}_j. \tag{1.35}$$

From Holstein-Primakoff transformation, the spin operators in each sublattice are represented by

$$\text{sublattice}-A \qquad \begin{cases} S^z = S - a^\dagger a \\ S^- = \sqrt{2S} a^\dagger \left(1 - \dfrac{a^\dagger a}{2S}\right)^{\frac{1}{2}} \\ S^+ = \sqrt{2S} \left(1 - \dfrac{a^\dagger a}{2S}\right)^{\frac{1}{2}} a \end{cases}, \tag{1.36}$$

$$\text{sublattice}-B \qquad \begin{cases} S^z = -S + b^\dagger b \\ S^+ = \sqrt{2S} b^\dagger \left(1 - \dfrac{b^\dagger b}{2S}\right)^{\frac{1}{2}} \\ S^- = \sqrt{2S} \left(1 - \dfrac{b^\dagger b}{2S}\right)^{\frac{1}{2}} b \end{cases}, \tag{1.37}$$

where $a_i^\dagger, a_i$ and $b_i^\dagger, b_i$ are bosonic creation-annihilation operators. The Hamiltonian is expressed by the bosonic operators as follow:

$$\mathcal{H} = \frac{1}{2} N \mathcal{J}(\boldsymbol{Q}) S^2 + \sum_{\boldsymbol{q}} \left[ A(\boldsymbol{q}) \left( a_{\boldsymbol{q}}^\dagger a_{\boldsymbol{q}} + b_{\boldsymbol{q}}^\dagger b_{\boldsymbol{q}} \right) + B(\boldsymbol{q}) \left( a_{\boldsymbol{q}} b_{\boldsymbol{q}} + a_{\boldsymbol{q}}^\dagger b_{\boldsymbol{q}}^\dagger \right) \right], \tag{1.38}$$

$$A(\boldsymbol{q}) = \frac{S}{2} \left[ \mathcal{J}(\boldsymbol{q}) + \mathcal{J}(\boldsymbol{q} + \boldsymbol{Q}) - 2\mathcal{J}(\boldsymbol{Q}) \right], \tag{1.39}$$

$$B(\boldsymbol{q}) = \frac{S}{2} \left[ \mathcal{J}(\boldsymbol{q}) - \mathcal{J}(\boldsymbol{q} + \boldsymbol{Q}) \right], \tag{1.40}$$

where $\boldsymbol{Q}$ is the magnetic propagation vector. To diagonalize the Hamiltonian, the Bogoliubov transformation is carried out. The Bogoliubov transformation is expressed by

$$\begin{cases} \alpha_{\boldsymbol{q}} = a_{\boldsymbol{q}} \cosh\theta_{\boldsymbol{q}} + b_{\boldsymbol{q}}^\dagger \sinh\theta_{\boldsymbol{q}}, \\ \beta_{\boldsymbol{q}}^\dagger = a_{\boldsymbol{q}} \sinh\theta_{\boldsymbol{q}} + b_{\boldsymbol{q}} \cosh\theta_{\boldsymbol{q}} \end{cases} \tag{1.41}$$

$$\begin{cases} a_{\boldsymbol{q}} = \alpha_{\boldsymbol{q}} \cosh\theta_{\boldsymbol{q}} - \beta_{\boldsymbol{q}}^\dagger \sinh\theta_{\boldsymbol{q}} \\ b_{\boldsymbol{q}}^\dagger = -\alpha_{\boldsymbol{q}} \sinh\theta_{\boldsymbol{q}} + \beta_{\boldsymbol{q}}^\dagger \cosh\theta_{\boldsymbol{q}} \end{cases}, \tag{1.42}$$

where $\theta_{\boldsymbol{q}}$ satisfies

$$\cosh^2\theta_{\boldsymbol{q}} - \sinh^2\theta_{\boldsymbol{q}} = 1. \tag{1.43}$$

Then the diagonalized Hamiltonian is expressed as

$$\mathcal{H} = \frac{N}{2} \mathcal{J}(\boldsymbol{Q}) S(S+1) + \sum_{\boldsymbol{q}} \hbar\omega_{\boldsymbol{q}} \left( \alpha_{\boldsymbol{q}}^\dagger \alpha_{\boldsymbol{q}} + \beta_{\boldsymbol{q}}^\dagger \beta_{\boldsymbol{q}} + 1 \right). \tag{1.44}$$

The spin wave dispersion $\hbar\omega_{\boldsymbol{q}}$ is given by

$$\begin{aligned} \hbar\omega_{\boldsymbol{q}} &= A(\boldsymbol{q}) \cosh 2\theta_{\boldsymbol{q}} - B(\boldsymbol{q}) \sinh 2\theta_{\boldsymbol{q}} \\ &= \sqrt{\left[A(\boldsymbol{q}) + B(\boldsymbol{q})\right] \left[A(\boldsymbol{q}) - B(\boldsymbol{q})\right]} \qquad (1.45) \\ &= S\sqrt{\left[\mathcal{J}(\boldsymbol{q}) - \mathcal{J}(\boldsymbol{Q})\right] \left[\mathcal{J}(\boldsymbol{q} + \boldsymbol{Q}) - \mathcal{J}(\boldsymbol{Q})\right]}. \qquad (1.46) \end{aligned}$$

For small $\boldsymbol{q}$, we have

$$\begin{aligned}\mathcal{J}(\boldsymbol{q}+\boldsymbol{Q})-\mathcal{J}(\boldsymbol{Q})\mid_{q\to 0} &\simeq \mathcal{J}(\boldsymbol{Q})+\sum_{\alpha}\left.\frac{\partial\mathcal{J}(\boldsymbol{q}+\boldsymbol{Q})}{\partial q_\alpha}\right|_{q=0} q_\alpha+\frac{1}{2}\sum_{\alpha,\beta}\left.\frac{\partial^2\mathcal{J}(\boldsymbol{q}+\boldsymbol{Q})}{\partial q_\alpha\partial q_\beta}\right|_{q=0} q_\alpha q_\beta \quad -\mathcal{J}(\boldsymbol{Q})\\ &= \frac{1}{2}\sum_{\alpha,\beta}\left.\frac{\partial^2\mathcal{J}(\boldsymbol{q}+\boldsymbol{Q})}{\partial q_\alpha\partial q_\beta}\right|_{q=0} q_\alpha q_\beta,\\ \mathcal{J}(\boldsymbol{q})-\mathcal{J}(\boldsymbol{Q})\mid_{q\to 0} &\simeq \mathcal{J}(0)-\mathcal{J}(\boldsymbol{Q}),\end{aligned}$$

where the first order of $q$ is ignored due to space inversion symmetry. Then the spin wave dispersion for small $\boldsymbol{q}$ is represented by

$$\begin{aligned}\hbar\omega_{\boldsymbol{q}} &= S\sqrt{[\mathcal{J}(\boldsymbol{q})-\mathcal{J}(\boldsymbol{Q})]\,[\mathcal{J}(\boldsymbol{q}+\boldsymbol{Q})-\mathcal{J}(\boldsymbol{Q})]}\\ &\propto |\boldsymbol{q}|.\end{aligned} \tag{1.47}$$

Thus, in the antiferromagnet the spin wave dispersion for small $\boldsymbol{q}$ is proportional to $q$.

## 1.4 Quantum phase transition

In general, phase transitions occur in materials by varying the temperature. For example, water becomes ice, and paramagnet becomes ferromagnet by the decrease of the temperatures. This transition is caused by a competition between the thermal fluctuation and ordering. The thermal fluctuation at high temperature prevents from ordering the material. At low temperature, in contrast, the microscopic interaction overcomes the thermal fluctuation, and the ordering occurs. According to above mechanism, the phase transition does not occurs at zero temperature because there is no thermal fluctuation. However, the phase transition occurs by quantum fluctuation at zero temperature. This phase transition is called the quantum phase transition (QPT) to distinguish from the phase transition due to the thermal fluctuation.

The QPT is a transition between different ground states induced by quantum fluctuation, which is controlled by external parameters such as magnetic field, pressure, and chemical doping [1, 2]. The quantum fluctuation originally comes from duality of wave (itinerancy) and particle (localization). The itinerancy corresponds to kinetic energy, which prevents from the ordering. In contrast, the localization corresponds to potential energy, which promotes the ordering. The competition between the itinerancy and localization determines the extent of the quantum fluctuation. When one varies a parameter $g$ controlling the quantum fluctuation, the singular point appears in which the long-range order is broken, and quantum disorder (QD) is realized. This is called quantum critical point (QCP).

The schematic diagram of the QPT is shown in Fig. 1.2. Since the quantum fluctuation is enhanced in the vicinity of the QCP, one has a chance to observe non-trivial phenomena around the QCP. Up to now, the QPT provides the unsolved topics in many condensed matter systems [3]; the 3D Ising ferromagnet in the transverse magnetic field in the rare-earth magnetic insulator [4, 5], the non-Fermi liquid behavior and superconductivity in the high-temperature superconductors [6, 7, 8, 9] and the heavy fermion metals [10, 11], the metal-insulator transition in the two-dimensional electron systems [12], and superfluid-Mott insulator transition in the ultracold atom systems [13, 14]. The QPT is therefore an intriguing topic in condensed matter physics.

In this section, the QPT is briefly described using a quantum rotor model and collective excitation based on the quantum field theory. In addition, a spin dimer system is shown as a well-studied example. Then a spin-1 antiferromagnet system with strong easy-plane anisotropy is explained.

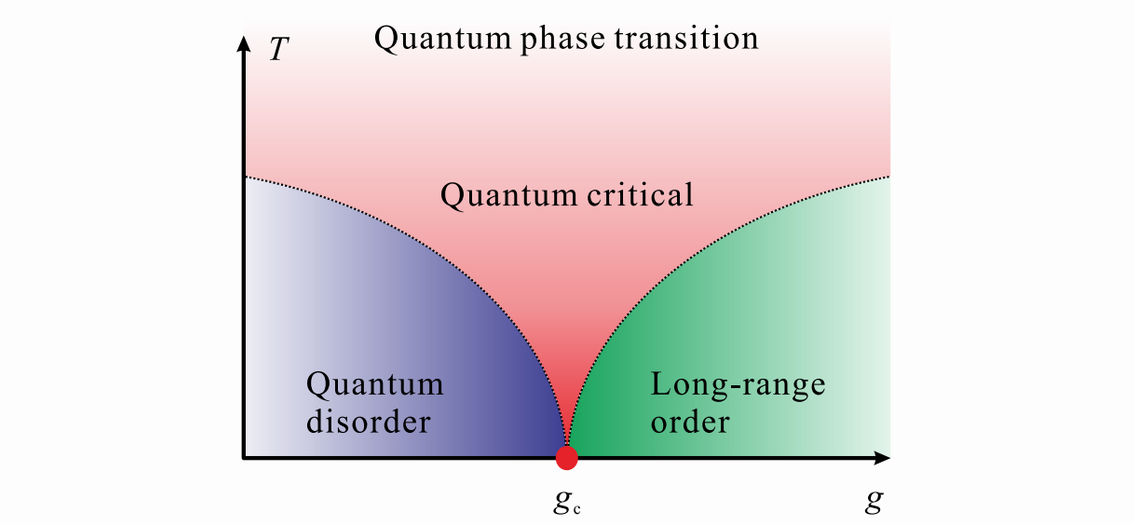


Figure 1.2 Schematic diagram of the phase diagram around Quantum critical point.

### 1.4.1 Quantum phase transition

Let us introduce the quantum rotor model to briefly describe the QPT [1]. The quantum rotor model is one of common models in the quantum spin system because each quantum rotor represents an effective quantum degree of freedom for the low energy states. Each rotor can be visualized as a particle constrained to move on the surface of $N$-dimensional sphere. An $N$-component unit vector $\hat{\boldsymbol{n}}_i$ represents the orientation of each rotor. The $\hat{\boldsymbol{n}}_i$ satisfies

$$\hat{\boldsymbol{n}}_i^2 = 1. \tag{1.48}$$

Each rotor has a momentum $\hat{\boldsymbol{p}}_i$ satisfying the commutation relations

$$[\hat{n}_\alpha, \hat{p}_\beta] = i\delta_{\alpha\beta}, \tag{1.49}$$

where $\alpha, \beta = 1, \ldots, N$ are the degree of freedom of the rotor orientation. The rotor angular momentum is defined by

$$\hat{L}^\gamma = \frac{1}{2}\epsilon_{\alpha\beta\gamma}\left(\hat{n}^\alpha \hat{p}^\beta - \hat{n}^\beta \hat{p}^\alpha\right), \tag{1.50}$$

where $\epsilon_{\alpha\beta\gamma}$ is a totally antisymmetric tensor with $\epsilon_{123} = 1$.

When we use the rotor $\hat{\boldsymbol{n}}_i$ and the rotor angular momentum $\hat{\boldsymbol{L}}_i$, the quantum rotor model is expressed as follow:

$$\mathcal{H}_R = \frac{Jg}{2}\sum_i \hat{\boldsymbol{L}}_i^{\,2} - J\sum_{\langle ij\rangle} \hat{\boldsymbol{n}}_i \cdot \hat{\boldsymbol{n}}_j, \tag{1.51}$$

where a coupling $J$ is positive. The first term represents the kinetic energy of the rotors, and the second term is a coupling of the rotors corresponding to the potential energy. To minimize the coupling energy, the all rotors must be oriented along the same direction, meaning the magnetic ordering. In contrast, the kinetic energy of the rotor angular momentum is minimized when the orientation of the rotor are maximally uncertain. Then the rotors are not oriented along the specific direction. This means that the kinetic term prefers a quantum paramagnetic state. Thus, the coupling (potential) energy competes with the kinetic energy, which originates from just the quantum fluctuation. The $g$ is a parameter of this competition.

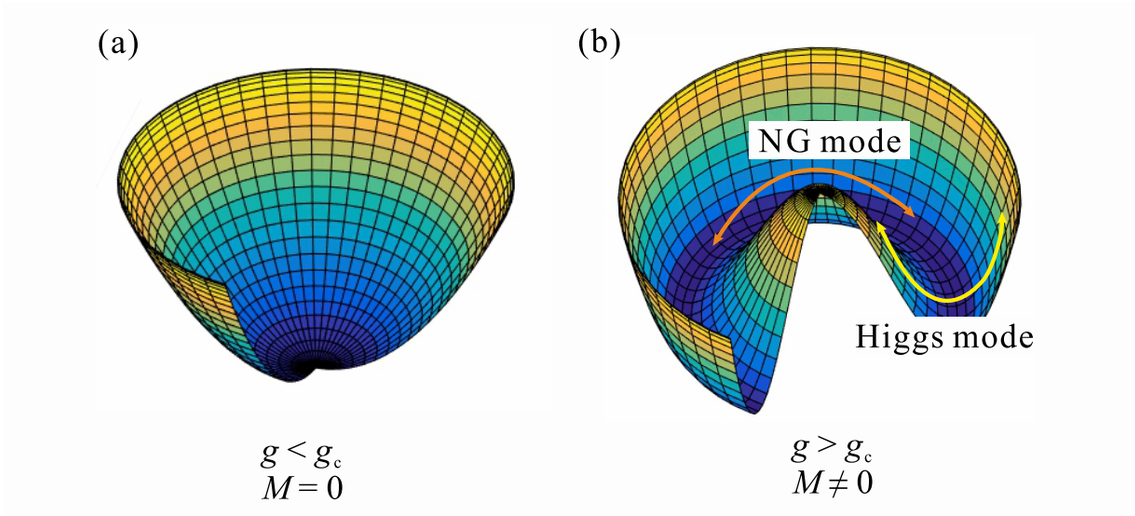


Figure 1.3 Schematic diagrams of mean-field ground state energy in (a) disordered state and (b) ordered state.

The kinetic energy becomes dominant in the $g \gg 1$ and the rotors are paramagnetic. In the $g \ll 1$, the coupling energy takes over the kinetic energy and the magnetic ordered state is realized. There is a critical point $g_c$ in which the QPT occurs between the paramagnetic and magnetic ordered phases. In a spin dimer system as an example, the kinetic and potential terms correspond to intra- and inter-dimer interaction. In addition, in a spin-1 antiferromagnet with a strong easy-plane anisotropy, the easy-plane type single-ion anisotropy is regarded as the kinetic term and spin-spin coupling is the potential term.

### 1.4.2 Collective excitation around quantum critical point

Collective excitation near the QCP in the ordered phase is described by phase and amplitude fluctuation of an order parameter. While the phase fluctuation is known as Nambu-Goldstone (NG) mode, the amplitude fluctuation is called Higgs mode, which is analogue to Higgs boson in particle physics.

Let us briefly describe the low energy collective excitations in the vicinity of the QCP based on Landau theory and quantum field theory. For the quantum field theory, a coarse-grained field $\phi_\alpha(x,t)$ is conveniently used, which is defined by

$$\phi_\alpha(x,t) \sim \sum_{i \in \mathcal{N}(x)} n_{i\alpha}(t), \tag{1.52}$$

where the index $\alpha = 1, \ldots, N$ is the degree of freedom of the rotor orientation, and the overall $\phi_\alpha$ is normalized. The $x$ is a position in $d$-dimensional space, and $\mathcal{N}(x)$ is a coarse-graining neighborhood of $x$. The rotors $\boldsymbol{n}_i$ is roughly grained by introducing the field $\phi_\alpha(x,t)$.

Based on Landau theory, the Hamiltonian in the continuum quantum model is represented as

$$\mathcal{H} = \int d^d x \sum_{\alpha=1}^{N} \left[ \frac{1}{2} \left\{ \pi_\alpha^2 + c^2 (\nabla_x \phi_\alpha)^2 + r \phi_\alpha^2(x) \right\} + \frac{u}{4!} \left( \phi_\alpha^2(x) \right)^2 \right], \tag{1.53}$$

where $\pi_\alpha(x,t)$ is the canonical momentum to the field $\phi_\alpha$. The first and second terms represent time and spatial fluctuations of the field $\phi_\alpha$. The third and fourth terms are given by a polynomial expansion for a local effective potential $V(\phi_\alpha^2)$. The magnetic phases are classified by the value

of $r$; $r > 0$ is at the quantum paramagnetic phase, $r = 0$ is at the QCP, and $r < 0$ is at the magnetic ordered phase.

In the paramagnetic phase, $r > 0$, the effective local potential in Eq. (1.53) is minimized at $\phi_\alpha = 0$ as shown in Fig. 1.3(a). The low-energy excitations are small fluctuations around $\phi_\alpha = 0$. Hence, the quadratic $u$ term can be ignored, and the Hamiltonian Eq. (1.53) is simply diagonalized as

$$\mathcal{H} = \int \frac{d^d k}{(2\pi)^d} \varepsilon_k \sum_{\alpha=1}^{N} \left[ a_\alpha^\dagger(\boldsymbol{k}) a_\alpha(\boldsymbol{k}) + \frac{1}{2} \right]. \tag{1.54}$$

Then the energy of the normal modes is

$$\varepsilon_k = \sqrt{c^2 k^2 + r}. \tag{1.55}$$

Here, in order to denote the normal excitation mode in each phase, we used harmonic oscillator operators expressed by

$$\begin{aligned} \phi_\alpha(x) &= \int \frac{d^d k}{(2\pi)^d} \frac{1}{\sqrt{2\varepsilon_k}} \left( a_\alpha(\boldsymbol{k}) e^{i\boldsymbol{k}\cdot\boldsymbol{x}} + a_\alpha^\dagger(\boldsymbol{k}) e^{-i\boldsymbol{k}\cdot\boldsymbol{x}} \right), \\ \pi_\alpha(x) &= -i \int \frac{d^d k}{(2\pi)^d} \frac{\varepsilon_k}{\sqrt{2}} \left( a_\alpha(\boldsymbol{k}) e^{i\boldsymbol{k}\cdot\boldsymbol{x}} - a_\alpha^\dagger(\boldsymbol{k}) e^{-i\boldsymbol{k}\cdot\boldsymbol{x}} \right), \end{aligned} \tag{1.56}$$

where $\varepsilon_k$ is the energy of the normal mode. $a_\alpha^\dagger(\boldsymbol{k})$ and $a_\alpha(\boldsymbol{k})$ are creation and annihilation operators satisfying the commutation relation:

$$\begin{aligned} \left[ a_\alpha(\boldsymbol{k}), a_\beta^\dagger(\boldsymbol{k}') \right] &= \delta_{\alpha\beta} (2\pi)^d \delta^d(\boldsymbol{k} - \boldsymbol{k}'), \\ \left[ a_\alpha(\boldsymbol{k}), a_\beta(\boldsymbol{k}') \right] &= 0. \end{aligned} \tag{1.57}$$

The collective excitation in the paramagnetic phase has an energy gap of $\Delta = \sqrt{r}$. The energy gap is softened by decrease of the $r$ and becomes zero at $r = 0$. Thus, the energy of the normal modes at the QCP becomes a gapless dispersion as

$$\varepsilon_k = ck. \tag{1.58}$$

In the magnetic ordered phase, i.e., $r < 0$, the potential in Eq. (1.53) is a Mexican hat-like potential as shown in Fig. 1.3(b), and has a minimum at $\phi_\alpha = m_0 \delta_{\alpha,1}$. The $m_0$ is given by

$$m_0 = \sqrt{\frac{-6r}{u}}. \tag{1.59}$$

The direction of the ordered magnetic moment has been arbitrarily selected along the $\alpha = 1$ direction. The field $\phi_\alpha$ is written as

$$\phi_\alpha(x) = m_0 \delta_{\alpha,1} + \tilde{\phi}_\alpha(x). \tag{1.60}$$

Considering quadratic order in the $\tilde{\phi}_\alpha$, the Hamiltonian Eq. (1.53) is computed as follow:

$$\begin{aligned} \mathcal{H} &= \frac{1}{2} \int d^d x \left\{ \sum_{\alpha=1}^{N} \left( \pi_\alpha^2 + c^2 (\nabla_x \tilde{\phi}_\alpha)^2 \right) + 2|r| \tilde{\phi}_1^2(x) \right\} \\ &= \frac{1}{2} \int d^d x \left\{ \left( \pi_1^2 + c^2 (\nabla_x \tilde{\phi}_1)^2 + 2|r| \tilde{\phi}_1^2(x) \right) + \sum_{\alpha=2}^{N} \left( \pi_\alpha^2 + c^2 (\nabla_x \tilde{\phi}_\alpha)^2 \right) \right\}. \end{aligned} \tag{1.61}$$

This is diagonalized by using Eq. (1.56), and two types of excitation are obtained:

$$\varepsilon_k = ck, \quad N-1 \text{ particles}, \tag{1.62}$$

$$\varepsilon_k = \sqrt{c^2k^2 + 2|r|}, \quad 1 \text{ particle}. \tag{1.63}$$

There are $N-1$ gapless modes and one gapped mode. The gapless modes are transverse oscillation of the $\phi_\alpha$ field, which correspond to the NG mode. In contrast, the gapped mode is longitudinal oscillation of the $\phi_1$ field, which is called the Higgs mode from the analogy of the Higgs boson in the particle physics. From the above derivation, $N-1$ NG modes and one Higgs mode appear in the ordered phase.

### 1.4.3 Higgs mode in condensed matter

The Higgs mode has attracted great interest for condensed matter physics in a few decades [15]. In particle physics, the Higgs boson appears in the amplitude fluctuation of the condensed Higgs field in the Standard Model, and has been discovered by F. Englert and P. W. Higgs in 1963 [16, 17], who won Nobel Prize in physics in 2013 for their remarkable work. Originally, their theory was inspired by the theory on the spontaneous symmetry breaking proposed by Y. Nambu [18, 19, 20] in 1960, who also won Nobel Prize in physics in 2008 for his pioneering work. Since the Nambu's theory derived from the analogy of the superconductivity theory, it was quite natural to anticipate the observation of the Higgs mode in the superconductor in condensed matter physics. In 1980, the Higgs mode was discovered in the superconductor $NbSe_2$ by means of Raman scattering for the first time [21].

After that, the investigation of the Higgs mode has been attracted in various materials such as superconductors [22, 23], charge-density-wave system [24, 25], and ultracold atom superfluid [26]. The quantum spin system is also one of the well-studied field for the Higgs mode. For example, a dimerized antiferromagnet $TlCuCl_3$ demonstrated a control of the Higgs mode by the pressure [27], and the quantum criticality was discussed [28]. In an Ising-like chain antiferromagnet $BaCo_2V_2O_8$, the longitudinal and transverse Zeeman ladder excitations were observed by inelastic neutron scattering [29]. Studies on a spin-orbit singlet antiferromagnet $Ca_2RuO_4$ [30] and a coupled latter antiferromagnet $C_9H_{18}N_2CuBr_4$ [31] were undertaken in order to discuss a decay of the Higgs mode to NG mode in the two-dimensional system.

To be exact, the Higgs mode only in the superconductor is analogous to the Higgs boson in particle physics from the point that gauge field (photon) obtains its mass (Meissner effect) by means of symmetry breaking. However, the study on Higgs mode coming from the spontaneous symmetry breaking in the condensed matter is important because understanding of the Higgs mode relates to the development of the quantum field theory. The investigation of the Higgs mode is therefore one of the central topics in the condensed matter physics.

### 1.4.4 Spin dimer system

Next let us denote a concrete example of QPT in the spin system, a spin dimer system [32]. The spin dimer system having $S = 1/2$ is the most common spin system in which the QPT occurs. The QPT in the dimer system is caused by competition between intra-dimer interaction and inter-dimer interaction. Here, the mean-field solution of the spin dimer system is explained. The following Hamiltonian is considered:

$$\begin{aligned}\mathcal{H} = &\sum_i J\boldsymbol{S}_{1,i}\cdot\boldsymbol{S}_{2,i} + \sum_{\langle i,j\rangle} J_1\left(\boldsymbol{S}_{1,i}\cdot\boldsymbol{S}_{1,j} + \boldsymbol{S}_{2,i}\cdot\boldsymbol{S}_{2,j}\right) \\ &+ \sum_{\langle i,j\rangle} J_2\left(\boldsymbol{S}_{1,i}\cdot\boldsymbol{S}_{1,j} + J_2\boldsymbol{S}_{2,i}\cdot\boldsymbol{S}_{2,j}\right) + \sum_{\langle i,j\rangle} J_3\boldsymbol{S}_{1,i}\cdot\boldsymbol{S}_{2,j},\end{aligned} \tag{1.64}$$

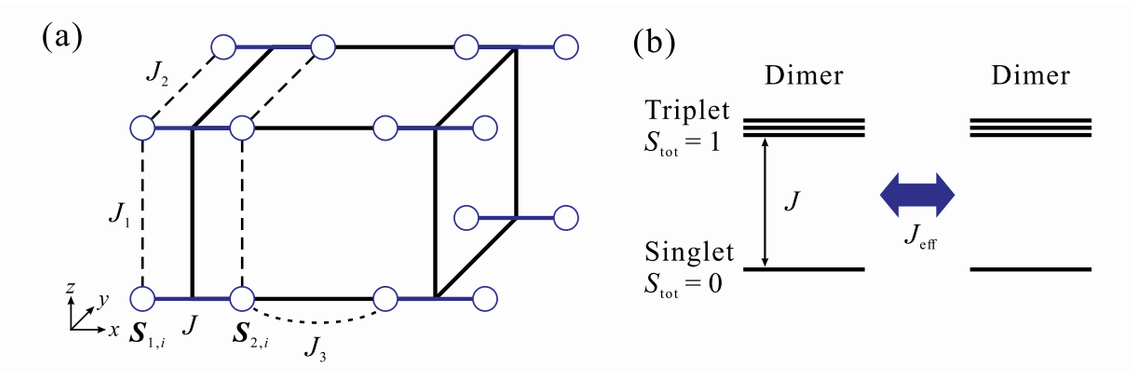


Figure 1.4 (a) Interaction paths of the dimer system. $J$ is intra-dimer interaction, and $J_1$, $J_2$, and $J_3$ are inter-dimer interactions. (b) Schematic diagram of spin dimer system.

where $\boldsymbol{S}_{1,i}$ and $\boldsymbol{S}_{1,i}$ represent the spin operator having spin 1/2 at the $i$-th site, and they form a dimer. $J$ is the antiferromagnetic intra-dimer interaction. $J_1$, $J_2$, and $J_3$ are inter-dimer interactions. It is assumed that $J_1$, $J_2$ and $J_3$ are antiferromagnetic. The interaction paths are shown in Fig. 1.4(a).

When the intra-dimer interaction $J$ is much stronger than the inter-dimer interaction, the non-magnetic singlet state $S_{\rm tot} = 0$ ($\boldsymbol{S}_{\rm tot} = \boldsymbol{S}_1 + \boldsymbol{S}_2$) is the ground state and the magnetic triplet state $S_{\rm tot} = 1$ is the excited state as shown in Fig. 1.4(b). According to Ref. [32], the singlet $|s\rangle$ and triplet $|t_x\rangle, |t_z\rangle, |t_y\rangle$ states are represented as follow:

$$|s\rangle = \frac{1}{\sqrt{2}}\left(|\uparrow\downarrow\rangle - |\downarrow\uparrow\rangle\right), \tag{1.65}$$

$$|t_x\rangle = \frac{-1}{\sqrt{2}}\left(|\uparrow\uparrow\rangle - |\downarrow\downarrow\rangle\right), \tag{1.66}$$

$$|t_y\rangle = \frac{i}{\sqrt{2}}\left(|\uparrow\uparrow\rangle + |\downarrow\downarrow\rangle\right), \tag{1.67}$$

$$|t_z\rangle = \frac{1}{\sqrt{2}}\left(|\uparrow\downarrow\rangle + |\downarrow\uparrow\rangle\right), \tag{1.68}$$

where $|S_1 S_2\rangle$ represents the spin state of the $S_1$-$S_2$ dimer. The $x$-, $y$-, and $z$-directions are shown in Fig. 1.4(a).

The singlet and triplet states are hybridized with increase of the inter-dimer interaction. This causes the magnetic long-range order. It is assumed that the ordered magnetic moments form a collinear magnetic structure and directs along the $x$-axis. The $z$-axis is defined as the rotational axis of the moment, and the magnetic structure is characterized by a magnetic propagation vector $\boldsymbol{Q} = (0, \pi, \pi)$. Considering the hybridization of the singlet and triplet states, local eigenstates at the $i$-th site are represented as follow:

$$\begin{aligned}
|G_i\rangle &= u\,|s\rangle + v\left(\cos\phi_i\,|t_x\rangle + \sin\phi_i\,|t_y\rangle\right), \\
|L_i\rangle &= -v\,|s\rangle + u\left(\cos\phi_i\,|t_x\rangle + \sin\phi_i\,|t_y\rangle\right), \\
|T_{1,i}\rangle &= -\sin\phi_i\,|t_x\rangle + \cos\phi_i\,|t_y\rangle, \\
|T_{2,i}\rangle &= |t_z\rangle,
\end{aligned}$$

where $u$ and $v$ are real coefficients satisfying $u^2 + v^2 = 1$. $|G_i\rangle$ is a eigenstate for the mean-field ground state. $|L_i\rangle$, $|T_{1,i}\rangle$ and $|T_{2,i}\rangle$ are orthogonal to $|G_i\rangle$ and are for excited states. The phase factor $\phi_i$ at the $i$-th site position $\boldsymbol{r}_i$ is written as

$$\phi_i = \boldsymbol{Q}\cdot\boldsymbol{r}_i + \phi_0, \tag{1.69}$$

where $\phi_0$ is constant. From Eq. (1.68), we have

$$|G_i\rangle = \frac{u}{\sqrt{2}}\left(|\uparrow\downarrow\rangle - |\downarrow\uparrow\rangle\right) - \frac{v}{\sqrt{2}}\left(e^{-i\phi_i}|\uparrow\uparrow\rangle - e^{i\phi_i}|\downarrow\downarrow\rangle\right), \tag{1.70}$$

$$|L_i\rangle = \frac{-v}{\sqrt{2}}\left(|\uparrow\downarrow\rangle - |\downarrow\uparrow\rangle\right) - \frac{u}{\sqrt{2}}\left(e^{-i\phi_i}|\uparrow\uparrow\rangle - e^{i\phi_i}|\downarrow\downarrow\rangle\right), \tag{1.71}$$

$$|T_{1,i}\rangle = \frac{i}{\sqrt{2}}\left(e^{-i\phi_i}|\uparrow\uparrow\rangle + e^{i\phi_i}|\downarrow\downarrow\rangle\right), \tag{1.72}$$

$$|T_{2,i}\rangle = \frac{1}{\sqrt{2}}\left(|\uparrow\downarrow\rangle + |\downarrow\uparrow\rangle\right). \tag{1.73}$$

The expectation values of the spin operators at the ground state are expressed as

$$\langle G_i|\, S^x_{1,i}\,|G_i\rangle = \langle G_i|\, S^x_{2,i}\,|G_i\rangle = uv\cos\phi_i, \tag{1.74}$$

$$\langle G_i|\, S^y_{1,i}\,|G_i\rangle = \langle G_i|\, S^y_{2,i}\,|G_i\rangle = uv\sin\phi_i, \tag{1.75}$$

$$\langle G_i|\, S^z_{1,i}\,|G_i\rangle = \langle G_i|\, S^z_{2,i}\,|G_i\rangle = 0, \tag{1.76}$$

where $uv = v\sqrt{1-v^2} \equiv M$ is the magnitude of the local magnetic moment. In the mean-field approximation, the inter-dimer interaction is represented as follow:

$$J_{ij}\,\langle G_i|\,\boldsymbol{S}_i\,|G_i\rangle \cdot \langle G_j|\,\boldsymbol{S}_j\,|G_j\rangle = J_{ij}(uv)^2\cos(\phi_i - \phi_j). \tag{1.77}$$

Furthermore, the expectation value of the intra-dimer interaction at the ground state is expressed as

$$\langle G_i|\, J\boldsymbol{S}_{1,i}\cdot\boldsymbol{S}_{2,i}\,|G_i\rangle = J\left(v^2 - \frac{3}{4}\right). \tag{1.78}$$

From Eqs. (1.77) and (1.78), the mean-field ground state energy per site $E_{\mathrm{MF}}$ is given by

$$\begin{aligned} E_{\mathrm{MF}} &= J\left(v^2 - \frac{3}{4}\right) - (2J_1 + 2J_2 - J_3)(uv)^2 \\ &= (J - J_{\mathrm{eff}})v^2 + J_{\mathrm{eff}}v^4 - \frac{3}{4}J. \end{aligned} \tag{1.79}$$

The mean-field ground state energy is only a function of $v$. The value of $v$ is determined by minimizing $E_{\mathrm{MF}}$ and characterized by the ratio of $J_{\mathrm{eff}}/J$, which corresponds to the dimensionless coupling $g$ in Section 1.4.1. $J_{\mathrm{eff}}/J = 1$ corresponds to the critical point $g_{\mathrm{c}}$. In $J_{\mathrm{eff}}/J < 1$, in which $E_{\mathrm{MF}}$ is a parabolic-like potential as shown in Fig. 1.3(a), $v$ becomes zero, i.e., the ordered moment $M = 0$. The spin system is in the paramagnetic state. In $J_{\mathrm{eff}}/J > 1$, in which $E_{\mathrm{MF}}$ is a Mexican hat-like potential as shown in Fig. 1.3(b), $v$ becomes finite value, i.e., the ordered moment $M \neq 0$. The magnetic ordered state is realized in this case.

In the ordered phase, three excitation modes are expected. Two of them are massless NG-mode originating from transverse fluctuation of the moment and the other is a massive Higgs mode from the longitudinal fluctuation as shown in Fig. 1.3(b).

### $TlCuCl_3$

$TlCuCl_3$ is a well-studied material showing the QPT in the spin dimer system. Since the nearest-neighbor antiferromagnetic interaction is very strong, the $Cu^{2+}$ spins are dimerized. The dimers weakly interact with each other as shown in Fig. 1.5(a). Under zero magnetic field and at ambient pressure, the $Cu^{2+}$ spin dimer realizes a spin singlet ground state [33] with the excitation gap of 0.6 meV [34, 35].

The magnetic ordering in $TlCuCl_3$ was observed under magnetic field [35, 36, 37] and pressure [38, 39, 40, 28]. In addition to that the magnetic field-induced magnetic ordering has

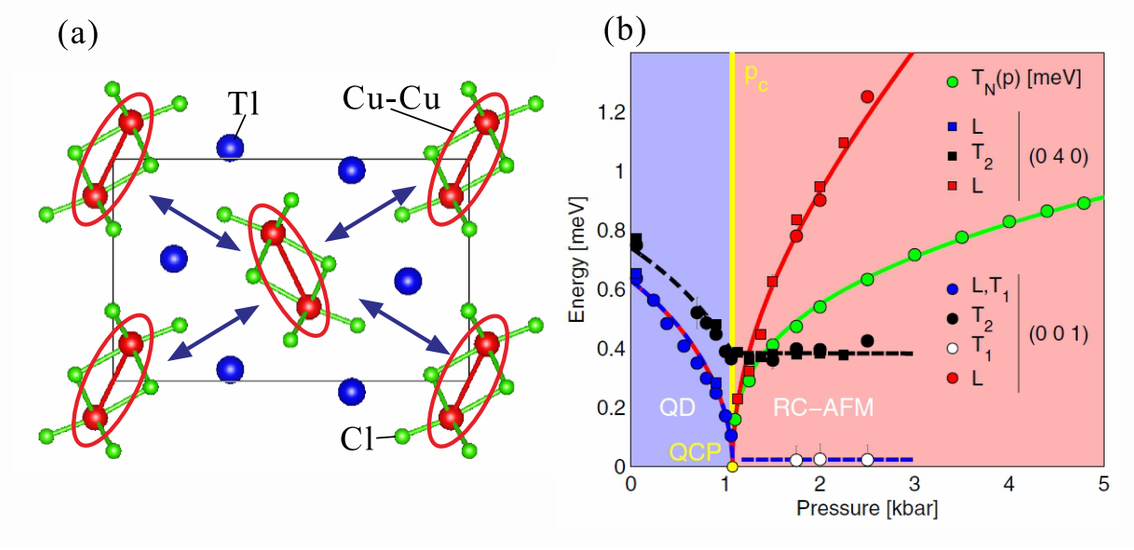


Figure 1.5 (a) Crystal structure of $TlCuCl_3$. (b) Measurements of the excitation energies and transition temperatures $T_N$ [27].

been studied as a good model compound of the magnon Bose-Einstein condensation [41], the inelastic neutron scattering study demonstrated the Higgs mode in the pressure-induced ordered phase [27, 28]. Figure 1.5(b) shows the measurements of the excitation energies under pressures. The magnetic excitations in the quantum disordered phase are softened with the increase of the pressure. The QPT occurs at 1.07 kbar [40]. In ordered phase, the magnetic excitations are split to Nambu-Goldstone (transverse) mode and Higgs (longitudinal) mode, and there are two transverse modes and one longitudinal mode. The experimental works on the magnetic field- and pressure-induced QPTs have triggered many theoretical studies; magnon Bose-Einstein condensation [41, 42, 43], longitudinal magnon [44, 45], and universality in three-dimensional quantum antiferromagnet [46, 47, 48, 49, 50].

### 1.4.5 Spin-1 antiferromagnet with strong easy-plane anisotropy

In this thesis, we focus on the spin $S = 1$ antiferromagnet with a strong easy-plane anisotropy. Its QPT is explained by the mean-field theory in the same procedure as the spin dimer system, which is described in detail in Ref. [51]. The Hamiltonian is given by

$$\mathcal{H} = \sum_{\langle ij \rangle} J_{ij} \boldsymbol{S}_i \cdot \boldsymbol{S}_j + \sum_i D(S_i^z)^2, \tag{1.80}$$

where $J_{ij}$ term represents an interaction between the spins and $D$ ($> 0$) term represents the easy-plane anisotropy. $S_i$ is the spin operator having spin-1.

#### Square lattice model

Firstly, let us denote a stacked square lattice model with the antiferromagnetic interactions $J_1$ and $J_2$ as shown in Fig. 1.6(a). When the easy-plane anisotropy $D$ is much stronger than the interaction $J_{ij}$, the singlet state $S^z = 0$ is the ground state and the doublet state $S^z = \pm 1$ is the excited state as shown in Fig. 1.6(b). With the increase of the spin interaction energy, the singlet and doublet sates are hybridized. This brings about the magnetic long-range order. It is assumed that the a collinear magnetic structure is realized and the direction of the magnetic moment

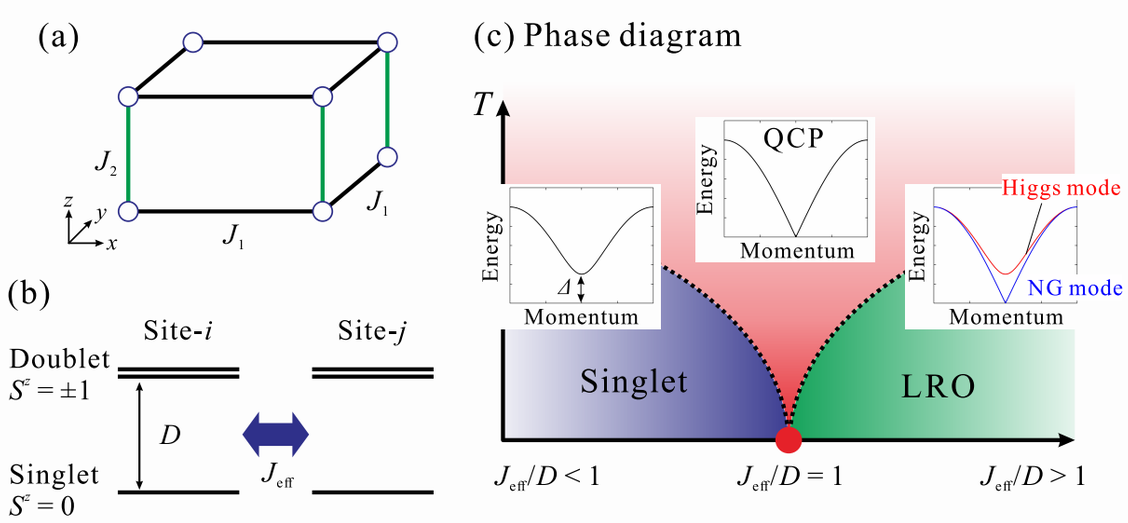


Figure 1.6 (a) Interaction paths of the square-lattice antiferromagnet. $J_1$ and $J_2$ are in-plane and inter-plane interactions, respectively. (b) Schematic diagram of $S = 1$ antiferromagnet with strong easy-plane anisotropy. (c) Schematic diagram of the relationship of the normal excitation mode and the QPT.

characterized by a magnetic propagation vector $\boldsymbol{Q} = (\pi, \pi, \pi)$. Considering the hybridization of the singlet and doublet state, local eigenstates at the $i$-th site are represented as follow:

$$|G_i\rangle = u\,|0_i\rangle + \frac{v}{\sqrt{2}}\left(e^{-i\phi_i}\,|1_i\rangle + e^{i\phi_i}\,|-1_i\rangle\right), \tag{1.81}$$

$$|L_i\rangle = -v\,|0_i\rangle + \frac{u}{\sqrt{2}}\left(e^{-i\phi_i}\,|1_i\rangle + e^{i\phi_i}\,|-1_i\rangle\right), \tag{1.82}$$

$$|T_i\rangle = \frac{-1}{\sqrt{2}}\left(e^{-i\phi_i}\,|1_i\rangle - e^{i\phi_i}\,|-1_i\rangle\right), \tag{1.83}$$

where $|m_i\rangle$ is the $S^z = m$ ($m = 1$, 0, -1) state at the $i$-th site. $u$ and $v$ are real coefficients satisfying $u^2 + v^2 = 1$. $|G_i\rangle$ is a eigenstate for the mean-field ground state. $|L_i\rangle$ and $|T_i\rangle$ are orthogonal to $|G_i\rangle$ and are for excited states. The phase factor $\phi_i$ at the $i$-th site position $\boldsymbol{r}_i$ is given by $\phi_i = \boldsymbol{Q} \cdot \boldsymbol{r}_i + \phi_0$.

At the ground state, the expectation values of the spin operators are expressed as

$$\langle G_i|\, S_i^x\, |G_i\rangle = 2uv\cos\phi_i, \tag{1.84}$$

$$\langle G_i|\, S_i^y\, |G_i\rangle = 2uv\sin\phi_i, \tag{1.85}$$

$$\langle G_i|\, S_i^z\, |G_i\rangle = 0, \tag{1.86}$$

where $2uv = 2v\sqrt{1-v^2} \equiv M$ is the magnitude of the local magnetic moment. In the mean-field approximation, the inter-spin interaction $J_{ij}$ is represented as

$$J_{ij}\,\langle G_i|\,\boldsymbol{S}_i\,|G_i\rangle \cdot \langle G_j|\,\boldsymbol{S}_j\,|G_j\rangle = J_{ij}(2uv)^2\cos(\phi_i - \phi_j). \tag{1.87}$$

In addition, the expectation value of the easy-plane anisotropy at the ground state is expressed as

$$\langle G_i|\, D(S_i^z)^2\, |G_i\rangle = Dv^2. \tag{1.88}$$

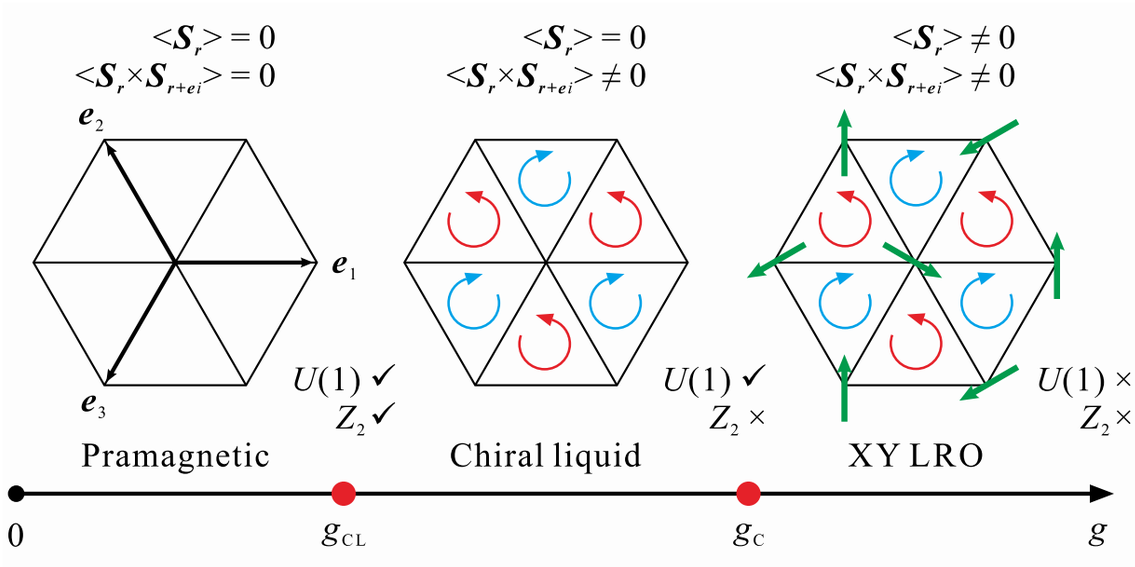


Figure 1.7 A schematic diagram of the paramagnetic, chiral liquid, and XY long-range order (LRO) phases as a function of the tuning parameter $g \sim J/D$ [52].

From Eqs. (1.87) and (1.88), the mean-field ground state energy per site $E_{\rm MF}$ is given by

$$\begin{aligned} E_{\rm MF} &= Dv^2 + (-2J_1 - J_2)(2uv)^2 \\ &= (D - J_{\rm eff})v^2 + J_{\rm eff}v^4, \end{aligned} \tag{1.89}$$

where $J_{\rm eff} = -8J_1 - 4J_2$.

The mean-field ground state energy is a function of $v$, and value of $v$ which is determined by minimizing $E_{\rm MF}$ is characterized by $J_{\rm eff}/D$. As in the case of the spin dimer system, the paramagnetic and ordered states are distinguished by $J_{\rm eff}/D < 1$ and $J_{\rm eff}/D > 1$, respectively. The normal excitation modes in the QPT were exhibited in Ref. [51]. Figure 1.6(c) shows the normal modes in each phase. In the singlet phase, there is a twofold degenerated gapped excitation. The excitation is softened toward the critical point, its gap closes at $J_{\rm eff}/D = 1$. In the ordered phase, the degenerated excitation is split into gapless and gapped excitations. The gapless and gapped modes correspond to Nambu-Goldstone and Higgs modes, respectively.

### Triangular lattice model

Next we describe a stacked triangular lattice model with a ferromagnetic inter-layer interaction $J_1$ and an antiferromagnetic in-plane interaction $J_2$. The magnetic structure is characterized by a magnetic propagation vector $\boldsymbol{Q} = (2\pi/3, 2\pi/3, 0)$. The $J_{\rm eff}$ should be modified as follow:

$$\begin{aligned} J_{\rm eff} &= -2\left(2J_1 + 6J_2\cos\frac{2\pi}{3}\right) \\ &= 2(-2J_1 + 3J_2). \end{aligned} \tag{1.90}$$

Thus, the mean-field ground state energy per site is obtained as

$$\begin{aligned} E_{\rm MF} &= Dv^2 - J_{\rm eff}(uv)^2 \\ &= (D - J_{\rm eff})v^2 + J_{\rm eff}v^4. \end{aligned} \tag{1.91}$$

In this system, the QPT occurs when $D = 2(-2J_1 + 3J_2)$.

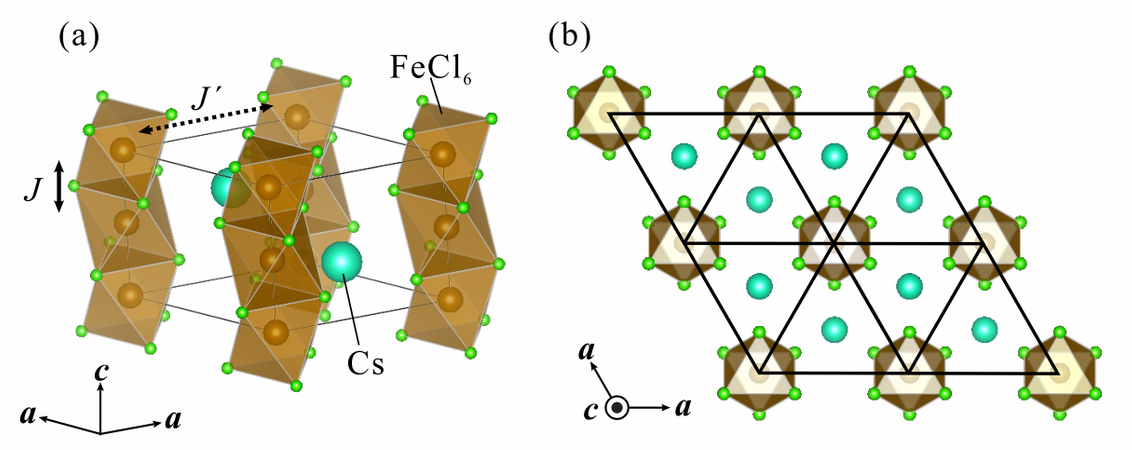


Figure 1.8 Crystal structures of $CsFeCl_3$. Double-headed solid and dashed arrows indicate the intrachain and interchain interaction $J$ and $J'$, respectively.

An interesting point in this system is that the system has a geometrical frustration due to the triangular lattice. Recent theoretical study found a remarkable QPT in spin-1 $XXZ$ Heisenberg antiferromagnet with a large easy-plane anisotropy on a triangular lattice [52]. In this study, an existence of the transition to a chiral spin liquid was found in addition to the ordinary magnetic dipole ordering as mentioned above. Figure 1.7 shows the phase diagram proposed in Ref. [52]. In the magnetic ordered phase, a 120° structure is realized and the system breaks continuous $U(1)$ symmetry and discrete $Z_2$ symmetry. While the $U(1)$ symmetry means a long-range magnetic order, the $Z_2$ symmetry represents chiral symmetry. They found that a phase where only $Z_2$ chiral symmetry is broken does exist between paramagnetic and magnetic ordered phases. This non-trivial phase is called the chiral liquid phase. Even though they focused on the appearance of the chiral liquid phase, they have not studied the spin spectrum yet. The interest is thus in the investigation of the magnetic excitation in the ordered phase. A novel magic state is expected in the vicinity of the QCP containing the geometrical frustration.

### $CsFeCl_3$

$CsFeCl_3$ is one of halide $ABX_3$ antiferromagnets ($A^+$ = alkali metal ion, $B^{2+}$ = transition metal ion, and $X^-$ = halogen ion). The $ABX_3$ antiferromagnets is a rich field of studies on magnetism. For examples, a dimerized antiferromagnet $KCuCl_3$ [53], a Haldane gap system $CsNiCl_3$ [54], a triangular lattice antiferromagnet $CsCuCl_3$ [55], 1D Ising-like antiferromagnet $CsCoCl_3$ [56, 57], and a $XY$-like antiferromagnet $RbFeCl_3$ [58].

The crystal structure of $CsFeCl_3$ is a hexagonal with $P6_3/mmc$ [59]. Magnetic $Fe^{2+}$ ions are surrounded octahedrally by six $Cl^-$ ions, and the $FeCl_6$ octahedra form a 1D ferromagnetic chain along the crystallographic $c$-axis [60] as shown in Fig. 1.8(a). The chains form a triangular lattice in the $ab$-plane as shown in Fig. 1.8(b).

The magnetic state of the $Fe^{2+}$ ion at the low temperature is shown in Fig. 1.9. The lowest orbital state of the $Fe^{2+}$ ion in the cubic environment is the triplet $T_{2g}$ [61]. This triplet orbital couples with the spin $S = 2$ owing to the spin-orbit interaction. The lowest state becomes a triplet expressed by a pseudo-spin $s = 1$. Moreover, the pseudo-spin $s = 1$ is split into $s^z = 0$ singlet ground state and $s^z = \pm 1$ doublet state because the trigonally elongated octahedra of $FeCl_6$ induces an easy-plane type single-ion anisotropy $D(s^z)^2$. The system is thus regarded as $s = 1$ $XY$-like spin system. The low energy magnetic properties of $CsFeCl_3$ can be described by

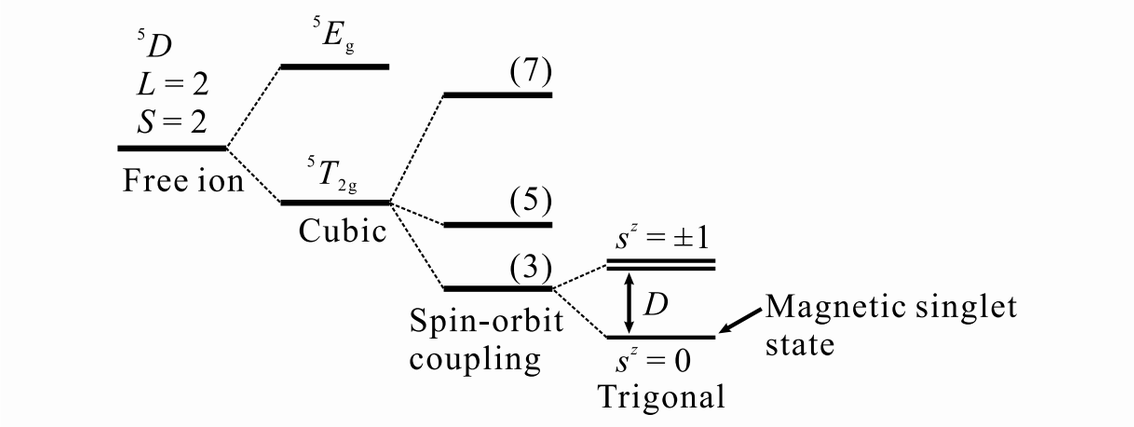


Figure 1.9 Electronic structure of the $Fe^{2+}$ ion.

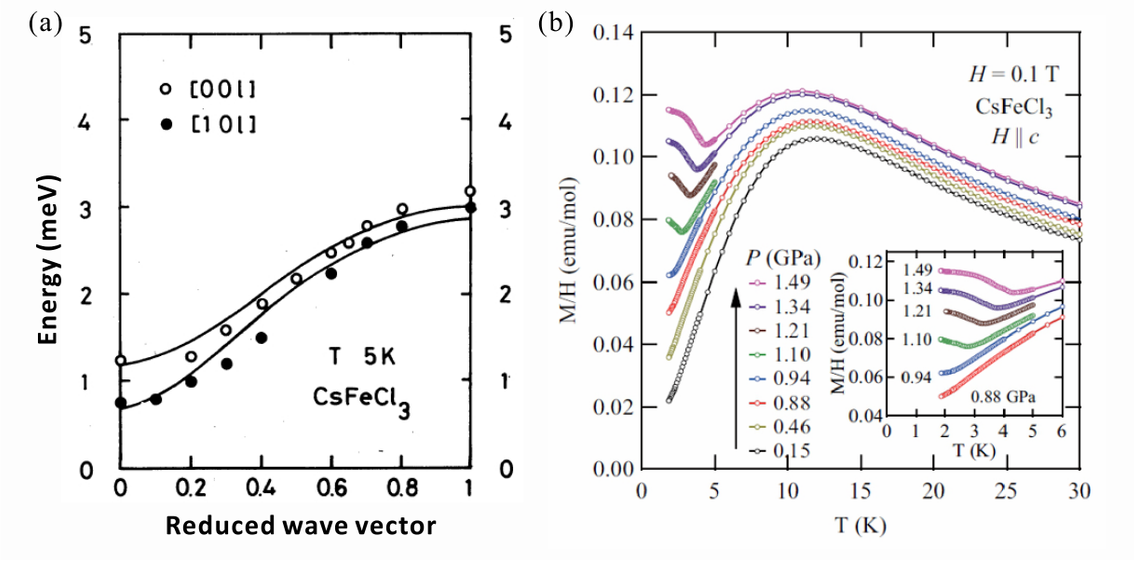


Figure 1.10 (a) Magnetic excitation in $CsFeCl_3$ under ambient pressure obtained by inelastic neutron scattering experiment [58]. (b) Pressure evolution of magnetic susceptibility [62].

the Hamiltonian [61]

$$\mathcal{H} = \sum_{\langle ij \rangle}^{\text{chain}} \left[ J_\perp (s_i^x s_j^x + s_i^y s_j^y) + J_\parallel s_i^z s_j^z \right] + \sum_{\langle ij \rangle}^{\text{plane}} \left[ J'_\perp (s_i^x s_j^x + s_i^y s_j^y) + J'_\parallel s_i^z s_j^z \right] + \sum_i D (s_i^z)^2, \quad (1.92)$$

where $J_\perp$, $J_\parallel$ are the intra-chain interactions and $J'_\perp$, $J'_\parallel$ are the in-plane interaction as shown in Fig. 1.8(a).

Inelastic neutron scattering experiment has revealed magnetic excitations of $CsFeCl_3$ at ambient pressure and at zero magnetic field by H. Yoshizawa [58]. The gapped dispersion was observed as shown in Fig. 1.10(a), and it evidenced that the ground state was the $s^z = 0$ singlet state. From the calculation of the magnetic dispersion, it was found that the spin system was ferromagnetic chains that were weakly coupled by antiferromagnetic interchain interaction. Since the $Fe^{2+}$ ions form the triangular lattice in the *ab*-plane, the antiferromagnetic interchain interaction causes the geometrical frustration.

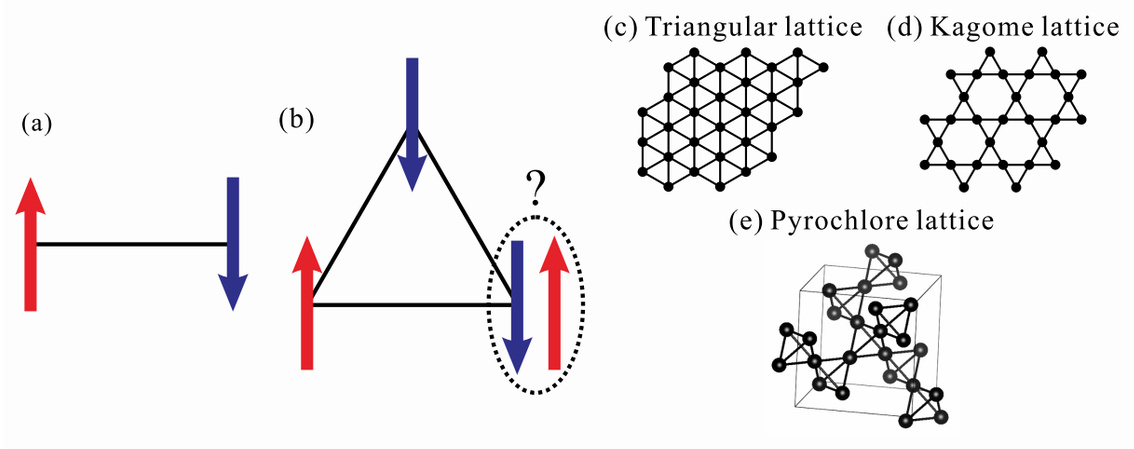


Figure 1.11 (a) A pair of Ising spins with antiferromagnetic coupling. (b) Ising spins with antiferromagnetic couplings on a triangle. Schematic diagrams of (c) triangular lattice, (d) Kagome lattice, and (f) pyrochlore lattice.

$CsFeCl_3$ exhibits an antiferromagnetic order under a magnetic field along the $c$-axis [63, 64, 65, 66, 67]. The neutron diffraction experiment under the field has identified that applying magnetic field induced an incommensurate state at $B \approx 5$ T, and a commensurate phase occurred above 10 T, in which the magnetic structure was a 120° structure with the magnetic propagation vector of $\boldsymbol{q} = (1/3, 1/3, 0)$ [67]. It was deduced that the temperature and magnetic field dependence of the order parameter corresponded to magnon BEC theory.

Very recently, a magnetic susceptibility measurement under pressures was performed by N. Kurita and H. Tanaka [62]. Figure 1.10(b) shows the pressure evolution of the magnetic susceptibility. The magnetic susceptibilities above $P = 0.94$ GPa showed upturn anomaly at low temperature. This indicates a magnetic long range order occurs above 0.94 GPa because this anomaly is similar to the susceptibility at the ambient pressure in the magnetic-field induced magnetic long range order. It is indicated that applying pressure effectively enhances the spin interaction, and suppresses the anisotropy energy. $CsFeCl_3$ is, thus, a singlet ground state magnet exhibiting pressure-induced QPT.

$CsFeCl_3$ is a good model compound to investigate the quantum critical phenomena on the geometrically frustrated lattice. As well as the excitations in pressure-induced ordered state in a spin-dimer compound $TlCuCl_3$ [28, 40], unconventional excitation including NG and Higgs modes are expected. In addition, $CsFeCl_3$ is a candidate for the experimental realization of the chiral liquid proposed in Ref. [52].

## 1.5 Geometrically frustrated spin systems

A geometrical frustration in spin system is generated by the competition of the magnetic interaction due to the lattice geometry. A typical example of the the geometrical frustration is a triangular lattice with antiferromagnetic Ising spins. When a pair of the Ising spins antiferromagnetically interacts each other, an antiparallel spin configuration is the ground state as shown in Fig. 1.11(a). In case of that the Ising spins are antiferromagnetically coupled on a triangle, it is impossible to simultaneously minimize the energies of all bonds in Fig. 1.11(b). This situation is called geometrical frustration. It prevents the realization of a trivial spin configuration, and the spin state is strongly fluctuated. The geometrical frustration appears not only in the triangular lattice in Fig. 1.11(c) but also in various lattices constructed by the triangle motif such as Kagome and pyrochlore lattices in Figs. 1.11(d) and 1.11(e).

Since the first study on the triangular lattice antiferromagnet having Ising spin was reported by G. H. Wannier in 1950 [68], many studies on the geometrically frustrated magnets have been extensively produced in both of theoretical and experimental aspects [69, 70]. Owing to remaining the macroscopic degeneracy at low temperature by the frustration, diverse and exotic spin states are expected [71]. The most remarkable phenomenon is the spin liquid state. Broadly speaking, the spin liquid is a disordered spin state in spite of that the spins are strongly coupled in the microscopic view. The spin liquid has been attracted in condensed matter physics because unforeseen properties such as fractional spin excitation [69] are expected.

In real geometrically frustrated magnets, most of cases exhibit magnetic ordering or freezing of spin system for a ground state, which is caused by the requirement of the third law of thermodynamics. When the main interaction cannot lift the degeneracy at low temperature, small perturbations can play a key role to determine the spin state. These perturbations include further neighbor interaction, single-ion anisotropy, Dzyaloshinskii-Moriya interaction, magnetic dipolar interaction, magnetoelectric coupling, site dilution and exchange randomness. The geometrical frustration thus brings about downshifting of the energy scale, and makes an effect of usually ignored perturbations stand out. It is very important to study a contribution of the small perturbations in the geometrically frustrated spin systems.

Another key feature in frustrated spin system is a non-collinear spin structure. For example, let us denote the ground state of three spins configuration in the case of $XY$ spins on a triangle. The energy of the three spins antiferromagnetically interacting each other is written as

$$E = J(\boldsymbol{S}_1 \cdot \boldsymbol{S}_2 + \boldsymbol{S}_2 \cdot \boldsymbol{S}_3 + \boldsymbol{S}_3 \cdot \boldsymbol{S}_1). \tag{1.93}$$

This energy $E$ can be represented as

$$E = -\frac{3}{2}JS^2 + \frac{J}{2}\left(\boldsymbol{S}_1 + \boldsymbol{S}_2 + \boldsymbol{S}_3\right)^2. \tag{1.94}$$

From this equation, $\boldsymbol{S}_1 + \boldsymbol{S}_2 + \boldsymbol{S}_3 = 0$ gives the minimum energy. This means that the three spins form a 120° structure when the magnitudes of the spin moments are conserved. Consequently, the noncollinear spin structure is realized. The non-collinear spin structure was discovered in 1959 independently by A. Yoshimori [72], J. Villain [73], and T. A. Kaplan [74]. This non-collinearity due to the geometrical frustration can make it easy to change the local crystal structure because the bond energy between the spins is not minimized. This effect is closely related to a magnetoelectric effect in the multiferroic materials, which have been greatly paid attention for the application to the innovative device [75]. Therefore, the geometrically frustrated spin systems have been remarked from the view of the fundamental and applied studies.

In this thesis, we focus on the Kagome antiferromagnet in the geometrically frustrated spin systems. Hereafter, studies on the Kagome antiferromagnet is briefly introduced. Then the ground state and dynamics on a classical Kagome antiferromagnet is described, and the Kagome-Triangular antiferromagnet $NaBa_2Mn_3F_{11}$ is introduced.

### 1.5.1 Kagome antiferromagnet

The Kagome lattice is a 2D lattice sharing corners of the triangles as shown in Fig. 1.11(d). First study was an Ising model on the Kagome lattice by K. Kano [76], who exhibited that the Kagome antiferromagnet was disordered at all temperature and possessed a finite entropy even at zero temperature. After P. W. Anderson in 1973 proposed a resonating valence bond ground state (RVB) in the triangular antiferromagnet as a spin liquid state [77], the Kagome antiferromagnets have been the forefront field to develop the new concept and discover the new materials which display exotic spin liquid states.

Figure 1.12 shows the energy spectrum calculated by the exact diagonalizations in a $S = 1/2$ Heisenberg Kagome antiferromagnet [78]. The energy spectra are plotted as a function of the magnitude of the spin $S$. The low-lying spectrum structure in the Kagome antiferromagnet is

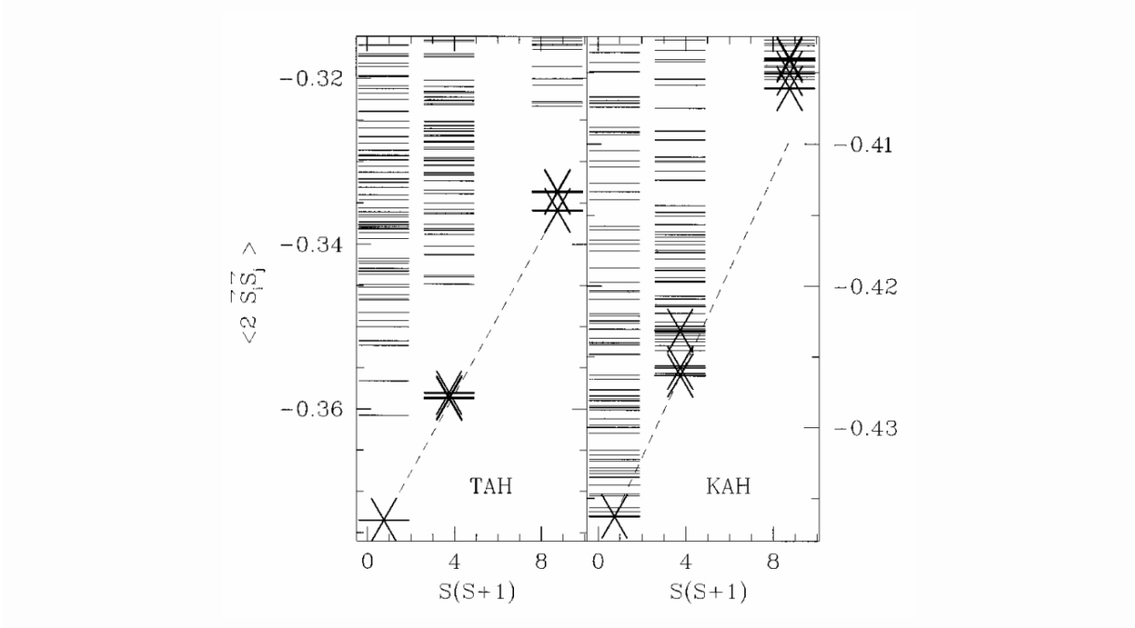


Figure 1.12 Energy spectra of the $N = 27$ sample calculated by exact diagonalizations technique in Heisenberg triangular antiferromagnet and Heisenberg Kagome antiferromagnet, labeled TAH and KAH, from Ref. [78].

different from that in the triangular antiferromagnet exhibiting the magnetic ordering. This indicates that the $S = 1/2$ Heisenberg antiferromagnet on the Kagome lattice realized a non-magnetic singlet ground state, i.e., quantum spin liquid state. It has been an open question what type of the spin liquid state is realized in the Kagome antiferromagnet up to now.

For the experimental studies, there has been many reports on the Kagome antiferromagnets so far. Herbertsmithite $ZnCu_3(OH)_6Cl_2$ has been studied as the most promising candidate for an ideal quantum Kagome antiferromagnet. It exhibited no magnetic long-range order down to 35 mK [79] and fractionalized excitation was observed [80]. In Volborthite $Cu_3V_2O_7(OH)_2 \cdot 2H_2O$, the one-third magnetization plateau [81] was observed and they discussed the existence of the condensation of the magnon bound state [82]. Kapellasite $Cu_3Zn(OH)_6Cl_2$ is one of the quantum spin liquid compound which has non-trivial cuboc spin correlation [83]. Other studies on the quantum Kagome antiferromagnet are reviewed in Ref. [84]. The Kagome antiferromagnet has been therefore an intriguing field to explore the novel spin state.

### 1.5.2 Ground state of Kagome antiferromagnet

While the quantum Kagome antiferromagnet has been studied as a field of the quantum spin liquid state, a classical Kagome antiferromagnet also have interesting characters. In the classical Heisenberg Kagome antiferromagnet, the ground state is infinitely degenerated. At zero temperature order-by-disorder mechanism induces a magnetic long-range order of the 120° structures with the enlarged $\sqrt{3}\times\sqrt{3}$ unit cell [85] in Fig. 1.13(a). Various perturbations can also lift the degeneracy of the ground states. In case of the Dzyaloshinskii-Moriya (DM) interaction $\boldsymbol{D}_{ij} \cdot (\boldsymbol{S}_i \times \boldsymbol{S}_j)$ in which the DM vector $\boldsymbol{D}_{ij}$ is on a mirror plane between the lattice points, 120° structures with $\boldsymbol{k} = 0$ are selected [86]. The 120° structures exhibit positive vector chirality in Fig. 1.13(b) and negative vector chirality in Fig. 1.13(c). In this thesis, the former and the latter structures are named for DM(+) and DM(−)-type 120° structures, respectively. The vector chirality is determined by the out-of-plane component of the DM vector $D_z$ as indicated

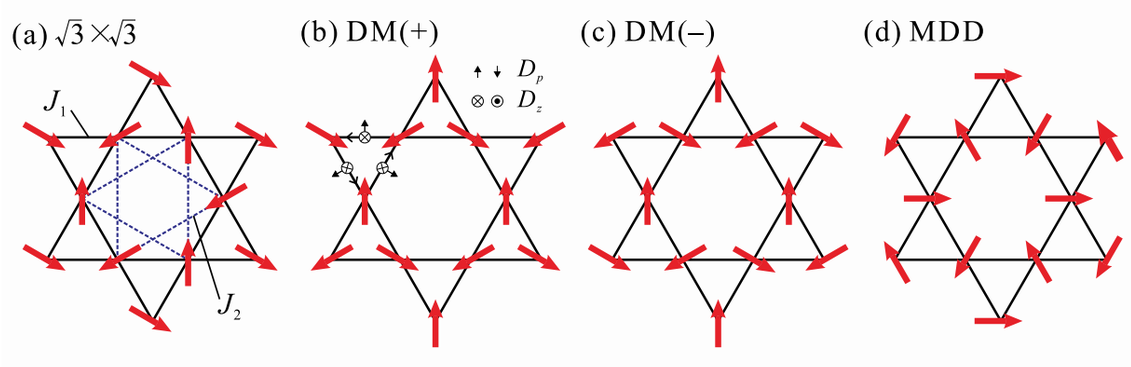


Figure 1.13 120° structures in Kagome lattice. The red arrows represented directions of the spins. (a) 120° structure with the enlarged unit cell by $\sqrt{3} \times \sqrt{3}$. (b) DM(+), (c) DM(−), and (d) MDD-type 120° structure with the magnetic propagation vector of $\boldsymbol{k} = 0$.

in Fig 1.13(b). In the DM(+)-type 120° structure, the easy-axis anisotropy is induced by its in-plane component of the DM vector $D_p$ as indicated in Fig 1.13(b). The MDD interaction selects the 120° structure with the $\boldsymbol{k} = 0$ exhibiting *tail-chase* geometry as shown in Fig. 1.13(d) [87]. It has positive vector chirality, and its direction of the easy-axis anisotropy is rotated by 90° from that of the DM(+)-type structure. It is named for MDD-type 120° structure. The second-neighbor interaction selects the 120° structure with $\boldsymbol{k} = 0$ for the antiferromagnetic case and that with $\sqrt{3} \times \sqrt{3}$ unit cell for the ferromagnetic case [88].

The magnetic structures of the Kagome antiferromagnet have been intensively investigated by neutron diffraction experiment on many compounds. The DM(+)-type structure has been reported in many cases; series of iron jarosite $A\mathrm{Fe_3(SO_4)_2(OH)_6}$ ($A$ = K, Na, Ag, Rb, $\mathrm{NH_4}$) [89, 90, 91, 92], chromium jarosite $\mathrm{KCr_3(SO_4)_2(OH)_6}$ [93], and tripod-Kagome compound $\mathrm{Nd_3Sb_3Mg_2O_{14}}$ [94]. They may be caused by the coincidence between the direction of spins and the magnetic easy-axis allowed by the crystallographic symmetry. The DM(−)-type 120° structure was observed in a couple semimetals $\mathrm{Mn_3Sn}$ and $\mathrm{Mn_3Ge}$, which demonstrated a large anomalous Hall effect [95]. The $\sqrt{3} \times \sqrt{3}$ structure was found in the high pressure phase in herbersmithite $\mathrm{ZnCu_3(OH)_6Cl_2}$ [96]. The 120° structure with the tail-chase geometry was observed in quiternary oxalate compounds with $\mathrm{Fe^{2+}}$ ion so far [97, 98]. However, the magnetic structure was attributed to a strong single-ion anisotropy not the MDD interaction. To our knowledge thus the tail-chase structure originating from the MDD interaction has not been observed by neutron diffraction yet.

### 1.5.3 Magnetic excitation of classical Kagome antiferromagnet

The classical Kagome antiferromagnet generates a macroscopic ground state degeneracy of the 120°. This macroscopic degeneracy of the 120° structure enables continuous arrangement of spins, and it forms excitation modes of zero energy [99], which is called zero-energy mode. Figure 1.14(a) shows schematic diagrams of the zero-energy mode. The two spins in a triangle rotate about the direction of rest of the spin, and they keep the 120° configuration. This rotation of the spins thus has no energy cost. In this mode, the spin wave mode is localized, i.e., the flat spin wave band is generated. The zero-energy mode in the frustrated spin systems prevents magnetic long-range order, even at $T = 0$.

The flat band has been recently attracted in other field not only in the geometrically frustrated magnet. In fermionic systems, the flat band provides a variety of unconventional topological orders [102, 103, 104]. Especially, the theoretical models for the fractional quantum Hall effect has been intensively studied based on the flat topological band in Refs. [105, 106, 107], which is

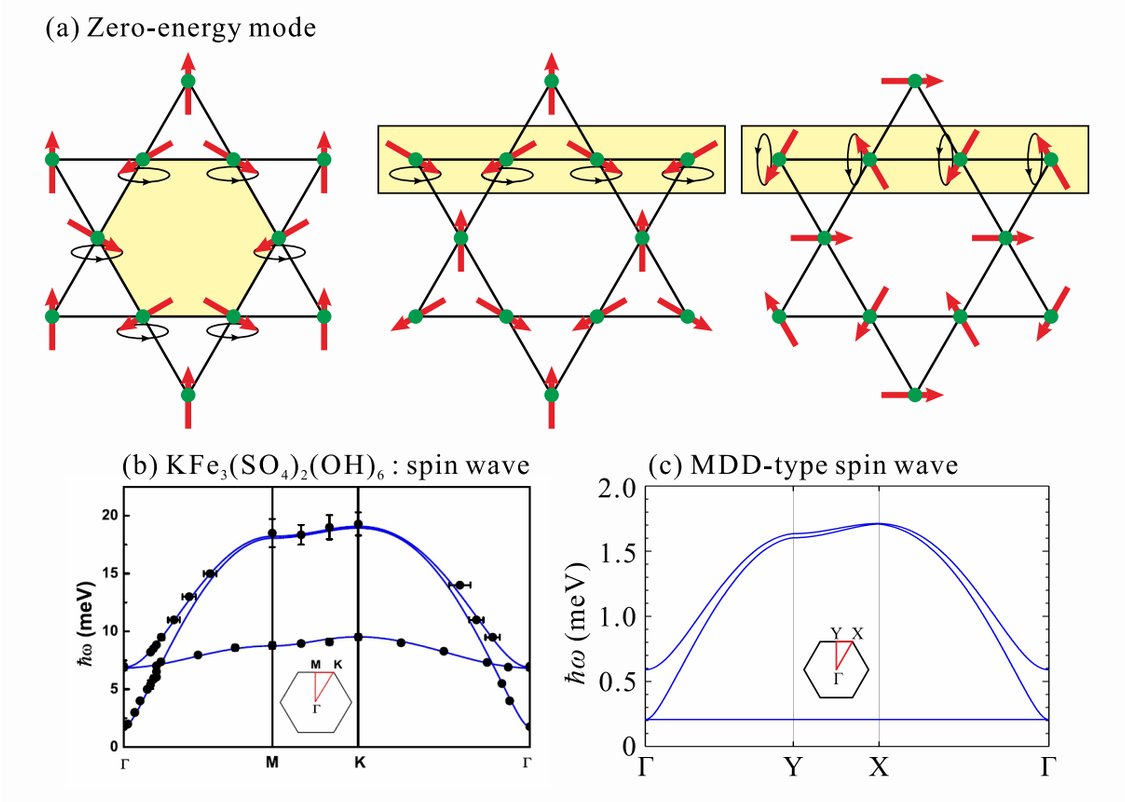


Figure 1.14 (a) Schematic of zero-energy mode in 120° structures. Red arrows indicate spins. (b) Spin wave dispersion in $KFe_3(SO_4)_2(OH)_6$ [100]. (c) Spin wave dispersion in a Kagome antiferromagnet with MDD interaction [101].

reviewed in Ref. [102]. Not limited to the fermionic flat bands, ones in bosonic systems exhibit unusual phenomena. For example, the Kagome ferromagnet Cu[1,3-benzenedicarboxylate] exhibited a flat band of spin wave excitation [108], which was the first material realizing an effectively 2D topological magnon insulator [109]. This material has been expected to exhibit a magnon Hall effect [110, 111] and protected chiral edge modes [112]. Furthermore, it is expected that the flat band can be responsible for unusual thermodynamics and transport properties even when it is not a host for the exotic topological order. Therefore, investigation of the flat zero-energy mode is an intriguing topic in condensed matter physics.

In real compounds for the Kagome antiferromagnet model, the zero-energy mode emerges in an excited state lifted by additional terms including magnetic anisotropy and/or DM interaction. The zero-energy mode in the Kagome antiferromagnet was observed in a potassium iron jarosite $KFe_3(SO_4)_2(OH)_6$ by inelastic neutron scattering [100]. Figure 1.14(b) shows the spin wave dispersion in $KFe_3(SO_4)_2(OH)_6$. They revealed through linear spin wave calculation that the flat dispersion at 7 meV corresponds to the zero-energy mode which was lifted to the excited state by DM interaction. Because of the small next neighbor exchange interaction, the flat mode becomes a little dispersive.

Recent theoretical study reported that the Kagome antiferromagnet having the MDD interaction exhibited the zero-energy mode lifted to the excited state by the MDD interaction [101]. Figure 1.14(c) show a spin wave dispersion calculated by the linear spin wave theory in a model having the nearest-neighbor exchange interaction and nearest-neighbor MDD interaction. The flat zero-energy mode appears at the first excited state, which is different from the case of the DM(+)-type 120° structure in $KFe_3(SO_4)_2(OH)_6$. In addition, it was showed that the zero-energy

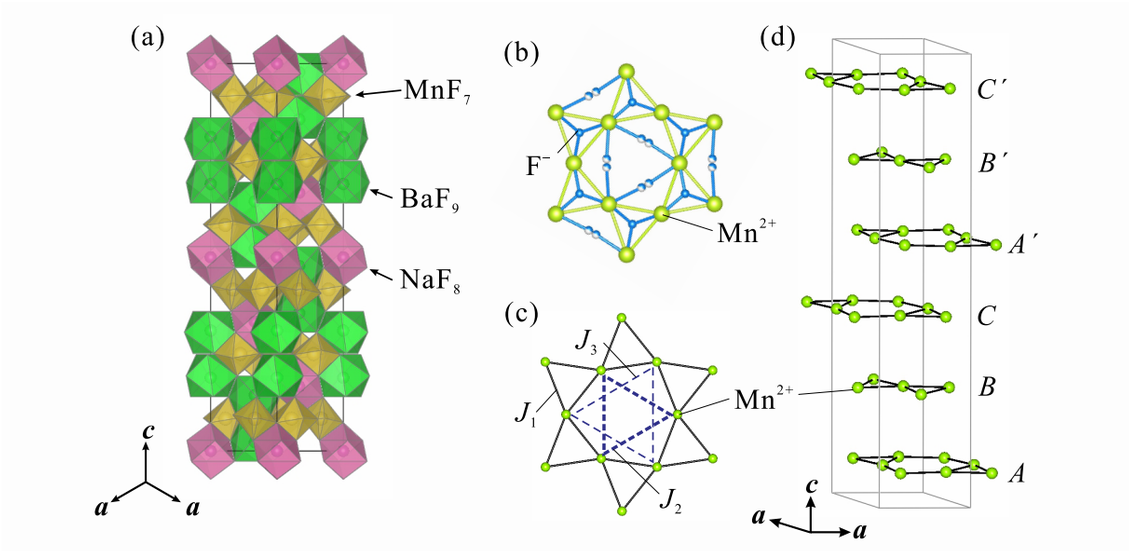


Figure 1.15 (a) Crystal structure of $NaBa_2Mn_3F_{11}$ with the space group $R\bar{3}c$. (b) $Mn^{2+}$ and $F^-$ ions in a Kagome layer. (c) Interaction paths in the Kagome layer. Solid lines are the nearest neighbor interaction $J_1$. Thick and thin dashed lines are the second $J_2$ and third $J_3$ neighbor interaction, respectively. (d) Linear perspective view of the Kagome layers.

mode is persistent in long-range MDD interactions [101]. To our knowledge, the zero-energy mode in Kagome antiferromagnet was reported only in $KFe_3(SO_4)_2(OH)_6$ [100]. In particular, there is no report of the zero-energy mode in the Kagome antiferromagnet with MDD interaction. Further study on the zero-energy mode in different material is important.

### 1.5.4 Kagome-Triangular antiferromagnet $NaBa_2Mn_3F_{11}$

$NaBa_2Mn_3F_{11}$ is a model compound for the classical Kagome antiferromagnet [113]. Figure 1.15(a) shows the crystal structure of $NaBa_2Mn_3F_{11}$ with the hexagonal symmetry and the space group $R\bar{3}c$. Magnetic $Mn^{2+}$ ions carry spin $S = 5/2$, and a Kagome lattice is formed by $MnF_7$ pentagonal bipyramids in the crystallographic $ab$-plane as shown in Figs. 1.15(b) and 1.15(c). The exchange path of the nearest neighbor interaction $J_1$ indicated by the solid line in Fig. 1.15(c) is Mn-F-Mn. The Kagome lattice is seemingly distorted because the interior angles of the hexagon in the Kagome lattice are shifted from 120°. However, the length of the sides and the angles of the Mn-F-Mn path are the same, which means that the magnitudes of the nearest neighbor interactions are the same. Hence, when we consider only the nearest neighbor interaction, the spin system is regarded as a regular Kagome lattice. The six Kagome layers are stacked in the unit cell as shown in Fig. 1.15(d). The $A$, $B$, and $C$ layers are related to the $A'$, $B'$, and $C'$ layers by the $c$-glide symmetry operation.

The exchange pathways of the second $J_2$ and third $J_3$ neighbor interactions are unusual. While the path of the $J_2$ indicated by the thick dashed line in Fig. 1.15(c) is Mn-F-Mn, that of the $J_3$ indicated by the thin dashed line is Mn-F-F-Mn. Thus, the $J_3$ is negligible compared with the $J_2$. The $J_1$ and $J_2$ network exhibits a unique lattice as shown in Fig. 1.16. The lattice becomes a regular Kagome lattice when the $J_2$ is zero. On the other hand, the lattice becomes an equivalent with a triangular lattice when the $J_2$ equals the $J_1$. This means that the $J_2/J_1$ is a parameter connecting Kagome and triangular lattices. Since the Kagome lattice in $NaBa_2Mn_3F_{11}$ is an intermediate lattice between the Kagome and triangular lattices, the lattice is called *Kagome-Triangular* lattice [114].

The heat capacity and magnetic susceptibility measurements have exhibited that an antifer-

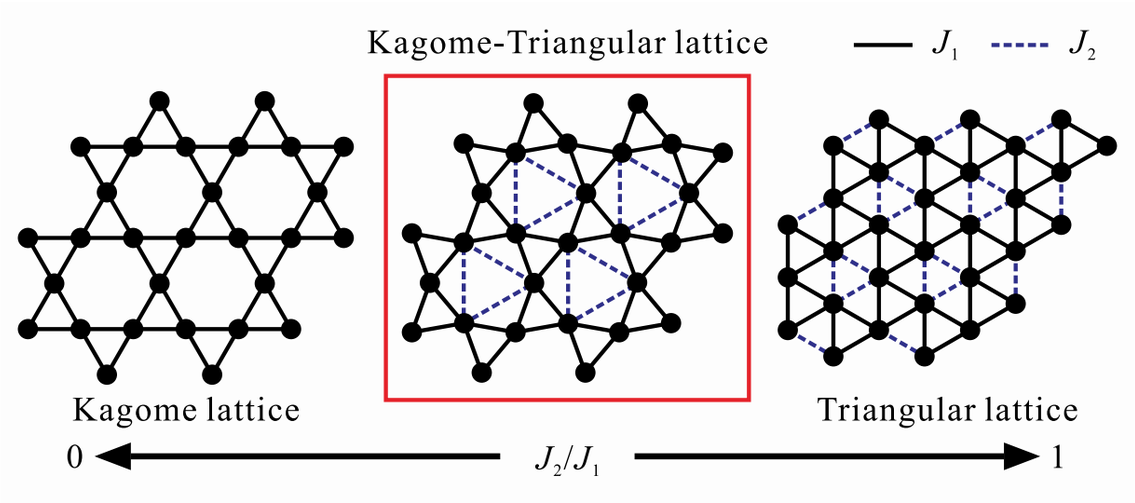


Figure 1.16 Schematic diagram of Kagome, Kagome-Triangular, and Triangular lattices.

romagnetic transition occurred at $T_N = 2$ K [114], and the Curie-Weiss temperature $\theta_{CW}$ was estimated to be $-32$ K. The frustration factor is $f = |\theta_{CW}|/T_N = 16$, which indicates an existence of the strong frustration. The Curie-Weiss temperature was smaller than those of most Kagome lattice antiferromagnets [89, 90, 91, 92, 93, 94, 96]. Furthermore, bond angles of the nearest neighbor exchange pathways are close to 90° rather than 180° as shown in Fig. 1.15(b). This suggests that the $J_1$ is weak antiferromagnetic or ferromagnetic based on the Goodenough-Kanamori rules [115, 116]. The exchange interactions in $NaBa_2Mn_3F_{11}$ are thus relatively small, and the MDD interaction may be important compared with other perturbations such as the second-neighbor exchange interaction and DM interaction. $NaBa_2Mn_3F_{11}$ is a candidate compound realizing a tail-chase geometry MDD-type 120° structure and showing the zero-energy mode lifted by the MDD interaction.

## 1.6 Work presented in this thesis

Spin systems with the quantum fluctuation and geometrical frustration have been good playgrounds to explore novel phenomena. Investigating the static and dynamic spin states is of great importance to elucidate the novel states. In this thesis, the static and dynamic properties in the quantum spin system and geometrically frustrated spin system are examined. The static and dynamic information are directly obtained by neutron scattering technique. The projects presented in this thesis are outlined below.

### 1.6.1 $CsFeCl_3$

The quantum phase transition has attracted great interest for the condensed matter physics because the exotic phenomenon occurs in the vicinity of the quantum critical point. According to quantum field theory, the collective excitation in the ordered phase is expressed by the fluctuations of the phase and amplitude of the order parameter. The phase and amplitude modes correspond to the Nambu-Goldstone and Higgs modes, respectively. Since the Higgs mode is strongly enhanced in the vicinity of the quantum critical point, it is an intriguing topic to investigate the Higgs mode in materials showing quantum phase transition.

$CsFeCl_3$ is a singlet ground state magnet caused by a strong easy-plane magnetic anisotropy. The $Fe^{2+}$ ions carry pseudo-spin $s = 1$ at low temperatures and form a triangular lattice. Pressure-induced quantum phase transition was exhibited by magnetic susceptibility measurement under pressures. Thus, $CsFeCl_3$ is a model compound for investigation of the pressure-induced quantum phase transition in the easy-plane $S = 1$ antiferromagnet with the geometrical frustration. In the vicinity of the quantum critical point, the enhanced Higgs mode is expected. In addition, it is significant to verify a non-trivial effect of the geometrical frustration on the collective excitation. To our knowledge, there has been no report on the quantum phase transition in the frustrated spin systems.

To identify the static and dynamic spin states in the vicinity of the quantum critical point, the magnetic structure in the ordered state and magnetic excitation on the both sides of the quantum phase transition have been studied. Non-trivial collective excitation has been discussed by combination of the experiment and calculation. Neutron diffraction under pressure is performed at ZEBRA diffractometer in PSI, Switzerland. Magnetic excitation is measured at HRC in J-PARC/MLF, Japan and CTAX spectrometer in ORNL, USA.

### 1.6.2 $NaBa_2Mn_3F_{11}$

The geometrically frustrated spin system has been a major topic in condensed matter physics since the competition of the spin interaction from the lattice geometry gives a macroscopic degeneracy and unconventional magnetic states at low temperatures. In real compounds, small perturbations make the spin state drastically change at low energies, and a novel magnetic state is induced. Thus, it is important to discuss perturbations in the geometrically frustrated magnets. Recent theoretical study in the classical Kagome antiferromagnet proposed that the magnetic dipole-dipole (MDD) interaction induced a 120° structure with a tail-chase geometry and a zero energy mode in the excited state unlike an effect of DM interaction.

$NaBa_2Mn_3F_{11}$ is the Kagome-Triangular antiferromagnet showing an antiferromagnetic order at $T_N = 2$ K. Because of its small Curie-Weiss temperature of $-32$ K, the exchange interaction is weak compared with other Kagome antiferromagnets. This implies that the MDD interaction is more important than other perturbations such as the second-neighbor exchange interaction and DM interaction to determine the magnetic state. Thus, it is expected to observe the 120° structure with tail-chase geometry and the zero-energy mode.

In order to verify the tail-chase 120° structure and zero-energy mode for the classical Kagome

antiferromagnet with the MDD interaction, the magnetic structure and spin dynamics in $NaBa_2Mn_3F_{11}$ have been investigated. The spin model including the MDD interaction has been discussed. The magnetic structure is identified by powder neutron diffraction experiment performed at ECHIDNA diffractometer in ANSTO, Australia, and WISH diffractometer in ISIS, UK. The magnetic excitation is measured by inelastic neutron scattering technique at IN6 in ILL, France.

# Chapter 2

# Neutron Scattering

The neutron discovered by J. Chadwick in 1932, who was awarded the Nobel Prize in Physics 1935, is one of elementary particles as well as proton and electron. The neutron scattering technique was established by C. G. Shull and B. N. Brockhouse. They were awarded the Nobel Prize in Physics 1994 for their pioneering work on the neutron scattering techniques. The neutron scattering technique has following features:

1. Since the de Broglie wavelength of the neuron is same extent as a distance between atoms in a material, we can study the structure of the material using interference effect between the neutron and the material.

2. Neutron deeply penetrates inside the material because it has no charge and is not influenced by the Coulomb potential in the material. This easily enables us to investigate bulk properties in the materials.

3. Unlike the X-ray, the neutron scatters with an element having the small number of electrons such as hydrogen due to nuclear scattering. Thus, we can measure scatterings from the light atom.

4. Since the neutron has spin half, a magnetic scattering with magnetic materials occurs. From the magnetic scattering, we can study an arrangement of the spin and magnetic dynamics in the magnetic materials.

5. Energy scale of the thermal neutron is same extent as various excited energies in solid materials such as lattice vibration and magnetic excitation. Thus, neutron can easily cause inelastic scattering.

Nowadays, the neutron scattering experiment is performed in various field such as soft-matter and life science not only in the solid material.
In this thesis, the magnetic materials are investigated. The neutron scattering technique is hence very effective method to obtain the magnetic information.

## 2.1 Neutron scattering theory

A theoretical treatment of the neutron scattering is given in many textbooks such as Refs. [117, 118]. Here we denote a general expression of cross-section of the scattering process. It is considered that a neutron with a mass of $m_{\mathrm{n}}$ is scattered by a scattering system. When wavevectors and energies of the neutron at initial and final states are $\boldsymbol{k}$, $\boldsymbol{k}'$ and $E$, $E'$ in Fig. 2.1, the partial

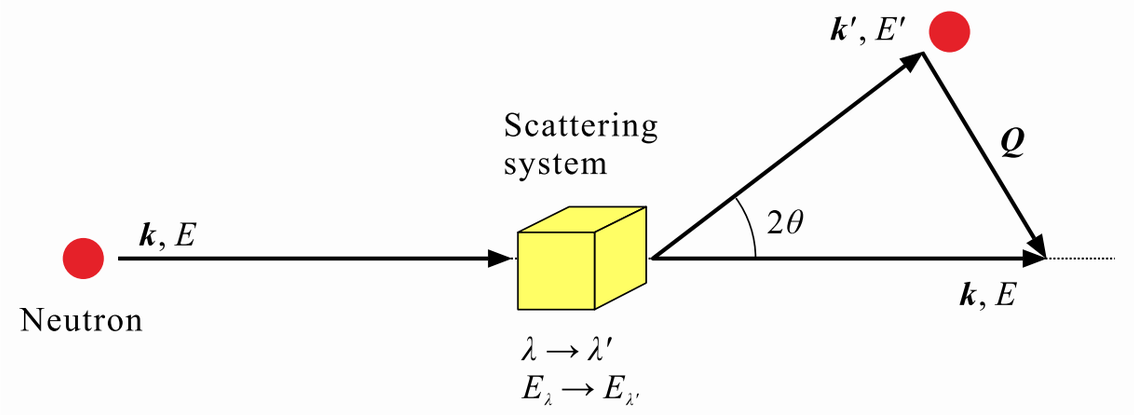


Figure 2.1 Geometry for scattering experiment.

differential cross-section is

$$\left(\frac{d^2\sigma}{d\Omega dE'}\right)_{\lambda\to\lambda'} = \frac{k'}{k}\left(\frac{m_{\rm n}}{2\pi\hbar^2}\right)^2 \left|\langle \boldsymbol{k}'\lambda'|\, V\, |\boldsymbol{k}\lambda\rangle\right|^2 \delta\left(E_\lambda - E_{\lambda'} + E - E'\right), \tag{2.1}$$

where $E_\lambda$ and $E_{\lambda'}$ are energies at initial $\lambda$ and final states $\lambda'$ of the scattering system, and $V$ is a potential of an interaction between the neutron and the scattering system. From conservation of the momentum and energy during the scattering process,

$$\boldsymbol{Q} = \boldsymbol{k} - \boldsymbol{k}', \tag{2.2}$$

$$\hbar\omega \equiv E - E' = E_{\lambda'} - E_\lambda, \tag{2.3}$$

where $\hbar\boldsymbol{Q}$ and $\hbar\omega$ are the momentum and energy transfers, respectively. In an actual experiment, we measure all processes in which the scattering system goes from a state $\lambda$ to another state $\lambda'$. To obtain this quantity, we sum Eq. (2.1) over all final states $\lambda'$, and average over all initial state $\lambda$. If the temperature of the scattering system is $T$, the probability $p_\lambda$ that is the scattering system is in the state $\lambda$ is given by the Boltzmann distribution as follow:

$$p_\lambda = \frac{1}{Z}\exp(-E_\lambda\beta), \tag{2.4}$$

where

$$Z = \sum_\lambda \exp(-E_\lambda\beta), \tag{2.5}$$

and

$$\beta = \frac{1}{k_{\rm B}T}. \tag{2.6}$$

$Z$ is the partition function. From Eqs. (2.1) and (2.4), we have

$$\frac{d^2\sigma}{d\Omega dE'} = \frac{k'}{k}\left(\frac{m_{\rm n}}{2\pi\hbar^2}\right)^2 \sum_{\lambda,\lambda'} p_\lambda \left|\langle \boldsymbol{k}'\lambda'|\, V\, |\boldsymbol{k}\lambda\rangle\right|^2 \delta\left(E_\lambda - E_{\lambda'} + E - E'\right), \tag{2.7}$$

The differential cross-section for unpolarized neutrons can be separated into the coherent and incoherent parts,

$$\frac{d^2\sigma}{d\Omega dE'} = \left(\frac{d^2\sigma}{d\Omega dE'}\right)_{\rm coh} + \left(\frac{d^2\sigma}{d\Omega dE'}\right)_{\rm inc}. \tag{2.8}$$

In general, we can obtain information on elastic Bragg scattering and inelastic scattering by phonon or magnon from the coherent scattering. On the other hand, the incoherent scattering provides the time correlations of the individual atoms. In the present section, the expressions of the cross-sections from the coherent scattering due to nuclear and magnetic scatterings are derived.

### 2.1.1 Nuclear scattering

When the position vector of the $j$th nucleus and that of the neutron represent $\boldsymbol{R}_j$ ($j = 1, \ldots, N$) and $\boldsymbol{r}$, the potential energy $V$ for the whole scattering system is expressed by

$$V = \sum_j V_j(\boldsymbol{r} - \boldsymbol{R}_j), \tag{2.9}$$

where $\mathrm{V}_j$ is the potential energy of the interaction between the $j$th nucleus and neutron. From this we have

$$\langle \boldsymbol{k}'\lambda' | \, V \, | \boldsymbol{k}\lambda \rangle = \sum_j V_j(\boldsymbol{Q}) \, \langle \lambda' | \exp(i\boldsymbol{Q} \cdot \boldsymbol{R}_j), | \lambda \rangle \tag{2.10}$$

$$V_j(\boldsymbol{Q}) = \int d\boldsymbol{x}_j V(\boldsymbol{x}_j) \exp(i\boldsymbol{Q} \cdot \boldsymbol{x}_j). \tag{2.11}$$

Since the strong force acts over very short distances, the nuclear potential for each atom is approximated by a Fermi pseudo-potential as,

$$V_j(\boldsymbol{x}_j) = \frac{2\pi\hbar^2}{m_\mathrm{n}} b_j \delta(\boldsymbol{x}_j), \tag{2.12}$$

where $b_j$ is the scattering length for the $j$th nucleus. In addition, we have

$$V_j(\boldsymbol{Q}) = \frac{2\pi\hbar^2}{m_\mathrm{n}} b_j. \tag{2.13}$$

From Eqs. (2.7), (2.10), and (2.13), the cross-section is represented by

$$\frac{d^2\sigma}{d\Omega dE'} = \frac{k'}{k} \sum_{\lambda,\lambda'} p_\lambda \left| \sum_j b_j \, \langle \lambda' | \exp(i\boldsymbol{Q} \cdot \boldsymbol{R}_j) \, | \lambda \rangle \right|^2 \delta \left( E_\lambda - E_{\lambda'} + E - E' \right). \tag{2.14}$$

Here we use the following expressions:

$$\delta \left( E_\lambda - E_{\lambda'} + \hbar\omega \right) = \frac{1}{2\pi\hbar} \int_{-\infty}^{\infty} dt \exp \left\{ i \frac{(E_{\lambda'} - E_\lambda)}{\hbar} t \right\} \exp(-i\omega t), \tag{2.15}$$

$$\exp \left( -i\mathcal{H}t/\hbar \right) | \lambda \rangle = \exp \left( -iE_\lambda t/\hbar \right) | \lambda \rangle \, , \tag{2.16}$$

where $\hbar\omega = E - E'$, and $\mathcal{H}$ is the Hamiltonian of the scattering system.

Eq. (2.14) is represented as

$$\begin{aligned} \frac{d^2\sigma}{d\Omega dE'} &= \frac{k'}{k} \frac{1}{2\pi\hbar} \sum_{j,j'} b_j b_{j'} \int_{-\infty}^{\infty} \exp(-i\omega t) \sum_\lambda p_\lambda \\ &\quad \times \langle \lambda | \exp \left( -i\boldsymbol{Q} \cdot \boldsymbol{R}_{j'} \right) \exp(i\mathcal{H}t/\hbar) \exp \left( -i\boldsymbol{Q} \cdot \boldsymbol{R}_j \right) \exp(-i\mathcal{H}t/\hbar) \, | \lambda \rangle \\ &= \frac{k'}{k} \frac{1}{2\pi\hbar} \sum_{j,j'} b_j b_{j'} \int_{-\infty}^{\infty} \exp(-i\omega t) \sum_\lambda p_\lambda \, \langle \lambda | \exp \left\{ -i\boldsymbol{Q} \cdot \boldsymbol{R}_{j'}(0) \right\} \exp \left\{ -i\boldsymbol{Q} \cdot \boldsymbol{R}_j(t) \right\} | \lambda \rangle \, . \end{aligned} \tag{2.17}$$

We define the thermal average of the operator $A$ as follow:

$$\langle A \rangle = \sum_{\lambda} p_{\lambda} \langle \lambda | A | \lambda \rangle . \tag{2.18}$$

Hence, the cross-section is represented by

$$\frac{d^2\sigma}{d\Omega dE'} = \frac{k'}{k} \frac{1}{2\pi\hbar} \sum_{j,j'} b_j b_{j'} \int_{-\infty}^{\infty} dt \, \langle \exp\{-i\boldsymbol{Q} \cdot \boldsymbol{R}_{j'}(0)\} \exp\{i\boldsymbol{Q} \cdot \boldsymbol{R}_j(t)\} \rangle \exp(-i\omega t). \tag{2.19}$$

Let us denote the cross-section of the nuclear scattering for crystalline solids. We consider only the coherent scattering for the simplicity, and the coherent scattering length is expressed by $\overline{b_j}$. For the crystalline solids, a lattice vector $\boldsymbol{l}$ and a reciprocal lattice vector $\boldsymbol{\tau}$ are defined as follow:

$$\boldsymbol{l} = l_1\boldsymbol{a}_1 + l_2\boldsymbol{a}_2 + l_3\boldsymbol{a}_3, \quad (l_i : \text{integer}) \tag{2.20}$$

$$\boldsymbol{\tau} = \tau_1\boldsymbol{b}_1 + \tau_2\boldsymbol{b}_2 + \tau_3\boldsymbol{b}_3, \quad (\tau_i : \text{integer}) \tag{2.21}$$

$$\boldsymbol{b}_1 = \frac{2\pi}{v_0}(\boldsymbol{a}_2 \times \boldsymbol{a}_3), \quad \boldsymbol{b}_2 = \frac{2\pi}{v_0}(\boldsymbol{a}_3 \times \boldsymbol{a}_1), \quad \boldsymbol{b}_3 = \frac{2\pi}{v_0}(\boldsymbol{a}_1 \times \boldsymbol{a}_2), \tag{2.22}$$

$$v_0 = \boldsymbol{a}_1 \cdot (\boldsymbol{a}_2 \times \boldsymbol{a}_3), \tag{2.23}$$

$$\boldsymbol{a}_i \cdot \boldsymbol{b}_j = 2\pi\delta_{ij}. \tag{2.24}$$

At a time $t$, the $d$-th nucleus position $\boldsymbol{R}_{ld}(t)$ in a unit cell $\boldsymbol{l}$ is expressed by

$$\boldsymbol{R}_{ld}(t) = \boldsymbol{l} + \boldsymbol{d} + \boldsymbol{u}_{ld}(t), \tag{2.25}$$

where $\boldsymbol{u}_{ld}(t)$ is a displacement vector by thermal motion. From this, the cross-section of the coherent scattering in Eq. (2.19) is expressed as

$$\begin{aligned} \frac{d^2\sigma}{d\Omega dE'} = \frac{k'}{k} \frac{1}{2\pi\hbar} \sum_{ld} \sum_{l'd'} \overline{b_d} \, \overline{b_{d'}} \exp\left\{i\boldsymbol{Q} \cdot (\boldsymbol{l}_d - \boldsymbol{l}'_{d'})\right\} \\ \times \int_{-\infty}^{\infty} dt \, \langle \exp\{-i\boldsymbol{Q} \cdot \boldsymbol{u}_{l'd'}(0)\} \exp\{i\boldsymbol{Q} \cdot \boldsymbol{u}_{ld}(t)\} \rangle \exp(-i\omega t). \end{aligned} \tag{2.26}$$

Here we use the following relation:

$$\langle \exp U \exp V \rangle = \exp\left\{\frac{1}{2}\left\langle U^2 + V^2 \right\rangle\right\} \exp\langle UV \rangle . \tag{2.27}$$

Then we have

$$\langle \exp\{-i\boldsymbol{Q} \cdot \boldsymbol{u}_{l'd'}(0)\} \exp\{i\boldsymbol{Q} \cdot \boldsymbol{u}_{ld}(t)\} \rangle = \exp\left\langle -\{\boldsymbol{Q} \cdot \boldsymbol{u}_{l'd'}(0)\}^2 \right\rangle \exp\langle -i\boldsymbol{Q} \cdot \{\boldsymbol{u}_{l'd'}(0) - \boldsymbol{u}_{ld}(t)\} \rangle , \tag{2.28}$$

where it is assumed that the thermal average of the square of the displacement does not depend on the time:

$$\exp\left\langle -\{\boldsymbol{Q} \cdot \boldsymbol{u}_{l'd'}(0)\}^2 \right\rangle = \exp\left\langle -\{\boldsymbol{Q} \cdot \boldsymbol{u}_{ld}(t)\}^2 \right\rangle . \tag{2.29}$$

Then the cross-section is represented as follow:

$$\begin{aligned} \frac{d^2\sigma}{d\Omega dE'} = \frac{k'}{k} \frac{1}{2\pi\hbar} \sum_{ld} \sum_{l'd'} \overline{b_d} \, \overline{b_{d'}} \exp\left\{i\boldsymbol{Q} \cdot (\boldsymbol{l}_d - \boldsymbol{l}'_{d'})\right\} \exp\left\langle -\{\boldsymbol{Q} \cdot \boldsymbol{u}_{l'd'}(0)\}^2 \right\rangle \\ \times \int_{-\infty}^{\infty} dt \exp\langle -i\boldsymbol{Q} \cdot \{\boldsymbol{u}_{l'd'}(0) - \boldsymbol{u}_{ld}(t)\} \rangle \exp(-i\omega t). \end{aligned} \tag{2.30}$$

Next we consider the elastic scattering ($E = E'$). For the elastic scattering, the displacement factor is expressed by

$$\exp\langle -i\boldsymbol{Q}\cdot\{\boldsymbol{u}_{l'd'}(0)-\boldsymbol{u}_{ld}(t)\}\rangle = 1. \tag{2.31}$$

The cross-section for the elastic scattering is

$$\begin{aligned}\left(\frac{d^2\sigma}{d\Omega}\right)_{\rm el} &= \frac{k'}{k}\frac{1}{2\pi\hbar}\sum_{ld}\sum_{l'd'}\overline{b_d}\;\overline{b_{d'}}\exp\left\{i\boldsymbol{Q}\cdot(\boldsymbol{l}_d-\boldsymbol{l}'_{d'})\right\}\exp\left\langle-\{\boldsymbol{Q}\cdot\boldsymbol{u}_{l'd'}\}^2\right\rangle \\ &= \sum_{ld}\sum_{l'd'}\overline{b_d}\;\overline{b_{d'}}\exp\left\{i\boldsymbol{Q}\cdot(\boldsymbol{l}-\boldsymbol{l}')\right\}\exp\left\{i\boldsymbol{Q}\cdot(\boldsymbol{d}-\boldsymbol{d}')\right\}\exp\left\langle-\{\boldsymbol{\kappa}\cdot\boldsymbol{u}_{l'd'}\}^2\right\rangle \\ &= N\sum_{l}\exp\{i\boldsymbol{Q}\cdot\boldsymbol{l}\}\sum_{d,d'}\overline{b_d}\;\overline{b_{d'}}\exp\left\{i\boldsymbol{Q}\cdot(\boldsymbol{d}-\boldsymbol{d}')\right\}\exp\left\langle-\{\boldsymbol{Q}\cdot\boldsymbol{u}_{l'd'}\}^2\right\rangle \\ &= N\sum_{l}\exp\{i\boldsymbol{Q}\cdot\boldsymbol{l}\}\left|\sum_{d}\overline{b_d}\exp(i\boldsymbol{Q}\cdot\boldsymbol{d})\exp(-W_d)\right|^2,\end{aligned} \tag{2.32}$$

where

$$\exp(-W_d) = \frac{1}{2}\left\langle\{\boldsymbol{Q}\cdot\boldsymbol{u}_{ld}\}^2\right\rangle \tag{2.33}$$

is the Debye-Waller factor due to the thermal motion. In addition, we use the Fourier transformation of the lattice vector $\boldsymbol{l}$

$$\sum_{l}\exp(i\boldsymbol{Q}\cdot\boldsymbol{l}) = \frac{(2\pi)^3}{v_0}\sum_{\tau}\delta(\boldsymbol{Q}-\boldsymbol{\tau}), \tag{2.34}$$

where $\boldsymbol{\tau}$ is the reciprocal lattice vector.

Therefore the coherent cross-section is

$$\left(\frac{d^2\sigma}{d\Omega}\right)_{\rm el} = N\frac{(2\pi)^3}{v_0}\sum_{\tau}\delta(\boldsymbol{Q}-\boldsymbol{\tau})\left|F_{\rm N}(\boldsymbol{Q})\right|^2, \tag{2.35}$$

$$F_{\rm N}(\boldsymbol{Q}) = \sum_{d}\overline{b_d}\exp(i\boldsymbol{Q}\cdot\boldsymbol{d})\exp(-W_d). \tag{2.36}$$

$F_{\rm N}(\boldsymbol{Q})$ is known as the nuclear unit-cell structure factor. Eq. (2.35) provides that the scattering occurs only when $\boldsymbol{Q} = \boldsymbol{\tau}$. This condition is the same as Bragg's law for X-ray scattering.

### 2.1.2 Magnetic scattering

The neutron has a magnetic moment of the spin half, which means that neutrons interact with a magnetic moment in a material. An elastic scattering from this interaction gives static information such as an arrangement of the magnetic moment. An inelastic magnetic scattering gives dynamical information such as spin wave excitation. Historically, C. G. Shull *et al*. reported the analysis of the magnetic structure on MnO by the neutron diffraction experiment for the first time in 1949 [119]. B. N. Brockhouse reported the observation of the spin wave excitation on $Fe_3O_4$ by the inelastic neutron scattering experiment [120]. One of advantages of the magnetic scattering by neutrons is that magnetic information in a material is directly observed without influence of the charge of electron showing magnetic property. Thus, the neutron scattering technique is an essential experimental method to study magnetism today.

The magnetic dipole moment of the neutron is

$$\boldsymbol{\mu}_{\rm n} = -\gamma\mu_{\rm N}\boldsymbol{\sigma}, \quad (\gamma = 1.913) \tag{2.37}$$

where

$$\mu_{\mathrm{N}} = \frac{e\hbar}{2m_{\mathrm{n}}} \tag{2.38}$$

is the nuclear magneton. $e$ is an elementary charge. $\boldsymbol{\sigma}$ is the Pauli spin operator for the neutron.

An electron with magnetic dipole moment $\boldsymbol{\mu}_e = -2\mu_{\mathrm{B}}\boldsymbol{s}$ and momentum $\boldsymbol{p}$ are considered. The magnetic fields at a point $\boldsymbol{R}$ from the electron due to $\boldsymbol{\mu}_e$ and $\boldsymbol{p}$ are respectively

$$\boldsymbol{B}_S = \mathrm{rot}\left(\frac{\mu_0}{4\pi}\frac{\boldsymbol{\mu}_{\mathrm{e}} \times \widehat{\boldsymbol{R}}}{R^2}\right), \tag{2.39}$$

$$\boldsymbol{B}_L = -\frac{\mu_0}{4\pi}\frac{2\mu_{\mathrm{B}}}{\hbar}\frac{\boldsymbol{p} \times \widehat{\boldsymbol{R}}}{R^2}, \tag{2.40}$$

where $\widehat{\boldsymbol{R}}$ is a unit vector in the direction of $\boldsymbol{R}$. The potential energy of the neutron with the magnetic dipole moment $\boldsymbol{\mu}_{\mathrm{n}}$ in these fields is represented by

$$\begin{aligned} V_{\mathrm{m}} = -\boldsymbol{\mu}_{\mathrm{n}} \cdot (\boldsymbol{B}_S + \boldsymbol{B}_L) &= -\frac{\mu_0}{4\pi}\gamma\mu_{\mathrm{N}} 2\mu_{\mathrm{B}} \boldsymbol{\sigma} \cdot (\boldsymbol{W}_S + \boldsymbol{W}_L) \\ &= -\gamma r_0 \frac{\hbar^2}{2m_{\mathrm{n}}} \boldsymbol{\sigma} \cdot (\boldsymbol{W}_S + \boldsymbol{W}_L) \end{aligned} \tag{2.41}$$

where

$$r_0 = \frac{\mu_0}{4\pi}\frac{e^2}{m_{\mathrm{e}}}, \tag{2.42}$$

$$\boldsymbol{W}_S = \mathrm{rot}\left(\frac{\boldsymbol{s} \times \widehat{\boldsymbol{R}}}{R^2}\right), \tag{2.43}$$

$$\boldsymbol{W}_L = \frac{1}{\hbar}\frac{\boldsymbol{p} \times \widehat{\boldsymbol{R}}}{R^2}. \tag{2.44}$$

The $r_0$ is known as the classical radius of the electron. $\boldsymbol{W}_S$ and $\boldsymbol{W}_L$ are contributions from the spin and orbital of the electron, respectively.

The cross-section including the neutron spin state $\boldsymbol{\sigma}$ is represented as follow:

$$\frac{d^2\sigma}{d\Omega dE'} = \frac{k'}{k}\left(\frac{m_{\mathrm{n}}}{2\pi\hbar^2}\right)^2 \sum_{\sigma,\sigma'}\sum_{\lambda,\lambda'} p_\sigma p_\lambda \left|\langle \boldsymbol{k}'\boldsymbol{\sigma}'\lambda'| V_{\mathrm{m}} |\boldsymbol{k}\boldsymbol{\sigma}\lambda\rangle\right|^2 \delta\left(E_\lambda - E_{\lambda'} + \hbar\omega\right), \tag{2.45}$$

where $p_\sigma$ is the probability that the neutron is initially in the state $\sigma$. From the potential energy Eq. (2.41), the cross-section is calculated by the magnetic scattering. The Fourier transform of the matrix element $\langle \boldsymbol{k}'| V_{\mathrm{m}} |\boldsymbol{k}\rangle$ can be found to be

$$\langle \boldsymbol{k}'| V_{\mathrm{m}} |\boldsymbol{k}\rangle = \gamma r_0 \frac{2\pi\hbar^2}{m_{\mathrm{n}}}\frac{1}{2\mu_{\mathrm{B}}} \boldsymbol{\sigma} \cdot \boldsymbol{M}_\perp(\boldsymbol{Q}), \tag{2.46}$$

where

$$\boldsymbol{M}_\perp(\boldsymbol{Q}) = \widehat{\boldsymbol{Q}} \times (\boldsymbol{M}(\boldsymbol{Q}) \times \widehat{\boldsymbol{Q}}) \tag{2.47}$$

$$= -2\mu_{\mathrm{B}} \sum_j \exp(i\boldsymbol{Q} \cdot \boldsymbol{r}_j)\left\{\widehat{\boldsymbol{Q}} \times (\boldsymbol{s}_j \times \widehat{\boldsymbol{Q}}) + \frac{i}{\hbar Q}(\boldsymbol{p}_j \times \widehat{\boldsymbol{Q}})\right\}. \tag{2.48}$$

From Eq. (2.46), the cross-section Eq. (2.45) is

$$\frac{d^2\sigma}{d\Omega dE'} = \left(\frac{\gamma r_0}{2\mu_{\mathrm{B}}}\right)^2 \frac{k'}{k} \sum_{\sigma,\sigma'}\sum_{\lambda,\lambda'} p_\sigma p_\lambda \left|\langle \boldsymbol{\sigma}'\lambda'| \boldsymbol{\sigma} \cdot \boldsymbol{M}_\perp(\boldsymbol{Q}) |\boldsymbol{\sigma}\lambda\rangle\right|^2 \delta\left(E_\lambda - E_{\lambda'} + \hbar\omega\right). \tag{2.49}$$

Since $\boldsymbol{M}_\perp(\boldsymbol{Q})$ does not depend on the spin state of the neutron $\sigma$, the sum on $\sigma$ and $\sigma'$ can be calculated as follow:

$$\begin{aligned}
&\sum_{\sigma,\sigma'} p_\sigma \left|\langle\sigma'\lambda'|\,\boldsymbol{\sigma}\cdot\boldsymbol{M}_\perp(\boldsymbol{Q})\,|\sigma\lambda\rangle\right|^2 \\
&= \sum_{\sigma,\sigma'} p_\sigma \sum_{\alpha,\beta=x,y,z} \langle\sigma|\,\sigma_\alpha\,|\sigma'\rangle\,\langle\sigma'|\,\sigma_\beta\,|\sigma\rangle\,\langle\lambda|\,M^\dagger_{\perp\alpha}(\boldsymbol{Q})\,|\lambda'\rangle\,\langle\lambda'|\,M_{\perp\beta}(\boldsymbol{Q})\,|\lambda\rangle \\
&= \sum_{\sigma} p_\sigma \sum_{\alpha,\beta} \langle\sigma|\,\sigma_\alpha\sigma_\beta\,|\sigma\rangle\,\langle\lambda|\,M^\dagger_{\perp\alpha}(\boldsymbol{Q})\,|\lambda'\rangle\,\langle\lambda'|\,M_{\perp\beta}(\boldsymbol{Q})\,|\lambda\rangle\,.
\end{aligned}$$

For unpolarized incident neutrons, the sum of the $\sigma$ becomes

$$\sum_{\sigma} p_\sigma\,\langle\sigma|\,\sigma_\alpha\sigma_\beta\,|\sigma\rangle = \begin{cases} 1 & (\alpha=\beta) \\ 0 & (\alpha\neq\beta) \end{cases}\,. \tag{2.50}$$

From this, the cross-section Eq. (2.49) is represented as follow:

$$\frac{d^2\sigma}{d\Omega dE'} = \left(\frac{\gamma r_0}{2\mu_\mathrm{B}}\right)^2 \frac{k'}{k} \sum_{\lambda,\lambda'} p_\lambda \left|\langle\lambda'|\,\boldsymbol{M}_\perp(\boldsymbol{Q})\,|\lambda\rangle\right|^2 \delta\left(E_\lambda - E_{\lambda'} + \hbar\omega\right). \tag{2.51}$$

It is useful to septate the cross-section to the elastic and inelastic parts as follow:

$$\frac{d^2\sigma}{d\Omega dE'} = \left(\frac{\gamma r_0}{2\mu_\mathrm{B}}\right)^2 \frac{k'}{k} \left[\left|\langle\boldsymbol{M}_\perp(\boldsymbol{Q})\rangle\right|^2 \delta\left(\hbar\omega\right) + \tilde{S}(\boldsymbol{Q},\omega)\right]. \tag{2.52}$$

$\left|\langle\boldsymbol{M}_\perp(\boldsymbol{Q})\rangle\right|^2$ is the elastic part giving static information such as a magnetic structure. $\tilde{S}(\boldsymbol{Q},\omega)$ is a dynamical structure factor without the static part which gives a dynamical information on a magnetic excited state. Hereafter we shall evaluate the elastic and inelastic parts of the magnetic scattering, respectively.

### Elastic magnetic scattering

The cross-section of the elastic scattering is

$$\begin{aligned}
\frac{d\sigma}{d\Omega} &= \left(\frac{\gamma r_0}{2\mu_\mathrm{B}}\right)^2 \left|\langle\boldsymbol{M}_\perp(\boldsymbol{Q})\rangle\right|^2 \\
&= \left(\frac{\gamma r_0}{2\mu_\mathrm{B}}\right)^2 \left|\widehat{\boldsymbol{Q}}\times\left(\langle\boldsymbol{M}(\boldsymbol{Q})\rangle\times\widehat{\boldsymbol{Q}}\right)\right|^2.
\end{aligned} \tag{2.53}$$

Firstly the magnetic scattering with only the spin of the electron is considered. When the position $\boldsymbol{r}_j$ of a $\nu$-th electron in a magnetic ion at the position $\boldsymbol{R}_{ld}$ is

$$\boldsymbol{r}_j = \boldsymbol{R}_{ld} + \boldsymbol{r}_\nu, \tag{2.54}$$

the operator $\boldsymbol{M}(\boldsymbol{Q})$ is represented as follow:

$$\boldsymbol{M}(\boldsymbol{Q}) = -2\mu_\mathrm{B} \sum_{l,d} \exp(i\boldsymbol{Q}\cdot\boldsymbol{R}_{ld}) \sum_{\nu} \exp(i\boldsymbol{Q}\cdot\boldsymbol{r}_\nu)\boldsymbol{s}_\nu. \tag{2.55}$$

The unpaired electrons at the site $\boldsymbol{R}_{ld}$ couple together, and the total spin operator $S_d$ is the quantum number. Since the neutron will not have enough energy to break down the coupled unpaired electron at the site $\boldsymbol{R}_{ld}$, the state $|\lambda\rangle$ in the scattering system depends on the total spin $S_{ld}$ and the position of the nucleus. We can therefore write

$$\langle\lambda|\,\boldsymbol{M}(\boldsymbol{Q})\,|\lambda\rangle = -2\mu_\mathrm{B} \sum_{l,d} f_d(\boldsymbol{Q})\,\langle\lambda|\exp(i\boldsymbol{Q}\cdot\boldsymbol{R}_{ld})\boldsymbol{S}_{ld}\,|\lambda\rangle\,, \tag{2.56}$$

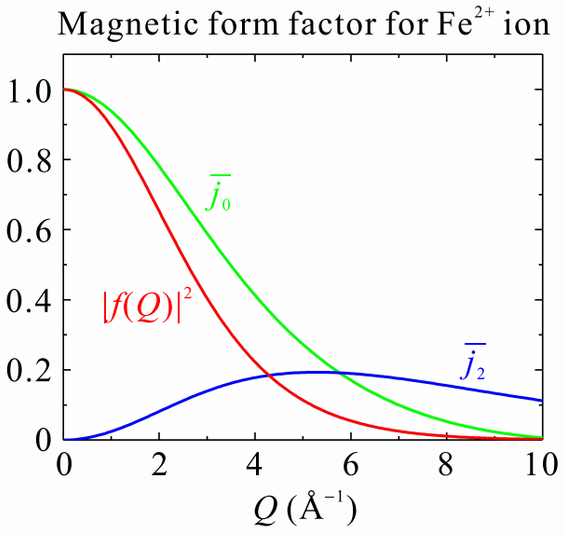


Figure 2.2 Free-ion magnetic form factor for $Fe^{2+}$ ion. The values of coefficients are taken from Ref. [121].

where

$$f_d(\boldsymbol{Q}) = \int d\boldsymbol{r}\hat{s}_d(\boldsymbol{r})\exp(i\boldsymbol{Q}\cdot\boldsymbol{r}). \tag{2.57}$$

$f_d(\boldsymbol{Q})$ is the magnetic form factor which is defined as the Fourier transform of the normalized spin density $\hat{s}_d(\boldsymbol{r})$ associated with the magnetic ion at the site $\boldsymbol{R}_{ld}$. The magnetic form factor Eq. (2.57) is conventionally approximated by a dipole moment as follow:

$$f(Q) = \overline{j_0} = 4\pi\int_0^\infty r^2 dr j_0(Qr)\hat{s}(\boldsymbol{r}), \tag{2.58}$$

where $j_n(Qr)$ is a spherical Bessel function of order $n$.

Next the contribution from the orbital angular momentum $\boldsymbol{W}_L$ is considered. The magnetic form factor should be modified. Using the dipole approximation, the magnetic form factor having the spin and orbital is represented as follow:

$$f(\boldsymbol{Q}) = \frac{g_S}{g}\overline{j_0} + \frac{g_L}{g}\left(\overline{j_0} + \overline{j_2}\right), \tag{2.59}$$

where

$$g = g_S + g_L, \tag{2.60}$$

$$g_{\mathrm{S}} = 1 + \frac{S(S+1) - L(L+1)}{J(J+1)}, \tag{2.61}$$

$$g_{\mathrm{L}} = \frac{1}{2} + \frac{L(L+1) - S(S+1)}{2J(J+1)}. \tag{2.62}$$

For the $d$ electrons of the transition metals and $f$ electron of the rare-earth metal, the $\overline{j_0}$ and $\overline{j_2}$ is conventionally approximated by analytical expressions [121]. In this approximation,

$$\overline{j_0} = Ae^{as^2} + Be^{bs^2} + Ce^{cs^2} + D, \tag{2.63}$$

$$\overline{j_2} = \left(Ae^{as^2} + Be^{bs^2} + Ce^{cs^2} + D\right)s^2, \tag{2.64}$$

where $s = Q/4\pi = \sin\theta/\lambda$, the neutron wavelength is denoted by $\lambda$ and the scattering angle is denoted by $2\theta$. Figure 2.2 shows a free-ion magnetic form factor for the $Fe^{2+}$ ion as a function of wavevector $Q$. The magnetic form factor $f(\boldsymbol{Q})$ monotonically decreases with increase of the $Q$, reflecting the real-space magnetic dipole moment decreasing away from the ion. In case of the $Fe^{2+}$ ion, the $f(\boldsymbol{Q})$ is reduced to be 20 % of that at $Q = 4$ Å$^{-1}$.

Using the magnetic form factor, Eq. (2.55) is represented as follow:

$$\boldsymbol{M}(\boldsymbol{Q}) = -2\mu_{\mathrm{B}} \sum_{l,d} f_d(\boldsymbol{Q}) \exp(i\boldsymbol{Q}\cdot\boldsymbol{R}_{ld})\boldsymbol{m}_{ld}, \tag{2.65}$$

where $\boldsymbol{m}_{ld}$ is a magnetic moment at the site $\boldsymbol{R}_{ld}$. In general, the magnetic structure is described by a magnetic propagation vector $\boldsymbol{k}_m$. The general expression of the magnetic moment at the site $\boldsymbol{R}_{ld}$ using the $\boldsymbol{k}_m$ is

$$\boldsymbol{m}_{ld} = \sum_{k_m} m_{d,k_m} \boldsymbol{\mu}_{d,k_m} \exp(i\boldsymbol{k}_m\cdot\boldsymbol{l}), \tag{2.66}$$

where $m_d$ is the magnitude of the magnetic moment, and the $\boldsymbol{\mu}_{d,k_m}$ is the unit-vector of the direction of the magnetic moment. In particular, when the magnetic structure is represented by a single magnetic propagation vector, we can write

$$\boldsymbol{m}_{ld} = m_d \left[\boldsymbol{\mu}_d \exp(i\boldsymbol{k}_m\cdot\boldsymbol{l}) + \boldsymbol{\mu}_d^* \exp(-i\boldsymbol{k}_m\cdot\boldsymbol{l})\right]. \tag{2.67}$$

The $\boldsymbol{\mu}_{d,-k_m}$ equals to $\boldsymbol{\mu}^*_{d,k_m}$ because $\boldsymbol{m}_{ld}$ is a real vector.

From Eqs. (2.65) and (2.67), we have the cross-section from the magnetic elastic scattering as follow:

$$\begin{aligned}\frac{d\sigma}{d\Omega} &= \left(\frac{\gamma r_0}{2\mu_{\mathrm{B}}}\right)^2 \left|\widehat{\boldsymbol{Q}} \times \left(\langle \boldsymbol{M}(\boldsymbol{Q})\rangle \times \widehat{\boldsymbol{Q}}\right)\right|^2 \\ &= (\gamma r_0)^2 \frac{(2\pi)^3}{v_0} \sum_{\boldsymbol{\tau}} \left|\widehat{\boldsymbol{Q}} \times \left(\boldsymbol{F}_{\mathrm{M}}(\boldsymbol{Q}) \times \widehat{\boldsymbol{Q}}\right)\right|^2 \left[\delta\left(\boldsymbol{Q} - \boldsymbol{\tau} + \boldsymbol{k}_m\right) + \delta\left(\boldsymbol{Q} - \boldsymbol{\tau} - \boldsymbol{k}_m\right)\right], \end{aligned} \tag{2.68}$$

where

$$\boldsymbol{F}_{\mathrm{M}}(\boldsymbol{Q}) = \sum_d f_d(\boldsymbol{Q}) \langle m_d\rangle \boldsymbol{\mu}_d \exp(i\boldsymbol{Q}\cdot\boldsymbol{d}) e^{-W_d}. \tag{2.69}$$

$\boldsymbol{F}_{\mathrm{M}}(\boldsymbol{Q})$ is known as the magnetic unit-cell structure factor, and $W_d$ is the Debye-Waller factor. $\langle m_d\rangle$ is the thermal-averaged magnitude of the magnetic moment.

Eq. (2.68) shows that magnetic Bragg scattering occurs when

$$\boldsymbol{Q} = \boldsymbol{\tau} \pm \boldsymbol{k}_m. \tag{2.70}$$

Thus, the magnetic Bragg peak appears at satellite positions from the nuclear Bragg peak. The neutron intensity of the magnetic Bragg peak depends on the $\langle m_d\rangle$. Since the $\langle m_d\rangle$ corresponds to the order parameter, the $\langle m_d\rangle$ in a critical region is

$$\langle m_d\rangle \sim |t|^{\beta}, \tag{2.71}$$

where $t$ is $(T - T_{\mathrm{C}})/T_{\mathrm{C}}$, and $T_{\mathrm{C}}$ is a transition temperature. The $\beta$ is a critical exponent. Therefore, measurement of the temperature dependence of the magnetic Bragg peak is important to discuss the criticality in the system.

Inelastic magnetic scattering

Next we denote the cross-section including the inelastic scattering part. For the sake of the simplicity, it is considered that the only spin contributes the magnetic scattering. Then Eq. (2.65) is represented by

$$\boldsymbol{M}(\boldsymbol{Q}) = -2\mu_{\mathrm{B}} \sum_{l,d} f_d(\boldsymbol{Q}) \exp(i\boldsymbol{Q}\cdot\boldsymbol{R}_{ld})\boldsymbol{S}_{ld}, \tag{2.72}$$

where $\boldsymbol{S}_{ld}$ is a spin operator at the site $\boldsymbol{R}_{ld}$. From Eqs. (2.51) and (2.72), we can write

$$\begin{aligned}\frac{d^2\sigma}{d\Omega dE'} &= (\gamma r_0)^2 \frac{k'}{k} \sum_{\lambda,\lambda'} p_\lambda \left| \widehat{\boldsymbol{Q}} \times \left( \langle\lambda'| \sum_{l,d} f_d(\boldsymbol{Q}) \exp(i\boldsymbol{Q}\cdot\boldsymbol{R}_{ld})\boldsymbol{S}_{ld} |\lambda\rangle \times \widehat{\boldsymbol{Q}} \right) \right|^2 \delta\left(E_\lambda - E_{\lambda'} + \hbar\omega\right) \\ &= (\gamma r_0)^2 \frac{k'}{k} \sum_{\lambda,\lambda'} p_\lambda \sum_{l,d} \sum_{l',d'} f_d(\boldsymbol{Q}) f^*_{d'}(\boldsymbol{Q}) \sum_{\alpha,\beta} \left(\delta_{\alpha\beta} - \widehat{Q}_\alpha \widehat{Q}_\beta\right) \\ &\quad \times \langle\lambda| \exp(-i\boldsymbol{Q}\cdot\boldsymbol{R}_{ld}) S^\alpha_{ld} |\lambda'\rangle \langle\lambda'| \exp(i\boldsymbol{Q}\cdot\boldsymbol{R}_{ld}) S^\beta_{ld} |\lambda\rangle \, \delta\left(E_\lambda - E_{\lambda'} + \hbar\omega\right), \end{aligned} \tag{2.73}$$

where $\{\alpha,\beta\} = \{x,y,z\}$ are Cartesian coordinations of the spin operator. Unlike nuclear scattering, the magnetic scattering contains a term $(\delta_{\alpha\beta} - \widehat{Q}_\alpha\widehat{Q}_\beta)$. This term selects the component of the magnetization which is perpendicular to the momentum transfer $\boldsymbol{Q}$.

Considering the expression in Eq. (2.73), we use following relations:

$$\delta\left(E_\lambda - E_{\lambda'} + \hbar\omega\right) = \frac{1}{2\pi\hbar} \int_{-\infty}^{\infty} dt \exp\left\{ i \frac{(E_{\lambda'} - E_\lambda)}{\hbar} t \right\} \exp(-i\omega t), \tag{2.74}$$

$$\exp\left(\frac{i\mathcal{H}t}{\hbar}\right) |\lambda\rangle = \exp\left(\frac{iE_\lambda t}{\hbar}\right) |\lambda\rangle . \tag{2.75}$$

The magnetic cross-section is represented as follow:

$$\begin{aligned}\frac{d^2\sigma}{d\Omega dE'} &= \frac{(\gamma r_0)^2}{2\pi\hbar} \frac{k'}{k} \sum_{\alpha,\beta} \left(\delta_{\alpha\beta} - \widehat{Q}_\alpha\widehat{Q}_\beta\right) \sum_{l,d} \sum_{l',d'} f_d(\boldsymbol{Q}) f^*_{d'}(\boldsymbol{Q}) \\ &\quad \times \int_{-\infty}^{\infty} dt \left\langle \exp\left\{-i\boldsymbol{Q}\cdot\boldsymbol{R}_{l'd'}(0)\right\} S^\alpha_{l'd'}(0) \exp\left\{i\boldsymbol{Q}\cdot\boldsymbol{R}_{ld}(t)\right\} S^\beta_{ld}(t) \right\rangle \exp(-i\omega t). \end{aligned} \tag{2.76}$$

When the electron spins weakly affect the motion of the nuclei, the thermal average $\langle\cdots\rangle$ can be separated to two parts. Considering only the spin fluctuation without the phonon, we have for the magnetic cross-section

$$\begin{aligned}\frac{d^2\sigma}{d\Omega dE'} &= \frac{(\gamma r_0)^2}{2\pi\hbar} \frac{k'}{k} \sum_{\alpha,\beta} \left(\delta_{\alpha\beta} - \widehat{Q}_\alpha\widehat{Q}_\beta\right) \sum_{d,d'} f_d(\boldsymbol{Q}) f^*_{d'}(\boldsymbol{Q}) \exp(-W_d) \exp(-W_{d'}) \\ &\quad \times \int_{-\infty}^{\infty} dt \left\langle S^\alpha_{d'}(\boldsymbol{Q},0) S^\beta_d(-\boldsymbol{Q},t) \right\rangle \exp(-i\omega t). \end{aligned} \tag{2.77}$$

$\left\langle S^\alpha_{d'}(\boldsymbol{Q},0) S^\beta_d(-\boldsymbol{Q},t) \right\rangle$ is known as a spin-spin correlation function. Thus, the magnetic scattering of the neutron scattering directly gives information on the magnetic correlation in the scattering system.

The magnetic cross-section is denoted by the response function $S(\boldsymbol{Q},\omega)$ as follow:

$$S(\boldsymbol{Q},\omega) = \sum_{\alpha,\beta} \left(\delta_{\alpha\beta} - \widehat{Q}_\alpha\widehat{Q}_\beta\right) S^{\alpha\beta}(\boldsymbol{Q},\omega), \tag{2.78}$$

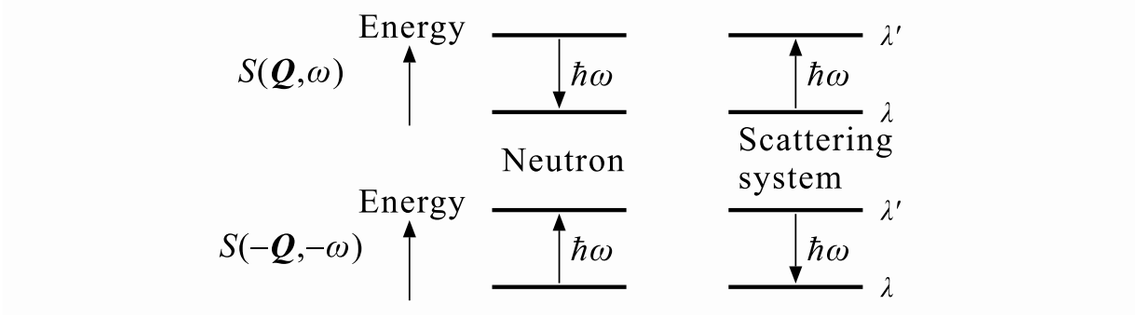


Figure 2.3 Diagram of the principle of detailed balance.

where

$$S^{\alpha\beta}(\boldsymbol{Q},\omega) = \frac{1}{2\pi\hbar}\sum_{d,d'} f_d(\boldsymbol{Q}) f^*_{d'}(\boldsymbol{Q}) \exp(-W_d)\exp(-W_{d'}) \times \int_{-\infty}^{\infty} dt \left\langle S^{\alpha}_{d'}(\boldsymbol{Q},0) S^{\beta}_{d}(-\boldsymbol{Q},t)\right\rangle \exp(-i\omega t). \tag{2.79}$$

Consider a relation of the two scattering processes: the neutron loses and gain the energy by the transition between two states $\lambda$ and $\lambda'$, in which the energy $E_{\lambda'}$ is larger than the energy $E_\lambda$ as shown in Fig. 2.3. When the temperature $T$ of the scattering system is stabilized by a thermal bath in a realistic system, the process in which the neutron loses the energy more likely occurs than that in which the neutron gains the energy. This is because that the two states $\lambda$ and $\lambda'$ are thermally populated. The proportion of the states $\lambda$ and $\lambda'$ is determined by the Boltzmann distribution $e^{-\hbar\omega/k_{\rm B}T}$. The response functions $S(\boldsymbol{Q},\omega)$ and $S(-\boldsymbol{Q},-\omega)$ are therefore determined by the principle of detailed balance as follow:

$$S(\boldsymbol{Q},\omega) = e^{\hbar\omega/k_{\rm B}T} S(-\boldsymbol{Q},-\omega). \tag{2.80}$$

Furthermore, according to the fluctuation-dissipation theorem, the dynamical part of $S(\boldsymbol{Q},\omega)$ relates to the imaginary part of the generalized susceptibility $\chi''(\boldsymbol{Q},\omega)$ by

$$\tilde{S}(\boldsymbol{Q},\omega) = \frac{1}{\pi}\left[1 + n(\hbar\omega)\right]\chi''(\boldsymbol{Q},\omega), \tag{2.81}$$

where $n(\hbar\omega) = [\exp(\hbar\omega/k_{\rm B}T) - 1]^{-1}$ is the Bose-Einstein distribution function. Thus, the temperature dependence of the cross-section from inelastic scattering is proportional to the Bose-Einstein distribution function.

## 2.2 Instrumentation

In this thesis, the neutron scattering experiments were performed in various facilities; Materials and Life Science Experimental Facility (MLF) at Japan Proton Accelerator Research Complex (J-PARC) in Japan, High Flux Isotope Reactor (HFIR) at Oak Ridge National Laboratory (ORNL) in USA, SINQ at Paul Scherrer Institut (PSI) in Switzerland, Open Pool Australian Light water (OPAL) reactor at Australian Nuclear Science and Technology Organisation (ANSTO) in Australia, ISIS at Rutherford Appleton Laboratory (RAL) in UK, and Insitut Laue-Langevin (ILL) in France. There we used various neutron scattering instruments; a powder neutron diffractometer (ECHIDNA in ANSTO), time-of-flight (TOF) diffractometer (WISH in ISIS), single-crystal diffractometer (ZEBRA in PSI), triple-axis spectrometer (CTAX in ORNL), and TOF spectrometer (HRC in J-PARC/MLF, IN4C and IN6 in ILL). In the present section, the

neutron scattering technique and instrumentations are explained. Detailed neutron scattering technique is given in many textbooks such as Ref. [122].

### 2.2.1 Neutron sources

Neutrons are produced in various nuclear reactions including fission, photofission, spallation, and fusion. For neutron scattering experiments, the neutrons are mostly provided by the fission and spallation. The fission takes place using a nuclear research reactor, and is the most common way to provide the neutrons. HFIR in ORNL, OPAL in ANSTO, and ILL correspond to the nuclear research reactors. In a nuclear reactor fueled with uranium $^{235}$U, fission of the $^{235}$U proceed as follow:

$$^{235}\mathrm{U} + \mathrm{n} \longrightarrow \text{ two fission fragments} + 2.7\mathrm{n}, \tag{2.82}$$

where 2.7 fast neutrons on average are produced, and the nucleus is disintegrated into two fission fragments. The produced neutron reacts with other uranium one after another, which is called *chian-reaction*. The energy of the produced neutrons is $\sim 10^6$ eV (1 MeV). When the neutrons are used for the scattering experiments, its energy is reduced to be about $\sim 10^{-3}$ eV (1 meV) using moderator such as light water and heavy water.

The spallation takes place by using *accelarator-based* sources. In the spallation process, a nuclear reaction occurs when a high-energy particle such as a proton collides with a heavy atom which is called a target. First, the high-energy proton hits to the nucleus of the target. It causes an internal nucleon cascade within the excited-target nucleus. Then high-energy neutrons are emitted and absorbed by other nuclei. After this, de-excitation of various target occurs with emission of many low-energy neutrons, whose energies are $\sim$ 50 MeV. This process is called *evaporation*. 3 % of the total neutrons is produced in the process of the cascade, which means that the most neurons are produced through the evaporation process. In regard to the accelerators, synchrotrons in J-PARC and ISIS provide pulsed neutron beams, and a cyclotron in PSI provides a continuous neutron beam.

### 2.2.2 Neutron detection

Neutrons are detected using an ionization of secondary particles produced by a nuclear reaction between neutrons and absorbing materials. The most common nuclear reactions used in the neutron detection are

$$^{3}\mathrm{He} + \mathrm{n} \longrightarrow {}^{3}\mathrm{H} + \mathrm{p} + 0.8 \text{ MeV}, \tag{2.83}$$

$$^{10}\mathrm{B} + \mathrm{n} \longrightarrow {}^{7}\mathrm{Li} + {}^{4}\mathrm{He} + 2.3 \text{ MeV}, \tag{2.84}$$

$$^{6}\mathrm{Li} + \mathrm{n} \longrightarrow {}^{4}\mathrm{He} + {}^{3}\mathrm{He} + 4.8 \text{ MeV}, \tag{2.85}$$

$$^{235}\mathrm{U} + \mathrm{n} \longrightarrow \text{ two fission fragments} + 190 \text{ MeV}. \tag{2.86}$$

The first and second reactions are employed in gas detectors, the third one in scintillation detectors and the last one in fission chambers for monitoring the incident beam.

The gas detector is constructed by enclosing the absorbing material such as $^{3}$He and $^{10}BF_3$ in a cylindrical metal tube. In the $^{3}$He detector, for example, the proton and triton from the nuclear reaction in Eq. (2.83) are ionized and collected by an anode wire at high voltage. It causes a pulsed current and it is recorded. When the anode wire made of a resistive material which is a glass fiber coated with a thin metallic layer, the gas detector can measure a position of neutron detection in the tube as shown in Fig. 2.4(a). A neutron captured at the position $x$ along the tube produces a charge. The amplitude of the charge is measured at both ends of the detector. Considering the resistance of the wire, the charge is divided in the ratio of the distance $x$ and $1-x$ and the position of the neutron is determined by the ration $q_1/q_2$ of the two charge measurements. This technique realizes a position-sensitive detector (PSD). In early TOF

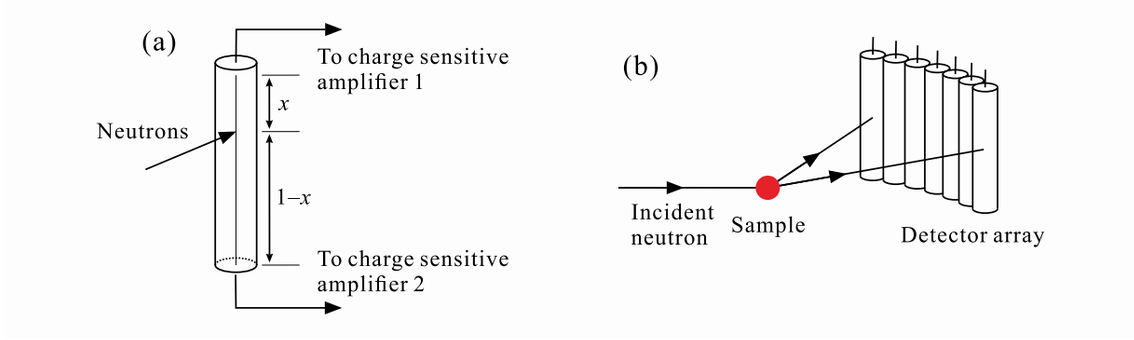


Figure 2.4 (a) The resistive-wire, position sensitive detector. The charges measured by the two amplifiers are $q_1$ and $q_2$, and $x$ is given by $x = q_1/(q_1 + q_2)$. (b) Array of individual detectors.

spectrometers, the many PSDs with long tubes are arrayed as shown in Fig. 2.4(b). It enables us to assemble the data in wide space, simultaneously.

A scintillation detector is constructed by mixing a neutron absorbing material such as Li salt and scintillator material such as ZnS. Initially, the burst of the light is emitted by absorption of a neutron and ionization of secondary particles. Then the light is amplified by photomultiplier and is recorded.

### 2.2.3 Monochromatic neutron and spectroscopy

For scattering experiments, it is necessary to select a specific neutron energy for the monochromatization and spectroscopy. Conventionally, there are two methods to determine the neutron energy; a crystal monochromator and mechanical chopper. The two techniques are described below.

#### Crystal monochromator

The simplest method selecting a monochromatic neutron beam is provided by diffraction from the single crystal. When neutrons are diffracted at a scattering plane with a plane-spacing $d$ and at a scattering angle $2\theta_{\mathrm{B}}$, the neutron wavelength $\lambda$ is determined by Bragg's law

$$\lambda = 2d \sin \theta_{\mathrm{B}}. \tag{2.87}$$

From the Bragg reflection, a monochromatic neutron is obtained as shown in Fig. 2.5(a).

A crystal monochromator will also reflect neutrons with the wavelength $\lambda/2$, $\lambda/3$, ..., which are higher harmonic waves. The higher harmonic wave causes experimental noise and background. In order to remove unwanted wavelength, a polycrystalline beam filter is usually used. Since all orientations are present in a polycrystalline material, the all wavelengths are scattered in satisfaction of the Bragg's law. However, there is a maximum wavelength $\lambda_{\max}$ beyond which there is no Bragg reflection. The maximum wavelength is given by $\lambda_{\max} = 2d_{\max}$, where $d_{\max}$ is the maximum plane spacing in the material. This is known as the Bragg-cut-off wavelength. The neutron having the wavelength beyond the $\lambda_{\max}$ nearly transmits to the filter. The cut-off wavelength depends on filter materials; a beryllium for the cold neutron and a pyrolitic graphite (PG) for the thermal neutron. Thus, it can remove high-energy neutrons with the higher harmonic wavelength.

As the beam flux in neutron scattering is limited, focusing techniques is important to increase neutron count rates. Arrays of monochromator crystals which focus the neutron beam enable us to gain more intensity than a single crystal. There are two focusing geometries: vertical and horizontal. In vertical focusing, the scattering triangle ABC is rotated about the line AC, and

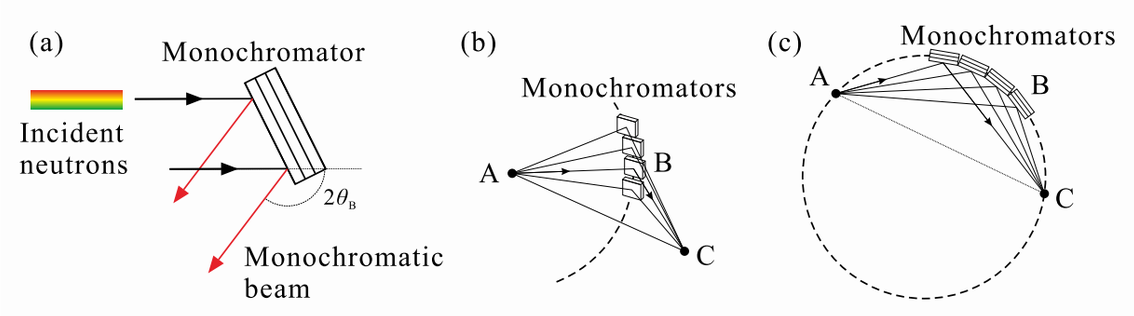


Figure 2.5 (a) Diagram of the monochromatization of the incident neutron by Bragg reflection. Diagram (b) shows vertical focusing array and (c) shows horizontal focusing.

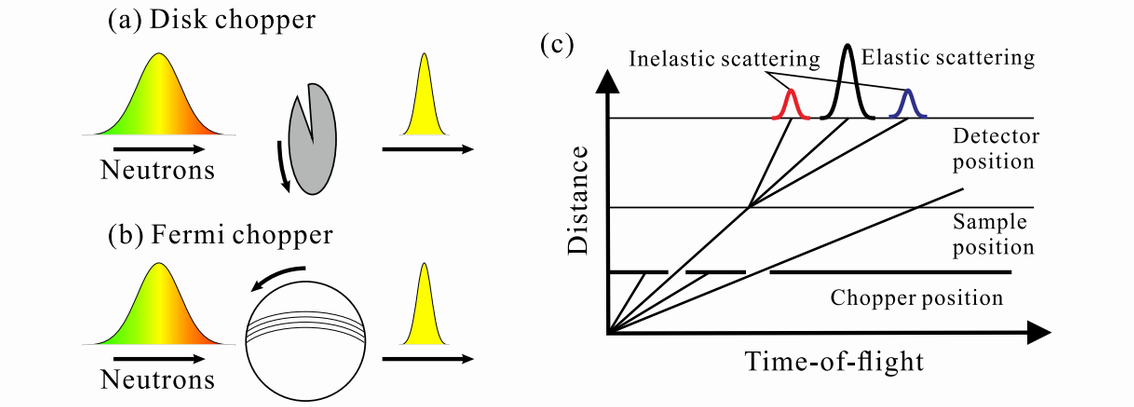


Figure 2.6 Schematic diagrams of (a) Disc chopper and (b) Fermi chopper. (c) Diagram of the TOF spectroscopy.

the crystals are stacked above and below the horizontal scattering plane as shown in Fig. 2.5(b). In horizontal focusing, the point B is kept on the horizontal plane and the crystals are put along the circumference as shown in Fig. 2.5(c).

### Chopper and time-of-flight spectroscopy

The neutron velocity $v$ is related to the wavelength $\lambda$ through the de Broglie relationship as follow:

$$\lambda = \frac{h}{m_{\mathrm{n}} v}, \tag{2.88}$$

where $h$ is the Planck constant and $m_{\mathrm{n}}$ is the neutron mass. The velocity can be measured by a TOF of the neutron when a distance is known. This means that the neutron energy is selected and monochromated by the TOF. In order to select the neutron energy by its velocity, a mechanical chopper is used. The chopper is slotted and rotated. The only neutron beam which is timed to the slot can pass through the chopper. Consequently, the neutrons can be monochromated and pulsed.

There are two types of the choppers; disk chopper and Fermi chopper. For the disk chopper, the disk is slotted, and is rotated about the parallel direction to the incident beam as shown in Fig. 2.6(a). The energy resolution for the chopper spectrometer depends on the width of the incident neutron beam. The width of the pulsed neutron is determined by the time taken by the slot in the chopper to transverse the neutron beam. In general, the energy resolution for the single-disk chopper is not high. In order to realize high energy-resolution, the multiple-disk

choppers are used. We can obtain the sharp-edged incident neutron by means of the multiple-disk choppers.

For the Fermi chopper, the slots are cut across the diameter of the cylinder as shown in Fig 2.6(b). The chopper is rotated about the perpendicular direction to the incident beam. The Fermi chopper is more compact than the disk chopper. Consequently, the Fermi chopper can be rotated faster than the disk one, and provide a shorter pulse width. In HRC and IN6 spectrometers, the Fermi choppers are used, and they realize the high energy-resolution.

By combination of the chopper and measurement of the TOF, the neutron velocity and energy are analyzed. Figure 2.6(c) shows a schematic diagram of the TOF spectroscopy. The monochromatic neutron by the chopper is scattered with the sample and detected by detectors. Then the detectors measure not only the detection position but also arrival time of the neutron from the neutron production. Since the distance of the neutron flight path is fixed, the neutron velocity and energy are given by the measurement of the neutron TOF.

### 2.2.4 Neutron diffractometer

When a Bragg reflection occurs at a scattering plane $(hkl)$ or a plane-spacing $d$, a neutron intensity $I$ is a function of a scattering angle $2\theta$ and a neutron wavelength $\lambda$ because of the Bragg's law $d = \lambda/2\sin\theta$. In addition, according to the de Broglie relationship Eq. (2.88), the $\lambda$ is represented by a neutron TOF $t$ as follow:

$$\lambda = \frac{h}{m_{\mathrm{n}}L}t, \tag{2.89}$$

where $L$ is the total distance of the neutron flight path. Thus, neutron intensity $I$ is a function of $2\theta$, $\lambda$, or $2\theta$, $t$ as follow:

$$I = I(2\theta, \lambda) = I(2\theta, t). \tag{2.90}$$

In the diffraction experiment, the neutron intensity is measured by fixing the wavelength $\lambda$ or the scattering angle $2\theta$. A diffractometer in which the $\lambda$ is fixed and the intensity is measured as a function of the $2\theta$ is called an angle-dispersive diffractometer, and that in which the $2\theta$ is fixed and the intensity measured as a function of the $t$ is called a TOF (energy) dispersive diffractometer.

#### ECHIDNA

ECHIDNA diffractometer installed at OPAL reactor in ANSTO, Australia, is the angle-dispersive powder diffractometer [123]. Figure 2.7(a) shows the diagram of the ECHIDNA diffractometer. An incident neutron beam is monochromated by a germanium single crystal. The wavelength range of the monochromatic neutron is from 1 Å to 3 Å. The common germanium Bragg reflections are $(hhl) = (331)$, $(335)$, $(337)$. The scattered neutrons from the sample are collected by 128 linear $^3$He gas PSDs of 25 mm diameter and 300 mm hight. In front of the PSD, a $5'$ collimator is inserted. The detectors array can move around the circumference consisting of the scattering angle $2\theta$. Consequently, it enables to finely measure the $2\theta$ of the diffraction pattern.

#### WISH

WISH diffractometer installed in ISIS, UK, is the TOF dispersive diffractometer [124]. Figure 2.7(b) shows the diagram of the WISH diffractometer. To select bandwidth of the incident neutron, two double-disk choppers and a single-disk chopper are used. The detector array is consist of $^3$He gas PSDs of 8 mm diameter and 1 m hight in a range from $2\theta = 10°$ to $170°$. Owing to using a long-wavelength neutron and long neutron flight path, the WISH diffractometer achieves the very high resolution of the plane spacing $d$. In a powder diffraction experiment, the detector array is divided to 10 banks as shown in Fig. 2.7(b), and the collected data are integrated at each bank.

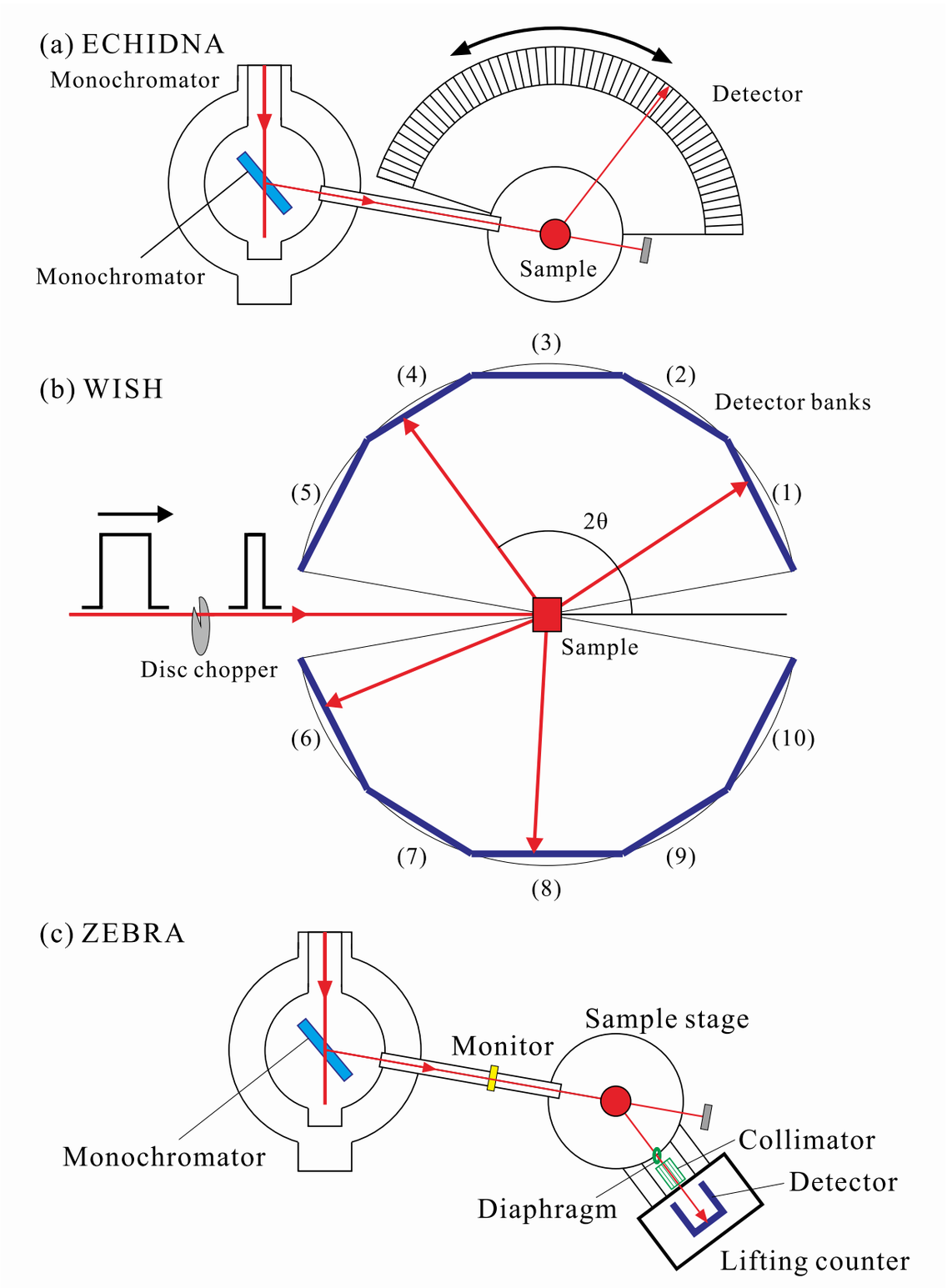


Figure 2.7 Diagrams of (a) a high resolution powder diffractometer ECHIDNA in ANSTO, (b) a long-wavelength TOF diffractometer WISH in ISIS, and (c) a single crystal diffractometer ZEBRA in PSI.

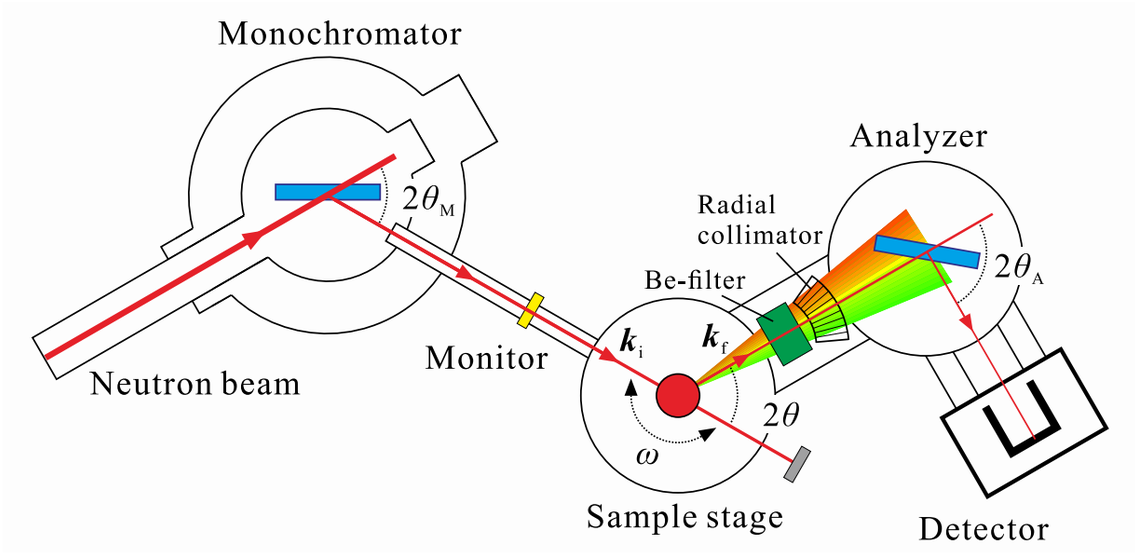


Figure 2.8 Schematic diagram of a triple-axis spectrometer. The neutron beam is shown by the red line. The monochromator, sample stage, and analyzer are able to rotate to obtain the required momentum and energy transfer.

ZEBRA

ZEBRA diffractometer installed at SINQ in PSI, Switzerland, is the angle dispersive single crystal diffractometer. Diagram of the instrument is shown in Fig. 2.7(c). The incident neutron is monochromated by vertical focusing monochromator of a germanium single crystal Ge (311) ($\lambda = 1.177$ Å) or PG (002) ($\lambda = 2.317$ Å). The scattered neutron is detected by 1D $^3$He detector or 2D $^3$He area detector of 160 mm $\times$ 160 mm. The position of the detector can be vertically lifted in a range of $\pm 15^\circ$ from the horizontal plane. This enables us to measure out-of-plane reflections.

### 2.2.5 Neutron spectrometer

In the inelastic neutron scattering (INS) experiment, the neutron intensity which we measure is a function of the energy transfer $\hbar\omega$ and the momentum transfer $\hbar\boldsymbol{Q}$. There are two types of the spectrometer; a triple-axis spectrometer and a TOF spectrometer. In the triple-axis spectrometer, we have to choose a measuring point and information about the excitations is obtained one-by-one in $(\boldsymbol{Q}, \omega)$ space. In contrast, the TOF spectrometer with numerous detector array gives an overview information of the excitations in a broad range of $(\boldsymbol{Q}, \omega)$ space. Hereafter these instruments are described.

Triple-axis-spectrometer

The triple-axis spectrometer (TAS) has been widely used to study dynamic properties such as thermal excitation and magnetic excitation. The name TAS refers to the axes of the three components of the instruments; the monochromator, the sample, and the analyzer. Figure 2.8 is a schematic diagram of the TAS. The monochromator selects the energy of the incident neutron from the white neutron beam emerging from the neutron source, and defines the wave vector $\boldsymbol{k}_\mathrm{i}$. The neutron having the $\boldsymbol{k}_i$ is scattered with the sample. An access point in the reciprocal space is determined by the scattering angle $2\theta$ and the angle of the rotation of the sample $\omega$. The analyzer selects a particular final wave vector $\boldsymbol{k}_\mathrm{f}$ from the scattered neutron. In this way, the neutron intensity in $(\boldsymbol{Q}, \omega)$ is measured at one-by-one using TAS.

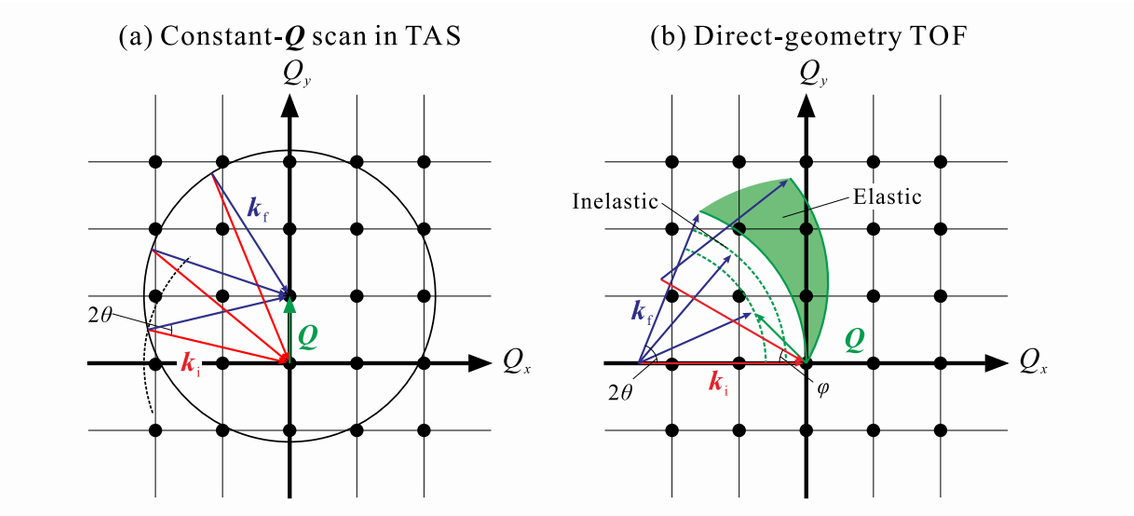


Figure 2.9 (a) Schematic diagram of TAS measurement at constant $\boldsymbol{Q}$ and at a fixed final wave vector $\boldsymbol{k}_f$. (b) Schematic diagram of direct-geometry TOF measurement.

A typical method to measure the inelastic scattering spectrum is a constant-$\boldsymbol{Q}$ scan. The energy transfer $\hbar\omega$ is obtained by fixing incident energy $E_i$ or final energy $E_f$ at a constant. Figure 2.9(a) shows the procedure for the measurement fixing the final energy $E_f$ at a constant. The energy scan is achieved by keeping $k_f$ while changing the angle $2\theta$ and $\omega$ to keep $\boldsymbol{Q}$ at a constant. Thus, the $\boldsymbol{k}_i$ and $\boldsymbol{k}_f$ move around a circular arc centered on the origin at $\boldsymbol{Q}$.

### CTAX

The CTAX is a cold neutron TAS installed at the CG4 guide tube of the High Flux Isotope Reactor (HFIR) in Oak Ridge National Laboratory (ORNL), USA. The incident neutron is monochromated by a vertically focusing monochromator PG (002), for which the energy range of the incident neutron is 2-20 meV. The energy of the scattered neutron is also selected by an analyzer PG (002), for which the lowest energy is 3 meV. Optionally, the analyzer can be set to vertically and/or horizontally focusing geometry. The higher harmonic wavelengths is removed by Be filter installed between the sample stage and analyzer as shown in Fig. 2.8.

### Time-of-flight spectrometer

Time-of-flight (TOF) spectrometers are classified to two types; *direct*-geometry spectrometer and *indirect*-geometry spectrometer. In the direct-geometry spectrometer, the incident energy $E_i$ is selected by a chopper, and the final energy $E_f$ is measured by TOF. In the indirect-geometry spectrometer, in contrast, the incident energy $E_i$ is measured by TOF and the final energy $E_f$ is fixed by analyzer crystals. Since the direct-geometry TOF spectrometer was used in this thesis, its technique is described.

Figure 2.10(a) shows a schematic diagram of the direct-geometry TOF spectrometer using a pulsed neutron source. The white neutron beam provided by the spallation reaction is monochromated by a disk chopper or Fermi chopper. Before monochromating the neutron beam, another choppers are used to reduce the background, which is called $T_0$ chopper. The monochromatic neutron beam with $\boldsymbol{k}_i$ is scattered with the sample. The detector array, which is usually PSDs array, measures the detected position and TOF from the production of the pulsed neutron. The range of the elastic and inelastic scattering measured in $(\boldsymbol{Q},\omega)$ space is shown in Fig. 2.9(b). Rotating the sample enables to move the measured reciprocal space and gives data in a wide range as a green region in Fig. 2.9(b).

#### HRC

The High Resolution Chopper (HRC) spectrometer is a TOF spectrometer installed at a spallation neutron source J-PARC/MLF in Japan [125, 126, 127]. Figure 2.10(b) illustrates HRC spectrometer. The incident neutron is monochromated by a Fermi chopper after a background chopper ($T_0$ chopper) rotating with 50 Hz excludes a higher energy neutron. We can widely select the incident neutron energy from 10 meV to 500 meV. The scattered neutrons are detected by $^3$He gas PSD array. The scattering angle is vertically $2\theta = \pm 20^\circ$ and horizontally $2\theta < 60^\circ$ (in 2017). The energy resolution is $\Delta E/E_i > 2.5$ % at elastic position.

#### IN6

IN6 spectrometer is a cold neutron time-focusing TOF spectrometer installed at the High Flux Reactor of the Institut Laue-Langevin (ILL) in France. IN6 spectrometer use a time focusing technique unlike HRC spectrometer. In the time focusing technique, three intense neutrons are extracted from white neutron beam by an assembly of three monochromators. Hence, each monochromator selects a neutron beam of distinct energy and of distinct velocity caused by different Bragg conditions. The three neutron beams are pulsed by a Fermi chopper. Then the fastest neutron beam pass the chopper after the slowest one pass it. Consequently, pulses of fast neutrons catch up with those of slower neutron after the chopper. This technique enables to increase intensity by a factor of three which corresponds to the number of spectrometer. Available wavelengths of the incident neutron are 4.1, 4.6, 5.1, 5.9 Å. A energy resolution at 5.1 Å is 70 $\mu$eV at elastic position. The scattered neutrons are detected by $^3$He gas PSD array. The scattering angle is vertically $2\theta = \pm 15^\circ$ and horizontally $10^\circ < 2\theta < 115^\circ$.

### 2.2.6 TAS vs TOF spectrometer

As mentioned above, it is advantage for TOF spectrometer to measure the neutron intensity in the broad range of $(\boldsymbol{Q}, \omega)$-space owing to numerous detector arrays. Thus, we can obtain an overview information of the excitation more efficiently than the TAS. In addition, inelastic neutron scattering spectrum for a powder sample having a dispersive excitation can be easily measured by the TOF spectrometer. The dispersive excitation of the powder sample usually becomes a broad spectrum in $(\boldsymbol{Q}, \omega)$-space because the spectrum is powder-averaged.

In contrast, the TAS has an advantage to access a specific point in $(\boldsymbol{Q}, \omega)$-space. When we measure a single point in $(\boldsymbol{Q}, \omega)$-space, the measurement efficiency of the TAS is better than that of the TOF spectrometer. This enables TAS to easily measure a spectrum at a specific point with varying external parameters such as temperature, magnetic field and pressure. The TAS is suit to track a parameter evolution of the neutron spectra. In this study therefore we used both types of spectrometers in response to purpose of the experiment.

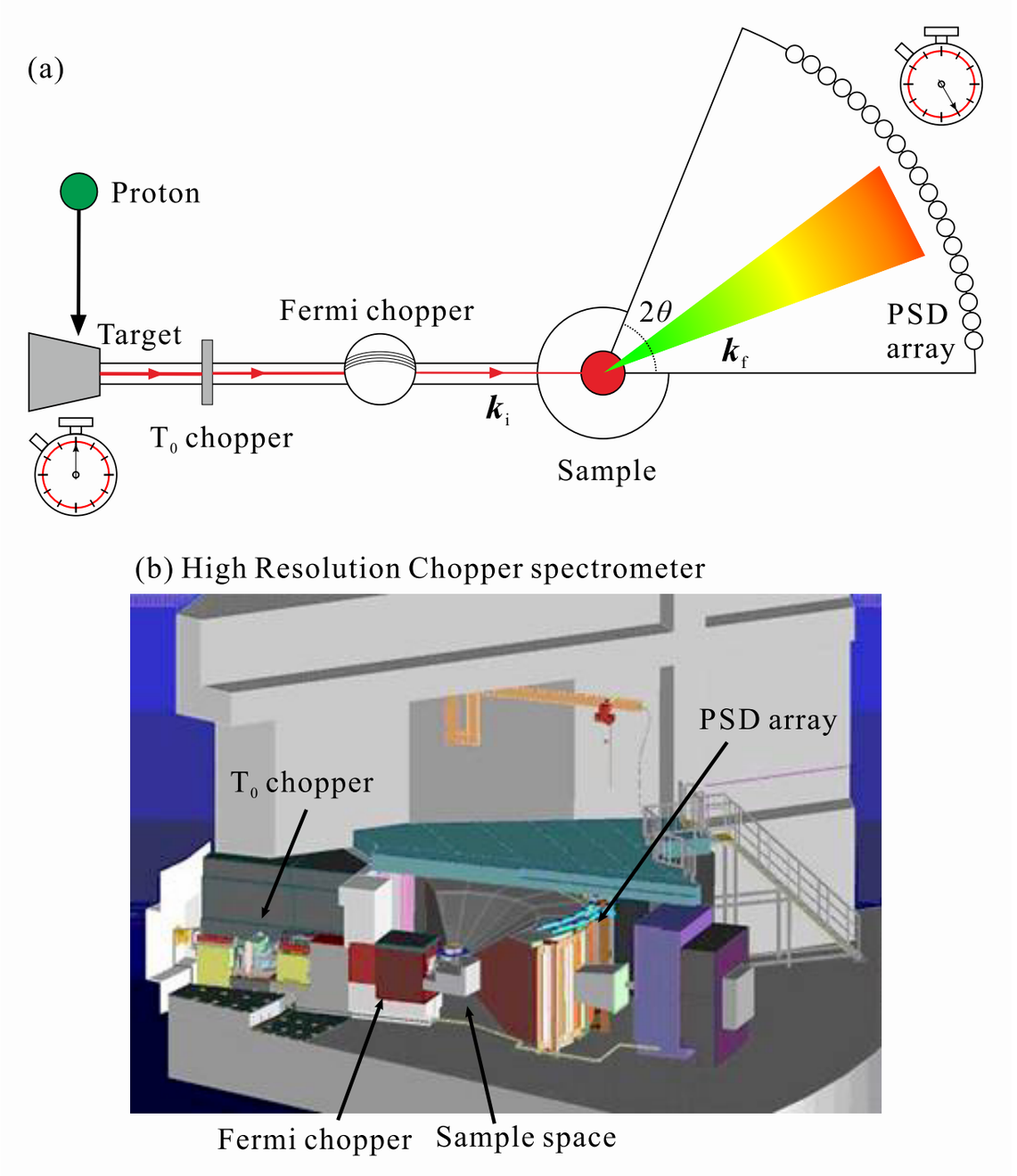


Figure 2.10 (a) Schematic diagram of a TOF chopper spectrometer. The neutron beam is shown by the red line. (b) Schematic diagram of HRC spectrometer at J-PARC/MLF as an example of a TOF instrument.

3章は学術誌掲載の形で刊行される予定のため、インターネット公表できません。

4 章は学術誌掲載の形で刊行される予定のため、インターネット公表できません。

# Chapter 5

# Concluding remarks and outlook

In this thesis, the spin systems have been investigated by means of the neutron scattering technique. It has been demonstrated that the neutron scattering experiments provided direct information on the magnetic state. We studied the two spin systems; the singlet ground state magnet $CsFeCl_3$ which occurs pressure-induced quantum phase transition, and the Kagome antiferromagnet having the MDD interaction $NaBa_2Mn_3F_{11}$. In the following, these studies are summarized, and future works are proposed.

## 5.1 $CsFeCl_3$

Work on the singlet ground state magnet $CsFeCl_3$ has examined the pressure-induced magnetic long-range order and unique collective spin excitations. In neutron diffraction experiment, the pressure-induced magnetic long-range order of the 120° structure was evidenced by observation of the magnetic Bragg peaks under pressure. The estimate of the critical exponent of the order parameter indicated that the symmetry in the ordered phase belonged to $U(1) \times Z_2$ universality class. This suggests that the chiral liquid state is realized in the vicinity of the quantum critical point. In order to detect the chiral liquid phase, we propose to measure electric polarization and dielectric permittivity under pressure for the future work. The information of the chiral order emerges as the dielectric property for the magnetoelectric effect.

Inelastic neutron scattering experiment under pressures demonstrated the softening of the magnetic excitation in the singlet phase. In the ordered phase, the unconventional collective excitation was observed. The collective excitation in the ordered phase exhibited a continuum-like gapless excitation and a well-defined excitation with the minimum energy of 0.6 meV. From the spin wave calculation based on the bond operator theory, it was found that the gapless excitation corresponded the conventional Nambu-Goldstone mode, and the well-defined excitation was mainly described by the non-trivial mixed mode of the traverse and longitudinal fluctuations (T+L-mode). It is found that the geometrical frustration causes the non-trivial T+L-mode since the T+L-mode comes from the non-collinearity of the 120° structure. Although the spectrum of the well-defined excitation may contain the Higgs mode, it was not clearly separated from the T+L-mode. To clearly observe the Higgs mode, inelastic neutron scattering under pressure and magnetic field is proposed. For the continuum-like gapless excitation, the calculation cannot explain the cause of the continuum spectrum. Since only the one-magnon excitation was calculated in this study, consideration of further term such as two-magnon excitation is required for the future work. Furthermore, we proposed to investigate the spin spectrum of $RbFeCl_3$ in order to verify the collective excitation in the ordered phase more in detail.

## 5.2 $NaBa_2Mn_3F_{11}$

We have examined the magnetic structure and magnetic excitation in the Kagome antiferromagnet $NaBa_2Mn_3F_{11}$ by the powder neutron diffraction and inelastic neutron scattering. Anal-

ysis of the magnetic structure showed the multiple-$\boldsymbol{k}$ structure in which the 120° structure with a tail-chase geometry is realized with modulated IC structure. The classical calculation of the ground state in the Kagome-Triangular antiferromagnet including the magnetic dipole-dipole (MDD) interaction up to fourth neighboring paths was performed. The calculation exhibited that the MDD interaction solved the degeneracy of the ground state, and selected the tail-chase geometry 120° structure.

In the inelastic neutron scattering experiment, the spin wave excitation including the dispersive excitation and dispersionless excitation was observed. The calculated linear spin wave excitation including the nearest neighbor exchange interaction and MDD interaction semi-quantitatively reproduced the experimentally obtained spectrum. It was found that the energy position of the flat zero-energy excitation was quantitatively described by the MDD interaction. From observation of the zero-energy mode induced by the MDD interaction, it is concluded that $NaBa_2Mn_3F_{11}$ is a rare compound for the classical Kagome antiferromagnet having the MDD interaction. The measurement of thermodynamics such as thermal conductivity would be interesting for the future work since it is expected that the flat band excitation can be responsible for unusual thermodynamics and transport properties in general.

In this study, the origin of the multiple-$\boldsymbol{k}$ state including IC structure has not been identified. In addition, the linear spin wave excitation for the minimal model does not reproduce the experimental spectrum in detail. For the future work, detailed theoretical studies considering further interaction including the interlayer interaction and/or the long-range MDD interaction are required for understanding of the magnetic state in $NaBa_2Mn_3F_{11}$.

# Appendix A

# Linear spin wave theory on $CsFeCl_3$

In the work on magnetic excitation of $CsFeCl_3$, the magnetic excitation in the ordered phase was compared with the linear spin wave dispersion. We hereafter denote a spin wave dispersion based on the linear spin wave theory. The spin Hamiltonian of $CsFeCl_3$ is represented by

$$\begin{aligned}\mathcal{H} = &\sum_i \sum_{m_i} D\left(S^{z_0}_{m_i}\right)^2 + \sum_{i,j} \sum_{m_i,n_j} \left\{ J_\perp \left( S^{x_0}_{m_i} S^{x_0}_{n_j} + S^{y_0}_{m_i} S^{y_0}_{n_j} \right) + J_\parallel S^{z_0}_{m_i} S^{z_0}_{n_j} \right\} \\ &+ \sum_{i,j} \sum_{m_i,n_j} \left\{ J'_\perp \left( S^{x_0}_{m_i} S^{x_0}_{n_j} + S^{y_0}_{m_i} S^{y_0}_{n_j} \right) + J'_\parallel S^{z_0}_{m_i} S^{z_0}_{n_j} \right\}, \end{aligned} \tag{A.1}$$

where $x_0$, $y_0$ and $z_0$ represent a global coordinate and $m_i$ is the $i$-th sublattice in the $m$-th unit cell. $J_\perp$ and $J_\parallel$ are ferromagnetic intrachain interactions, and $J_\perp$ and $J_\parallel$ are antiferromagnetic in-plane interactions. $D$ is a single ion anisotropy and we set it positive to give an easy-plane anisotropy.

Since the magnetic structure is 120° structure with a magneic propagation vector $(1/3, 1/3, 0)$, three sublattices are considered. Considering the 120° structure, the global coordinate $(S^{x_0}_{m_i}, S^{y_0}_{m_i}, S^{z_0}_{m_i})$ is transformed to a local coordinate as follow:

$$\begin{cases} S^{x_0}_{m_i} = \cos\theta_i S^z_{m_i} + \sin\theta_i S^x_{m_i} \\ S^{y_0}_{m_i} = -\sin\theta_i S^z_{m_i} + \cos\theta_i S^x_{m_i} \\ S^{z_0}_{m_i} = S^y_{m_i} \end{cases}, \tag{A.2}$$

where $\theta_i$ are $0, \pm 2\pi/3$. From Holstein-Primakoff transformation, the spin operators are represented by

$$\begin{cases} S^z_{m_i} = S - a^\dagger_{m_i} a_{m_i} \\ S^x_{m_i} = \sqrt{\dfrac{S}{2}} \left( a^\dagger_{m_i} + a_{m_i} \right) \\ S^y_{m_i} = -\sqrt{\dfrac{S}{2}} i \left( a^\dagger_{m_i} - a_{m_i} \right) \end{cases},$$

where $a^\dagger_{m_i}$ and $a_{m_i}$ are bosonic creation-annihilation operators satisfying the commutation relation as

$$\left[ a_{m_i}, a^\dagger_{n_j} \right] = \delta(m_i - n_j). \tag{A.3}$$

Operator $a_{i,q}$ and $a^\dagger_{i,q}$ are introduced by the Fourier expansions:

$$\begin{cases} a_{m_i} = \dfrac{1}{\sqrt{N}} \displaystyle\sum_q e^{iq\cdot m_i} a_{i,q} \\ a^\dagger_{m_i} = \dfrac{1}{\sqrt{N}} \displaystyle\sum_q e^{-iq\cdot m_i} a^\dagger_{i,q} \end{cases}. \tag{A.4}$$

Using Eqs. (A.2), (A.3) and (A.4), the Hamiltonian Eq. (A.1) is represented. In the calculation, higher-order terms than the quadratic term of the bosonic operators are ignored for a linear approximation. Firstly, the single-ion anisotropy term is represented as follow:

$$\begin{aligned}
\sum_i \sum_{m_i} D\left(S^{z_0}_{m_i}\right)^2 &= \sum_i \sum_{m_i} D\left(S^{y}_{m_i}\right)^2 \\
&= -\frac{S}{2} \sum_i \sum_{m_i} D\left(a^\dagger_{m_i} - a_{m_i}\right)^2 \\
&= \frac{S}{2} \sum_i \sum_{m_i} D\left(a_{m_i} a^\dagger_{m_i} + a^\dagger_{m_i} a_{m_i} - a_{m_i} a_{m_i} - a^\dagger_{m_i} a^\dagger_{m_i}\right) \\
&= \frac{S}{2} \sum_i \sum_{m_i} D\left(2a^\dagger_{m_i} a_{m_i} + 1 - a_{m_i} a_{m_i} - a^\dagger_{m_i} a^\dagger_{m_i}\right) \\
&= \frac{S}{2} D N_{\mathrm{tot}} + \frac{S}{2}\frac{D}{N} \sum_i \sum_{m_i} \sum_{q,q'} \left[2a^\dagger_{i,q} a_{i,q'} e^{-i(q-q')\cdot m_i} - a_{i,q} a_{i,q'} e^{i(q+q')\cdot m_i} - h.c.\right] \\
&= \frac{S}{2} D N_{\mathrm{tot}} + \frac{S}{2} D \sum_i \sum_q \left[2a^\dagger_{i,q} a_{i,q} - a_{i,q} a_{i,-q} - h.c.\right] \qquad \text{(A.5)}
\end{aligned}$$

$N_{\mathrm{tot}}$ is the total number of the magnetic ion.

Next, intra-chain interaction is calculated as follow:

$$\begin{aligned}
&\sum_{i,j} \sum_{m_i,n_j} \left\{ J_\perp \left( S^{x_0}_{m_i} S^{x_0}_{n_j} + S^{y_0}_{m_i} S^{y_0}_{n_j} \right) + J_\parallel S^{z_0}_{m_i} S^{z_0}_{n_j} \right\} \\
&= \sum_{i,j} \sum_{m_i,n_j} \Big[ J_\perp \Big\{ (\cos\theta_i S^z_{m_i} + \sin\theta_i S^x_{m_i})(\cos\theta_j S^z_{n_j} + \sin\theta_j S^x_{n_j}) \\
&\quad + (-\sin\theta_i S^z_{m_i} + \cos\theta_i S^x_{m_i})(-\sin\theta_j S^z_{n_j} + \cos\theta_j S^x_{n_j}) \Big\} + J_\parallel S^y_{m_i} S^y_{n_j} \Big] \\
&= \sum_{i,j} \sum_{m_i,n_j} \left\{ J_\perp \cos(\theta_i - \theta_j) \left( S^z_{m_i} S^z_{n_j} + S^x_{m_i} S^x_{n_j} \right) + J_\parallel S^y_{m_i} S^y_{n_j} \right\},
\end{aligned}$$

where $\theta_i = \theta_j$ because the spins are ferromagnetic formed along the chain. Thus, the $\cos(\theta_i - \theta_j) = 1$ and we have

$$\sum_{i,j} \sum_{m_i,n_j} \left\{ J_\perp \left( S^z_{m_i} S^z_{n_j} + S^x_{m_i} S^x_{n_j} \right) + J_\parallel S^y_{m_i} S^y_{n_j} \right\}.$$

This equation is expressed by the bosonic operators as follow:

$$
\begin{aligned}
&\sum_{i,j}\sum_{m_i,n_j}\Bigg[J_\perp\Bigg\{(S-a^\dagger_{m_i}a_{m_i})(S-a^\dagger_{n_j}a_{n_j})+\frac{S}{2}(a^\dagger_{m_i}+a_{m_i})(a^\dagger_{n_j}+a_{n_j})\\
&-J_\parallel\frac{S}{2}(a^\dagger_{m_i}-a_{m_i})(a^\dagger_{n_j}-a_{n_j})\Bigg\}\Bigg]\\
&=\sum_{i,j}\sum_{m_i,n_j}\Bigg[J_\perp S^2-J_\perp S(a^\dagger_{m_i}a_{m_i}+a^\dagger_{n_j}a_{n_j})+\frac{S}{2}(J_\perp+J_\parallel)(a_{m_i}a^\dagger_{n_j}+a^\dagger_{m_i}a_{n_j})\\
&+\frac{S}{2}(J_\perp-J_\parallel)(a_{m_i}a_{n_j}+a^\dagger_{m_i}a^\dagger_{n_j})\Bigg]\\
&=J_\perp S^2N_{\rm tot}+\frac{S}{N}\sum_{i,j}\sum_{m_i,n_j}\sum_{q,q'}\Bigg[-2J_\perp a^\dagger_{i,q}a_{i,q'}e^{-i(q-q')\cdot m_i}\\
&+(J_\perp+J_\parallel)a^\dagger_{i,q}a_{j,q'}e^{-i(q-q')\cdot m_i}e^{-iq'\cdot(m_i-n_j)}\\
&+\frac{1}{2}(J_\perp-J_\parallel)\left\{a_{i,q}a_{j,q'}e^{i(q+q')\cdot m_i}e^{-iq'\cdot(m_i-n_j)}+h.c.\right\}\Bigg]\\
&=J_\perp S^2N_{\rm tot}+\sum_q\sum_{i,j}\sum_{\rho_{ij}}\Bigg[-2J_\perp Sa^\dagger_{i,q}a_{i,q}+S(J_\perp+J_\parallel)a^\dagger_{i,q}a_{j,q}e^{-iq\cdot\rho_{ij}}\\
&+\frac{S}{2}(J_\perp-J_\parallel)\left(a_{i,q}a_{j,-q}e^{-iq\cdot\rho_{ij}}+h.c.\right)\Bigg]\\
&=J_\perp S^2N_{\rm tot}+\sum_q\sum_{i}\sum_{\rho_{ii}}\Bigg[-2J_\perp Sa^\dagger_{i,q}a_{i,q}+S(J_\perp+J_\parallel)a^\dagger_{i,q}a_{i,q}e^{-iq\cdot\rho_{ii}}\\
&+\frac{S}{2}(J_\perp-J_\parallel)\left(a_{i,q}a_{i,-q}e^{-iq\cdot\rho_{ii}}+h.c.\right)\Bigg],
\end{aligned}
\tag{A.6}
$$

where $\rho_{ii}$ is a bond vector of the nearest neighbor interaction along the chain.

When a lattice unit vector $\boldsymbol{a},\boldsymbol{b},\boldsymbol{c}$ is used, the bond vector is given by $\pm\boldsymbol{c}/2$. Hence the sum of $\rho_{ii}$ is given by

$$
f(\boldsymbol{q})=\sum_{\rho_{ii}}e^{-iq\cdot\rho_{ii}}=2\cos(\pi l),
\tag{A.7}
$$

where wave vector $\boldsymbol{q}$ is defined as a reciprocal lattice unit vector $h\boldsymbol{a}^*+k\boldsymbol{b}^*+l\boldsymbol{c}^*$. Then the intra-chain interaction is represented by

$$
\begin{aligned}
&J_\perp S^2N_{\rm tot}+\sum_q\sum_i\Bigg[-4J_\perp Sa^\dagger_{i,q}a_{i,q}+S(J_\perp+J_\parallel)f(\boldsymbol{q})a^\dagger_{i,q}a_{i,q}\\
&+\frac{S}{2}(J_\perp-J_\parallel)\left(a_{i,q}a_{i,-q}f(\boldsymbol{q})+h.c.\right)\Bigg].
\end{aligned}
\tag{A.8}
$$

Similary, the inter-chain interaction term is represented by

$$
\begin{aligned}
&\sum_{i,j}\sum_{m_i,n_j}\left\{J'_\perp\left(S^{x_0}_{m_i}S^{x_0}_{n_j}+S^{y_0}_{m_i}S^{y_0}_{n_j}\right)+J'_\parallel S^{z_0}_{m_i}S^{z_0}_{n_j}\right\}\\
&=\sum_{i,j}\sum_{m_i,n_j}\Bigg[J'_\perp\Bigg\{(\cos\theta_iS^z_{m_i}+\sin\theta_iS^x_{m_i})(\cos\theta_jS^z_{n_j}+\sin\theta_jS^x_{n_j})\\
&+(-\sin\theta_iS^z_{m_i}+\cos\theta_iS^x_{m_i})(-\sin\theta_jS^z_{n_j}+\cos\theta_jS^x_{n_j})\Bigg\}+J'_\parallel S^y_{m_i}S^y_{n_j}\Bigg]\\
&=\sum_{i,j}\sum_{m_i,n_j}\left\{J'_\perp\cos(\theta_i-\theta_j)\left(S^z_{m_i}S^z_{n_j}+S^x_{m_i}S^x_{n_j}\right)+J'_\parallel S^y_{m_i}S^y_{n_j}\right\}.
\end{aligned}
$$

Since the magnetic structure is the 120° structure, the spin configuration of the nearest neighbor bond is $\theta_i - \theta_j = \pm 2\pi/3$. Thus, $\cos(\theta_i - \theta_j) = -1/2$ and we have

$$\sum_{i,j}\sum_{m_i,n_j}\left\{-\frac{1}{2}J'_\perp\left(S^z_{m_i}S^z_{n_j}+S^x_{m_i}S^x_{n_j}\right)+J'_\parallel S^y_{m_i}S^y_{n_j}\right\}. \tag{A.9}$$

This equation is expressed by the bosonic operators as follow:

$$\begin{aligned}
&\sum_{i,j}\sum_{m_i,n_j}\left[-J'_\perp\frac{S^2}{2}+J'_\perp\frac{S}{2}(a^\dagger_{m_i}a_{m_i}+a^\dagger_{n_j}a_{n_j})+\frac{S}{2}\left(-\frac{1}{2}J'_\perp+J'_\parallel\right)(a_{m_i}a^\dagger_{n_j}+a^\dagger_{m_i}a_{n_j})\right.\\
&\left.+\frac{S}{2}\left(-\frac{1}{2}J'_\perp-J'_\parallel\right)(a_{m_i}a_{n_j}+a^\dagger_{m_i}a^\dagger_{n_j})\right]\\
&=-J'_\perp\frac{S^2}{2}N_{\rm tot}+\frac{S}{N}\sum_{i,j}\sum_{m_i,n_j}\sum_{q,q'}\left[J'_\perp a^\dagger_{i,q}a_{i,q'}e^{-i(q-q')\cdot m_i}\right.\\
&+\left(-\frac{1}{2}J'_\perp+J'_\parallel\right)a^\dagger_{i,q}a_{j,q'}e^{-i(q-q')\cdot m_i}e^{-iq'\cdot(m_i-n_j)}\\
&\left.+\frac{1}{2}\left(-\frac{1}{2}J'_\perp-J'_\parallel\right)\left\{a_{i,q}a_{j,q'}e^{i(q+q')\cdot m_i}e^{-iq'\cdot(m_i-n_j)}+h.c.\right\}\right]\\
&=-J'_\perp\frac{S^2}{2}N_{\rm tot}+\sum_q\sum_{i,j}\sum_{\rho_{ij}}\left[J'_\perp Sa^\dagger_{i,q}a_{i,q}+S\left(-\frac{1}{2}J'_\perp+J'_\parallel\right)a^\dagger_{i,q}a_{j,q}e^{-iq\cdot\rho_{ij}}\right.\\
&\left.+\frac{S}{2}\left(-\frac{1}{2}J'_\perp-J'_\parallel\right)\left(a_{i,q}a_{j,-q}e^{-iq\cdot\rho_{ij}}+h.c.\right)\right],
\end{aligned}\tag{A.10}$$

where $\rho_{ij}$ is a bond vector of the nearest neighbor inter-chain interaction.

The bond vectors are given by $\boldsymbol{a}, \boldsymbol{b}, \boldsymbol{a}+\boldsymbol{b}$. Hence the sums of $\rho_{12}$, $\rho_{23}$ and $\rho_{31}$ are represented by

$$\begin{aligned}
g(\boldsymbol{q}) &= \sum_{\rho_{12}}e^{-iq\cdot\rho_{12}}=\sum_{\rho_{23}}e^{-iq\cdot\rho_{23}}=\sum_{\rho_{31}}e^{-iq\cdot\rho_{31}}\\
&= \exp(-2\pi ih)+\exp(-2\pi ik)+\exp(-2\pi i(h+k)).
\end{aligned}\tag{A.11}$$

Then the intra-chain interaction is represented by

$$\begin{aligned}
&-J'_\perp\frac{S^2}{2}N_{\rm tot}+\sum_q\sum_{i,j}\left[3J'_\perp Sa^\dagger_{i,q}a_{i,q}+S\left(-\frac{1}{2}J'_\perp+J'_\parallel\right)g(\boldsymbol{q})a^\dagger_{i,q}a_{j,q}e^{-iq\cdot\rho_{ij}}\right.\\
&\left.+\frac{S}{2}\left(-\frac{1}{2}J'_\perp-J'_\parallel\right)(a_{i,q}a_{j,-q}g(\boldsymbol{q})+h.c.)\right].
\end{aligned}\tag{A.12}$$

The Hamiltonian Eq. (A.1) is represented as follow:

$$\begin{aligned}
\mathcal{H}=&\left(\frac{S}{2}D+S^2J_\perp-\frac{S^2}{2}J'_\perp\right)N_{\rm tot}+\sum_q S\left[\sum_{i,j}\left\{\left(D-2J_\perp+(J_\perp+J_\parallel)f(\boldsymbol{q})\right)\delta_{ij}\right.\right.\\
&\left.+\left(3J'_\perp\delta_{ij}+\left(-\frac{1}{2}J'_\perp+J'_\parallel\right)g(\boldsymbol{q})(1-\delta_{ij})\right)\right\}a^\dagger_{i,q}a_{j,q}\\
&+\frac{1}{2}\sum_{i,j}\left\{\left(-D+(J_\perp-J_\parallel)f(\boldsymbol{q})\right)\delta_{ij}\right.\\
&\left.\left.+(1-\delta_{ij})\left(-\frac{1}{2}J'_\perp-J'_\parallel\right)g(\boldsymbol{q})\right\}a_{i,q}a_{j,-q}+h.c.\right].
\end{aligned}\tag{A.13}$$

The only second term with $q$-depedence exhibits the spin wave excitation. When the constant terms are ignored and $3\times3$ matrices $\boldsymbol{A}(\boldsymbol{q})$ and $\boldsymbol{B}(\boldsymbol{q})$ are introdued, the Hamiltonian is represented by

$$\mathcal{H} = \sum_{\boldsymbol{q}} \left\{ \sum_{i,j} A_{i,j}(\boldsymbol{q}) a_i^\dagger(\boldsymbol{q}) a_j(\boldsymbol{q}) + \frac{1}{2} \sum_{i,j} \left[ B_{i,j}(\boldsymbol{q}) a_i^\dagger(\boldsymbol{q}) a_j^\dagger(-\boldsymbol{q}) + h.c. \right] \right\}. \tag{A.14}$$

In general, the eigenvalue equation of this Hamiltonian is given by

$$(\boldsymbol{A}+\boldsymbol{B})(\boldsymbol{A}-\boldsymbol{B})\,\chi_\tau(\boldsymbol{q}) = \omega(\boldsymbol{q})^2 \chi_\tau(\boldsymbol{q}). \tag{A.15}$$

Diagonalizing $(\boldsymbol{A}+\boldsymbol{B})(\boldsymbol{A}-\boldsymbol{B})$, energy dispersions $\omega(\boldsymbol{q})$ are obtained, and $\tau$ indicates a label of the nomal mode. In this calculation, since the three sublattices are considered, three spin wave dispersions are obtained.

# Acknowledgements

First and foremost I would like to thank my supervisor, Prof. Takatsugu Masuda for his good advice and insight throughout my graduate studies. He has provided me with important things to advance the research, and demonstrated various experimental techniques, especially neutron scattering technique. I am indebted to him for dedicating so much his time to answering my questions and discussion on this study. Furthermore, I would like to appreciate him giving me precious opportunities such as going abroad for experiments and attending conferences.

I would like to thank all collaborators for their kind supports, helpful suggestions, and fruitful discussions. I am grateful to Dr. Minoru Soda who supported the neutron scattering experiments and gave me many fruitful suggestions for my research. He taught me how to perform neutron scattering experiment and analyze the data. I am grateful to Dr. Masato Hagihala who supported the pressure experiment on $CsFeCl_3$ at CTAX in ORNL and discussed the ground state of $NaBa_3Mn_3F_{11}$. I wish to thank Dr. Oksana Zaharko who supported the neutron diffraction experiment on $CsFeCl_3$ at ZEBRA diffractometer in PSI, and Dr. Tao Hong who supported the inelastic neutron scattering experiment on $CsFeCl_3$ at CTAX spectrometer in ORNL. I wish to thank Dr. Maxim Avdeev who supported the powder neutron diffraction experiment on $NaBa_2Mn_3F_{11}$ at ECHIDNA diffractometer in ANSTO, and Dr. Manuel Pascal who supported the powder neutron diffraction experiment on $NaBa_2Mn_3F_{11}$ at WISH diffractometer in ISIS. I wish to thank Dr. Hannu Mutka and Dr. Gøran J. Nilsen who supported the powder inelastic neutron scattering experiments on $NaBa_2Mn_3F_{11}$ at IN4C and IN6 spectrometers in ILL. I would like to thank Prof. Shinichi Itoh and Prof. Tetsuya Yokoo for supporting the inelastic neutron scattering experiment at HRC in J-PARC/MLF.

I wish to thank Dr. Nobuyuki Kurita and Prof. Hidekazu Tanaka for providing the high quality single crystal sample of $CsFeCl_3$. I wish to thank Dr. Hajime Ishikawa, Prof. Yoshihiko Okamoto and Prof. Zenji Hiroi for providing the high quality powder sample of $NaBa_2Mn_3F_{11}$.

I would like to thank Prof. Yoshiya Uwatoko for preparation of pressure cell and supporting pressure experiment on $CsFeCl_3$. I would like to thank Dr. Denis Cheptiakov and Dr. Jonathan White for supporting the pressure experiment on $CsFeCl_3$ at ZEBRA in PSI.

I am grateful to Prof. Masashige Matsumoto who calculated the spin wave excitation and discussed collective excitation of $CsFeCl_3$. I would like to thank Dr. Tsuyoshi Okubo for discussion on the magnetic order and magnetic excitation in $NaBa_2Mn_3F_{11}$.

I would like to thank Dr. Shinichiro Asai for giving me suggestions and fruitful comments to my research work. I would like to thank Dr. Daichi Kawana, Mr. Toshio Asami, and Mr. Ryosuke Sugiura for technical support of the neutron scattering experiment. I would like to appreciate Prof. Henrik M. Rønnow giving me many good suggestions and permitting my visit to EPFL. I am grateful to Dr. Yu Tanaka and Mr. Ryutaro Okuma for fruitful discussions on the Kagome antiferromagnet. I am grateful to Dr. Tendai Haku, Mr. Yuki Honma, Mr. Takuya Oyama, Mr. Toshiya Yoshida, Mr. Shinsuke Iida, Mr. Daiki Kato, Mr. Hodaka Kikuchi, and Mr. Shunsuke Hasegawa for their cooperations in research life, Masuda group. I would like to thank Ms. Ayako Ohgushi, Ms. Naomi Habu, Ms. Tomoko Iidaka, and Ms. Junko Itoh for supporting my research activity.

This project was essentially based on experiments at large scale facilities. I am thankful for all the assistance I received from many staffs for the instruments and sample environments at PSI, ORNL, ANSTO, ISIS, ILL, and J-PARC/MLF.

I would like to appreciate the support by the Japan Society for the Promotion of Science through the Leading Graduate Schools (MERIT).

Lastly, I want to thank my parents and family, and all the people who have supported me.

# Bibliography


[1] S. Sachdev, *Quantum Phase Transitions* (Cambridge University Press, 2007).
[2] S. Sachdev, Science **288**, 475 (2000).
[3] M. Vojta, Reports on Progress in Physics **66**, 2069 (2003).
[4] D. Bitko, T. F. Rosenbaum, and G. Aeppli, Phys. Rev. Lett. **77**, 940 (1996).
[5] H. M. Rønnow, R. Parthasarathy, J. Jensen, G. Aeppli, T. F. Rosenbaum, and D. F. McMorrow, Science **308**, 389 (2005).
[6] E. Dagotto, Rev. Mod. Phys. **66**, 763 (1994).
[7] J. Orenstein and A. J. Millis, Science **288**, 468 (2000).
[8] J. Paglione and R. L. Greene, Nature Physics **6**, 645 EP (2010), Review Article.
[9] T. Shibauchi, A. Carrington, and Y. Matsuda, Annual Review of Condensed Matter Physics **5**, 113 (2014).
[10] P. Gegenwart, Q. Si, and F. Steglich, Nature Physics **4**, 186 (2008).
[11] Q. Si and F. Steglich, Science **329**, 1161 (2010).
[12] B. Spivak, S. V. Kravchenko, S. A. Kivelson, and X. P. A. Gao, Rev. Mod. Phys. **82**, 1743 (2010).
[13] M. Greiner, O. Mandel, T. Esslinger, T. W. Hänsch, and I. Bloch, Nature **415**, 39 (2002).
[14] I. Bloch, J. Dalibard, and W. Zwerger, Rev. Mod. Phys. **80**, 885 (2008).
[15] D. Pekker and C. Varma, Annual Review of Condensed Matter Physics **6**, 269 (2015).
[16] F. Englert and R. Brout, Phys. Rev. Lett. **13**, 321 (1964).
[17] P. W. Higgs, Phys. Rev. Lett. **13**, 508 (1964).
[18] Y. Nambu, Phys. Rev. Lett. **4**, 380 (1960).
[19] Y. Nambu and G. Jona-Lasinio, Phys. Rev. **122**, 345 (1961).
[20] Y. Nambu and G. Jona-Lasinio, Phys. Rev. **124**, 246 (1961).
[21] R. Sooryakumar and M. V. Klein, Phys. Rev. Lett. **45**, 660 (1980).
[22] P. B. Littlewood and C. M. Varma, Phys. Rev. B **26**, 4883 (1982).
[23] R. Matsunaga, N. Tsuji, H. Fujita, A. Sugioka, K. Makise, Y. Uzawa, H. Terai, Z. Wang, H. Aoki, and R. Shimano, Science **345**, 1145 (2014).
[24] J. C. Tsang, J. E. Smith, and M. W. Shafer, Phys. Rev. Lett. **37**, 1407 (1976).
[25] J. P. Pouget, B. Hennion, C. Escribe-Filippini, and M. Sato, Phys. Rev. B **43**, 8421 (1991).
[26] M. Endres, T. Fukuhara, D. Pekker, M. Cheneau, P. Schaub, C. Gross, E. Demler, S. Kuhr, and I. Bloch, Nature **487**, 454 (2012).
[27] C. Rüegg, B. Normand, M. Matsumoto, A. Furrer, D. F. McMorrow, K. W. Krämer, H. U. Güdel, S. N. Gvasaliya, H. Mutka, and M. Boehm, Phys. Rev. Lett. **100**, 205701 (2008).
[28] P. Merchant, B. Normand, K. W. Kramer, M. Boehm, D. F. McMorrow, and C. Ruegg, Nat Phys **10**, 373 (2014).
[29] B. Grenier, S. Petit, V. Simonet, E. Canévet, L.-P. Regnault, S. Raymond, B. Canals, C. Berthier, and P. Lejay, Phys. Rev. Lett. **114**, 017201 (2015).
[30] A. Jain, M. Krautloher, J. Porras, G. H. Ryu, D. P. Chen, D. L. Abernathy, J. T. Park, A. Ivanov, J. Chaloupka, G. Khaliullin, B. Keimer, and B. J. Kim, Nature Physics **13**, 633 (2017).
[31] T. Hong, M. Matsumoto, Y. Qiu, W. Chen, T. R. Gentile, S. Watson, F. F. Awwadi, M. M. Turnbull, S. E. Dissanayake, H. Agrawal, R. Toft-Petersen, B. Klemke, K. Coester, K. P. Schmidt, and D. A. Tennant, Nature Physics **13**, 638 (2017).

[32] S. Sachdev and R. N. Bhatt, Phys. Rev. B **41**, 9323 (1990).
[33] K. Takatsu, W. Shiramura, and H. Tanaka, J. Phys. Soc. Jpn. **66**, 1611 (1997).
[34] W. Shiramura, K. Takatsu, H. Tanaka, K. Kamishima, M. Takahashi, H. Mitamura, and T. Goto, J. Phys. Soc. Jpn. **66**, 1900 (1997).
[35] A. Oosawa, M. Ishii, and H. Tanaka, Journal of Physics: Condensed Matter **11**, 265 (1999).
[36] A. Oosawa, H. A. Katori, and H. Tanaka, Phys. Rev. B **63**, 134416 (2001).
[37] H. Tanaka, A. Oosawa, T. Kato, H. Uekusa, Y. Ohashi, K. Kakurai, and A. Hoser, J. Phys. Soc. Jpn. **70**, 939 (2001).
[38] A. Oosawa, M. Fujisawa, T. Osakabe, K. Kakurai, and H. Tanaka, J. Phys. Soc. Jpn. **72**, 1026 (2003).
[39] K. Goto, M. Fujisawa, T. Ono, H. Tanaka, and Y. Uwatoko, J. Phys. Soc. Jpn. **73**, 3254 (2004).
[40] C. Rüegg, A. Furrer, D. Sheptyakov, T. Strässle, K. W. Krämer, H.-U. Güdel, and L. Mélési, Phys. Rev. Lett. **93**, 257201 (2004).
[41] T. Nikuni, M. Oshikawa, A. Oosawa, and H. Tanaka, Phys. Rev. Lett. **84**, 5868 (2000).
[42] M. Matsumoto, B. Normand, T. M. Rice, and M. Sigrist, Phys. Rev. B **69**, 054423 (2004).
[43] A. Khudoyberdiev, A. Rakhimov, and A. Schilling, New Journal of Physics **19**, 113002 (2017).
[44] Y. Kulik and O. P. Sushkov, Phys. Rev. B **84**, 134418 (2011).
[45] Y. Q. Qin, B. Normand, A. W. Sandvik, and Z. Y. Meng, Phys. Rev. Lett. **118**, 147207 (2017).
[46] J. Oitmaa, Y. Kulik, and O. P. Sushkov, Phys. Rev. B **85**, 144431 (2012).
[47] S. Jin and A. W. Sandvik, Phys. Rev. B **85**, 020409 (2012).
[48] M. Kao and F. Jiang, The European Physical Journal B **86**, 419 (2013).
[49] D.-R. Tan and F.-J. Jiang, Phys. Rev. B **95**, 054435 (2017).
[50] H. D. Scammell and O. P. Sushkov, Phys. Rev. B **95**, 094410 (2017).
[51] M. Matsumoto, J. Phys. Soc. Jpn. **83**, 084704 (2014).
[52] Z. Wang, A. E. Feiguin, W. Zhu, O. A. Starykh, A. V. Chubukov, and C. D. Batista, Phys. Rev. B **96**, 184409 (2017).
[53] T. Kato, K. Takatsu, H. Tanaka, W. Shiramura, M. Mori, K. Nakajima, and K. Kakurai, J. Phys. Soc. Jpn. **67**, 752 (1998).
[54] I. A. Zaliznyak, S.-H. Lee, and S. V. Petrov, Phys. Rev. Lett. **87**, 017202 (2001).
[55] H. Nojiri, Y. Tokunaga, and M. Motokawa, Le Journal de Physique Colloques **49**, C8 (1988).
[56] H. Yoshizawa and K. Hirakawa, J. Phys. Soc. Jpn. **46**, 448 (1979).
[57] K. Hirakawa and H. Yoshizawa, J. Phys. Soc. Jpn. **46**, 455 (1979).
[58] H. Yoshizawa, W. Kozukue, and K. Hirakawa, J. Phys. Soc. Jpn. **49**, 144 (1980).
[59] H. J. Seifert and K. Klatyk, Z. Anorg. Allg. Chem. **342**, 1 (1966).
[60] M. Steiner, K. Kakurai, W. Knop, B. Dorner, R. Pynn, U. Happek, P. Day, and G. McLeen, Solid State Communications **38**, 1179 (1981).
[61] K. Inomata and T. Oguchi, J. Phys. Soc. Jpn. **23**, 765 (1967).
[62] N. Kurita and H. Tanaka, Phys. Rev. B **94**, 104409 (2016).
[63] T. Haseda, N. Wada, M. Hata, and K. Amaya, Physica B+C **108**, 841 (1981).
[64] J. A. Baines, C. E. Johnson, and M. F. Thomas, Journal of Physics C: Solid State Physics **16**, 3579 (1983).
[65] M. Chiba, T. Tsuboi, H. Hori, I. Shiozaki, and M. Date, Solid State Communications **63**, 427 (1987).
[66] M. Chiba, Y. Ajiro, K. Adachi, and T. Morimoto, J. Phys. Soc. Jpn. **57**, 3178 (1988).
[67] M. Toda, Y. Fujii, S. Kawano, T. Goto, M. Chiba, S. Ueda, K. Nakajima, K. Kakurai, J. Klenke, R. Feyerherm, M. Meschke, H. A. Graf, and M. Steiner, Phys. Rev. B **71**, 224426 (2005).
[68] G. H. Wannier, Phys. Rev. **79**, 357 (1950).

[69] C. Lacroix, P. Mendels, and F. Mila, *Introduction to Frustrated Magnetism: Materials, Experiments, Theory* (Springer, 2011).
[70] H. Diep, *Frustrated Spin Systems (2nd Edition)* (World Scientific Publishing Company, 2013).
[71] L. Balents, Nature **464**, 199 (2010).
[72] A. Yoshimori, J. Phys. Soc. Jpn. **14**, 807 (1959).
[73] J. Villain, Journal of Physics and Chemistry of Solids **11**, 303 (1959).
[74] T. A. Kaplan, Phys. Rev. **116**, 888 (1959).
[75] S.-W. Cheong and M. Mostovoy, Nature Materials **6**, 13 (2007).
[76] K. Kano and S. Naya, Progress of Theoretical Physics **10**, 158 (1953).
[77] P. Anderson, Materials Research Bulletin **8**, 153 (1973).
[78] P. Lecheminant, B. Bernu, C. Lhuillier, L. Pierre, and P. Sindzingre, Phys. Rev. B **56**, 2521 (1997).
[79] M. A. de Vries, J. R. Stewart, P. P. Deen, J. O. Piatek, G. J. Nilsen, H. M. Rønnow, and A. Harrison, Phys. Rev. Lett. **103**, 237201 (2009).
[80] T.-H. Han, J. S. Helton, S. Chu, D. G. Nocera, J. A. Rodriguez-Rivera, C. Broholm, and Y. S. Lee, Nature **492**, 406 (2012).
[81] H. Ishikawa, M. Yoshida, K. Nawa, M. Jeong, S. Krämer, M. Horvatić, C. Berthier, M. Takigawa, M. Akaki, A. Miyake, M. Tokunaga, K. Kindo, J. Yamaura, Y. Okamoto, and Z. Hiroi, Phys. Rev. Lett. **114**, 227202 (2015).
[82] M. Yoshida, K. Nawa, H. Ishikawa, M. Takigawa, M. Jeong, S. Krämer, M. Horvatić, C. Berthier, K. Matsui, T. Goto, S. Kimura, T. Sasaki, J. Yamaura, H. Yoshida, Y. Okamoto, and Z. Hiroi, Phys. Rev. B **96**, 180413 (2017).
[83] B. Fåk, E. Kermarrec, L. Messio, B. Bernu, C. Lhuillier, F. Bert, P. Mendels, B. Koteswararao, F. Bouquet, J. Ollivier, A. D. Hillier, A. Amato, R. H. Colman, and A. S. Wills, Phys. Rev. Lett. **109**, 037208 (2012).
[84] M. R. Norman, Rev. Mod. Phys. **88**, 041002 (2016).
[85] J. N. Reimers and A. J. Berlinsky, Phys. Rev. B **48**, 9539 (1993).
[86] M. Elhajal, B. Canals, and C. Lacroix, Phys. Rev. B **66**, 014422 (2002).
[87] M. Maksymenko, V. R. Chandra, and R. Moessner, Phys. Rev. B **91**, 184407 (2015).
[88] J.-C. Domenge, P. Sindzingre, C. Lhuillier, and L. Pierre, Phys. Rev. B **72**, 024433 (2005).
[89] T. Inami, M. Nishiyama, S. Maegawa, and Y. Oka, Phys. Rev. B **61**, 12181 (2000).
[90] A. S. Wills, Phys. Rev. B **63**, 064430 (2001).
[91] A. S. Wills, A. Harrison, C. Ritter, and R. I. Smith, Phys. Rev. B **61**, 6156 (2000).
[92] D. Grohol, D. G. Nocera, and D. Papoutsakis, Phys. Rev. B **67**, 064401 (2003).
[93] T. Inami, T. Morimoto, M. Nishiyama, S. Maegawa, Y. Oka, and H. Okumura, Phys. Rev. B **64**, 054421 (2001).
[94] A. Scheie, M. Sanders, J. Krizan, Y. Qiu, R. J. Cava, and C. Broholm, Phys. Rev. B **93**, 180407 (2016).
[95] S. T. T. Nagamiya and Y. Yamaguchi, Solid State Commun. **42**, 385 (1982).
[96] D. P. Kozlenko, A. F. Kusmartseva, E. V. Lukin, D. A. Keen, W. G. Marshall, M. A. de Vries, and K. V. Kamenev, Phys. Rev. Lett. **108**, 187207 (2012).
[97] E. Lhotel, V. Simonet, J. Ortloff, B. Canals, C. Paulsen, E. Suard, T. Hansen, D. J. Price, P. T. Wood, A. K. Powell, and R. Ballou, Phys. Rev. Lett. **107**, 257205 (2011).
[98] E. Lhotel, V. Simonet, J. Ortloff, B. Canals, C. Paulsen, E. Suard, T. Hansen, D. Price, P. Wood, A. Powell, and R. Ballou, The European Physical Journal B **86**, 248 (2013).
[99] J. T. Chalker, P. C. W. Holdsworth, and E. F. Shender, Phys. Rev. Lett. **68**, 855 (1992).
[100] K. Matan, D. Grohol, D. G. Nocera, T. Yildirim, A. B. Harris, S. H. Lee, S. E. Nagler, and Y. S. Lee, Phys. Rev. Lett. **96**, 247201 (2006).
[101] M. Maksymenko, R. Moessner, and K. Shtengel, Phys. Rev. B **96**, 134411 (2017).
[102] S. A. Parameswaran, R. Roy, and S. L. Sondhi, Comptes Rendus Physique **14**, 816 (2013).
[103] E. J. Bergholtz and Z. Liu, International Journal of Modern Physics B **27**, 1330017 (2013).

[104] O. Derzhko, J. Richter, and M. Maksymenko, International Journal of Modern Physics B **29**, 1530007 (2015).
[105] E. Tang, J.-W. Mei, and X.-G. Wen, Phys. Rev. Lett. **106**, 236802 (2011).
[106] K. Sun, Z. Gu, H. Katsura, and S. Das Sarma, Phys. Rev. Lett. **106**, 236803 (2011).
[107] T. Neupert, L. Santos, C. Chamon, and C. Mudry, Phys. Rev. Lett. **106**, 236804 (2011).
[108] R. Chisnell, J. S. Helton, D. E. Freedman, D. K. Singh, R. I. Bewley, D. G. Nocera, and Y. S. Lee, Phys. Rev. Lett. **115**, 147201 (2015).
[109] L. Zhang, J. Ren, J.-S. Wang, and B. Li, Phys. Rev. B **87**, 144101 (2013).
[110] K. Ohgushi, S. Murakami, and N. Nagaosa, Phys. Rev. B **62**, R6065 (2000).
[111] T. Ideue, Y. Onose, H. Katsura, Y. Shiomi, S. Ishiwata, N. Nagaosa, and Y. Tokura, Phys. Rev. B **85**, 134411 (2012).
[112] D. L. Bergman, C. Wu, and L. Balents, Phys. Rev. B **78**, 125104 (2008).
[113] J. Darriet, M. Ducau, M. Feist, A. Tressaud, and P. Hagenmuller, Journal of Solid State Chemistry **98**, 379 (1992).
[114] H. Ishikawa, T. Okubo, Y. Okamoto, and Z. Hiroi, J. Phys. Soc. Jpn. **83**, 043703 (2014).
[115] J. B. Goodenough, Phys. Rev. **100**, 564 (1955).
[116] J. Kanamori, Journal of Physics and Chemistry of Solids **10**, 87 (1959).
[117] G. L. Squires, *Introduction to the theory of thermal neutron scattering* (Cambridge University Press, 2012).
[118] S. Lovesey, *Theory of neutron scattering from condensed matter* (Oxford University Press, 1984).
[119] C. G. Shull and J. S. Smart, Phys. Rev. **76**, 1256 (1949).
[120] B. N. Brockhouse, Phys. Rev. **106**, 859 (1957).
[121] P. Brown, International tables for crystallography **100** (1992).
[122] B. T. M. Willis and C. J. Carlile, *Experimental neutron scattering* (Oxford University Press, 2017).
[123] K.-D. Liss, B. Hunter, M. Hagen, T. Noakes, and S. Kennedy, Physica B: Condensed Matter **385**, 1010 (2006).
[124] L. C. Chapon, P. Manuel, P. G. Radaelli, C. Benson, L. Perrott, S. Ansell, N. J. Rhodes, D. Raspino, D. Duxbury, E. Spill, and J. Norris, Neutron News **22**, 22 (2011).
[125] S. Itoh, T. Yokoo, S. Satoh, S. Yano, D. Kawana, J. Suzuki, and T. J. Sato, Nuclear Instruments and Methods in Physics Research Section A: Accelerators, Spectrometers, Detectors and Associated Equipment **631**, 90 (2011).
[126] S. Yano, S. Itoh, S. Satoh, T. Yokoo, D. Kawana, and T. J. Sato, Nuclear Instruments and Methods in Physics Research Section A: Accelerators, Spectrometers, Detectors and Associated Equipment **654**, 421 (2011).
[127] S. Itoh, T. Yokoo, D. Kawana, H. Yoshizawa, T. Masuda, M. Soda, T. J. Sato, S. Satoh, M. Sakaguchi, and S. Muto, J. Phys. Soc. Jpn. **82**, SA033 (2013).
[128] A. Wills, Physica B: Condensed Matter **276**, 680 (2000).
[129] J. Rodriguez-Carvajal, Physica B: Condensed Matter **192**, 55 (1993).
[130] H. Nakao, M. Nishi, Y. Fujii, T. Masuda, I. Tsukada, K. Uchinokura, K. Hirota, and G. Shirane, J. Phys. Soc. Jpn. **68**, 3662 (1999).
[131] Y. J. Wang, V. Kiryukhin, R. J. Birgeneau, T. Masuda, I. Tsukada, and K. Uchinokura, Phys. Rev. Lett. **83**, 1676 (1999).
[132] D. M. Pajerowski, C. R. Rotundu, J. W. Lynn, and R. J. Birgeneau, Phys. Rev. B **87**, 134507 (2013).
[133] M. G. Kim, M. Wang, G. S. Tucker, P. N. Valdivia, D. L. Abernathy, S. Chi, A. D. Christianson, A. A. Aczel, T. Hong, T. W. Heitmann, S. Ran, P. C. Canfield, E. D. Bourret-Courchesne, A. Kreyssig, D. H. Lee, A. I. Goldman, R. J. McQueeney, and R. J. Birgeneau, Phys. Rev. B **92**, 214404 (2015).
[134] H. Kawamura, J. Phys. Soc. Jpn. **61**, 1299 (1992).
[135] H. Kawamura, Journal of Physics: Condensed Matter **10**, 4707 (1998).

[136] Y. Ajiro, T. Nakashima, Y. Unno, H. Kadowaki, M. Mekata, and N. Achiwa, J. Phys. Soc. Jpn. **57**, 2648 (1988).
[137] U. Schotte, N. Stusser, K. D. Schotte, H. Weinfurter, H. M. Mayer, and M. Winkelmann, Journal of Physics: Condensed Matter **6**, 10105 (1994).
[138] M. Enderle, R. Schneider, Y. Matsuoka, and K. Kakurai, Physica B: Condensed Matter **234-236**, 554 (1997).
[139] A. V. Chubukov and O. A. Starykh, Phys. Rev. Lett. **110**, 217210 (2013).
[140] E. Parker and L. Balents, Phys. Rev. B **95**, 104411 (2017).
[141] S. Miyashita and H. Shiba, J. Phys. Soc. Jpn. **53**, 1145 (1984).
[142] A. O. Sorokin and A. V. Syromyatnikov, Phys. Rev. B **85**, 174404 (2012).
[143] T. Okubo and H. Kawamura, Phys. Rev. B **82**, 014404 (2010).
[144] M. L. Plumer, H. Kawamura, and A. Caillé, Phys. Rev. B **43**, 13786 (1991).
[145] H. Katsura, N. Nagaosa, and A. V. Balatsky, Phys. Rev. Lett. **95**, 057205 (2005).
[146] I. A. Sergienko and E. Dagotto, Phys. Rev. B **73**, 094434 (2006).
[147] M. Mostovoy, Phys. Rev. Lett. **96**, 067601 (2006).
[148] M. Kenzelmann, G. Lawes, A. B. Harris, G. Gasparovic, C. Broholm, A. P. Ramirez, G. A. Jorge, M. Jaime, S. Park, Q. Huang, A. Y. Shapiro, and L. A. Demianets, Phys. Rev. Lett. **98**, 267205 (2007).
[149] A. J. Hearmon, F. Fabrizi, L. C. Chapon, R. D. Johnson, D. Prabhakaran, S. V. Streltsov, P. J. Brown, and P. G. Radaelli, Phys. Rev. Lett. **108**, 237201 (2012).
[150] H. Mitamura, R. Watanuki, K. Kaneko, N. Onozaki, Y. Amou, S. Kittaka, R. Kobayashi, Y. Shimura, I. Yamamoto, K. Suzuki, S. Chi, and T. Sakakibara, Phys. Rev. Lett. **113**, 147202 (2014).
[151] R. Coldea, D. A. Tennant, A. M. Tsvelik, and Z. Tylczynski, Phys. Rev. Lett. **86**, 1335 (2001).
[152] J. Ma, Y. Kamiya, T. Hong, H. B. Cao, G. Ehlers, W. Tian, C. D. Batista, Z. L. Dun, H. D. Zhou, and M. Matsuda, Phys. Rev. Lett. **116**, 087201 (2016).
[153] S. Ito, N. Kurita, H. Tanaka, S. Ohira-Kawamura, K. Nakajima, S. Itoh, K. Kuwahara, and K. Kakurai, Nat. Commun. **8**, 235 (2017).
[154] A. L. Chernyshev and M. E. Zhitomirsky, Phys. Rev. Lett. **97**, 207202 (2006).
[155] A. L. Chernyshev and M. E. Zhitomirsky, Phys. Rev. B **79**, 144416 (2009).
[156] M. Mourigal, W. T. Fuhrman, A. L. Chernyshev, and M. E. Zhitomirsky, Phys. Rev. B **88**, 094407 (2013).
[157] M. E. Zhitomirsky and A. L. Chernyshev, Rev. Mod. Phys. **85**, 219 (2013).
[158] E. A. Ghioldi, A. Mezio, L. O. Manuel, R. R. P. Singh, J. Oitmaa, and A. E. Trumper, Phys. Rev. B **91**, 134423 (2015).
[159] A. S. Wills, R. Ballou, and C. Lacroix, Phys. Rev. B **66**, 144407 (2002).
[160] J. M. Luttinger and L. Tisza, Phys. Rev. **70**, 954 (1946).
[161] B. Fåk, S. Raymond, D. Braithwaite, G. Lapertot, and J.-M. Mignot, Phys. Rev. B **78**, 184518 (2008).
[162] A. Krimmel, H. Mutka, M. M. Koza, V. Tsurkan, and A. Loidl, Phys. Rev. B **79**, 134406 (2009).
[163] B. Fåk and B. Dorner, Physica B: Condensed Matter **234**, 1107 (1997).
[164] S. Petit, JDN **12**, 105 (2011).
[165] S. Toth and B. Lake, Journal of Physics: Condensed Matter **27**, 166002 (2015).
[166] T. Yavors'kii, M. Enjalran, and M. J. P. Gingras, Phys. Rev. Lett. **97**, 267203 (2006).
[167] N. d'Ambrumenil, O. A. Petrenko, H. Mutka, and P. P. Deen, Phys. Rev. Lett. **114**, 227203 (2015).
[168] W. Schweika, S. V. Maleyev, T. Brückel, V. P. Plakhty, and L.-P. Regnault, EPL (Europhysics Letters) **60**, 446 (2002).